Designing a Telescope for Laser Communication with Ceramic Matrix Composites

Evaluating the viability of C/C-SiC for thermally stable space optics

Thesis report

Gilles Hartman, 5624801

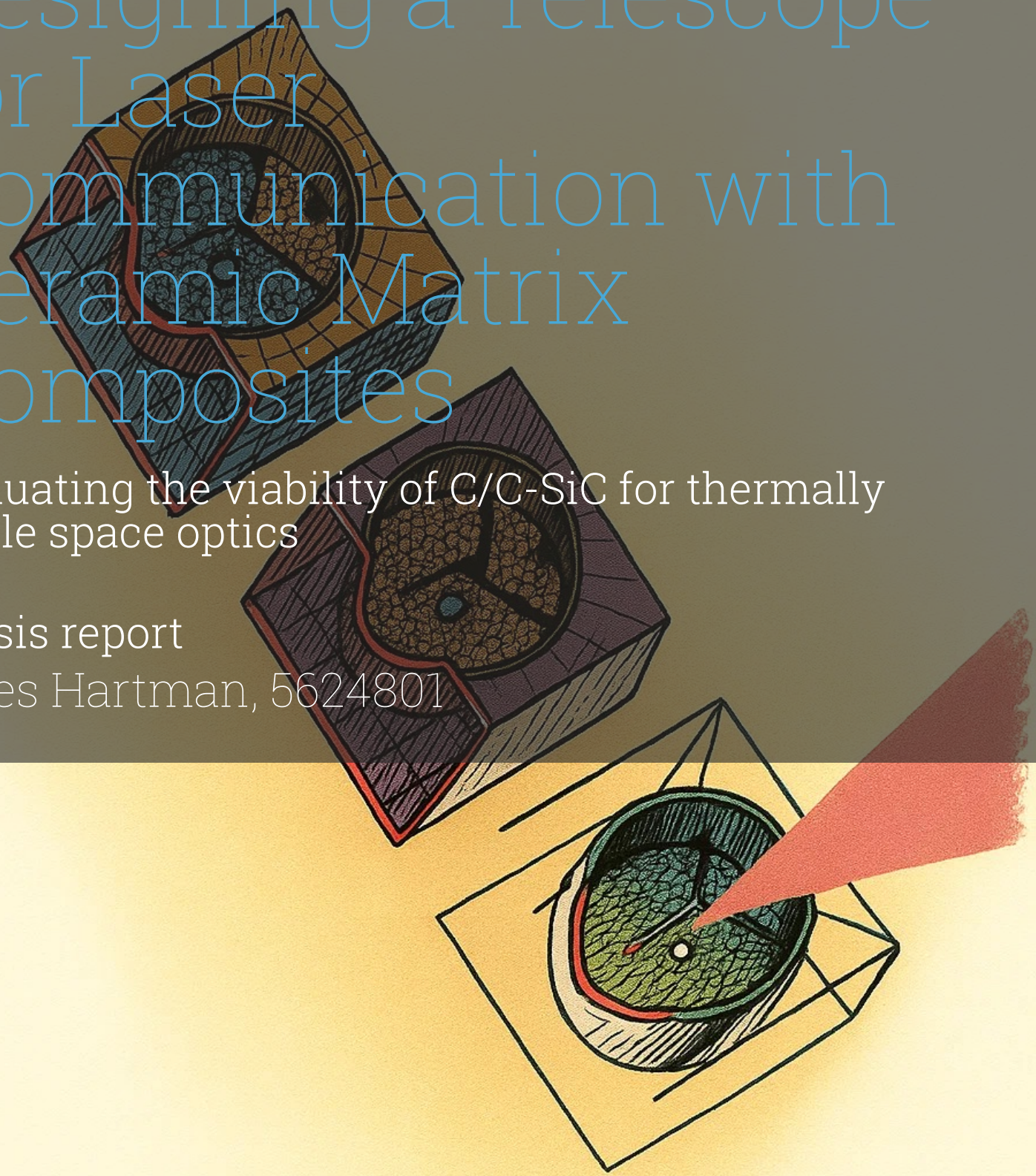

Delft University of Technology

TU Delft

TNO

Designing a Telescope for Laser Communication with Ceramic Matrix Composites

Evaluating the viability of C/C-SiC for thermally stable space optics

by

Gilles Hartman, 5624801

to obtain the degree of Master of Science

at the Delft University of Technology,

to be defended publicly on Monday, September 29, 2025, at 9:30 AM.

Student number:	5620481	
Project duration:	January 13, 2025 – September 29, 2025	
Committee Chair:	Dr. Y. Tang,	TU Delft, Chair
	Dr. Ir. D.M.J. Peeters,	TU Delft, Supervisor
	Dr. Ir. R. Saathof,	TU Delft, External Member
	Dr. Ir. J. de Vreugd,	TNO, Company Supervisor

Cover:	Graphical interpretation of the thermo-mechanical model results
Style:	TU Delft Report Style, with modifications by Gilles Hartman

An electronic version of this thesis is available at `http://repository.tudelft.nl/`.

TU Delft

Abstract

Carbon–carbon silicon carbide (C/C–SiC) is a ceramic matrix composite combining low density with high stiffness, damage tolerance, and excellent thermal properties. A feature of this material is its low (0.1μm/mK) and tunable coefficient of thermal expansion (CTE), making it highly suitable for precision structures that must remain dimensionally stable under varying thermal loads. This thesis investigates its applicability to a $\varnothing$100m̃m Cassegrain telescope structure as a candidate for space-based laser communication terminals. A parametric thermo-elastic finite element model was developed in COMSOL Multiphysics. Rigid body motions and surface form errors were quantified using a Zernike-polynomial-based Python post-processing pipeline, enabling evaluation of optical performance. Results show that by targeting a near-zero in-plane CTE, C/C–SiC can maintain deformations within acceptable limits, supporting its feasibility for lightweight and stable free-space optical communication systems. Using an opto-thermo-mechanical workflow, the model couples radiative and conductive heat transfer with the structural response to assess wavefront stability under representative orbital thermal load cases. Within the evaluated steady-state cases, tuning the in-plane CTE to approximately 0.1–0.5 μm/mK kept rigid-body motions and surface-form errors within a $\lambda/30 \approx 50$ nm RMS budget, leaving margin for other effects treated as out of scope. From a production perspective, however, current cleanliness and manufacturing-consistency challenges for large continuous-fibre C/C–SiC constrain near-term applicability to off-the-shelf terminals, suggesting more viable deployment in other use cases until maturity improves.

Preface

This work documents my graduation project at TNO-Optomechatronics, where I initially set out to produce a validated thermo-mechanical model through a planned thermal-vacuum chamber test. However, unforeseen hurdles arose, and the testing campaign was postponed. Although I would still welcome the opportunity to participate in such a campaign, the setback had its silver lining. The shifting objectives and uncertainty posed a project-management challenge through which I learned a great deal and successfully pivoted to a model-based project without significant delay. This pivot sharpened my ability to manage scope, communicate across disciplines, and maintain momentum under uncertainty. The experience proved especially valuable, not least because of the behind-the-scenes view of the CASTT project. I will look back fondly on my time at TNO and the lessons learned during this project.

Acknowledgements

I extend my most sincere thanks to TNO-Optomechatronics and all my colleagues for their guidance and camaraderie. In particular, I am deeply grateful to Jan de Vreugd for our weekly discussions; his enthusiasm and expertise consistently sharpened my thinking, and to Daniël Peeters for keeping the work on track across the many disciplines this project touched. I am especially thankful to Arceon, FSO Instruments, and the European Space Agency (ESA) for their collaboration and openness; in particular, Yesting van Haaren, Rahul Sharma, and Dorus de Lange, who generously shared their time and insights. From the faculty, I thank Yinglu Tang for candid discussions and Ines Uriol Balbin for helping me get the project started. I am also grateful to Rudolf Saathof and the research group for valuable perspective on laser communications during the monthly meetings.

Above all, I owe heartfelt thanks to my family, friends, and my girlfriend for their unwavering support, patience, and encouragement. Their belief made this work possible and sustained me throughout the inevitable challenges. I would never have made it this far without any of them.

Gilles Hartman, 5624801
Delft, September 2025

Contents

Nomenclature

Abbreviations

Abbreviation	Definition
ARCEON	Company name; manufacturer of C/C-SiC components
ARIEL	Atmospheric Remote-sensing Infrared Exoplanet Large-survey (ESA mission)
ATOX	Atomic oxygen (space environment)
AU	Astronomical Unit
BAM	Basic Angle Monitoring (system)
BS	Beam Splitter
C/C	Carbon–Carbon (preform)
C/C-SiC	Carbon–Carbon Silicon Carbide (a type of Ceramic Matrix Composite)
CAD	Computer-Aided Design
CASTT	Carbon and Silicon-Carbide Telescope Tube (project)
CCD	Charge-Coupled Device
CFRP	Carbon Fiber Reinforced Polymer
CHEOPS	CHaracterising ExOPlanets Satellite (ESA mission)
CHIME	Canadian Hydrogen Intensity Mapping Experiment (mission)
CMC	Ceramic Matrix Composite
CME	Coefficient of Moisture Expansion
COMSOL	COMSOL Multiphysics (FEM software)
CT	Computed Tomography (imaging)
CTE	Coefficient of Thermal Expansion
CVI	Chemical Vapor Infiltration
DLR	German Aerospace Centre (Deutsches Zentrum für Luft- und Raumfahrt)
EC2216	Two-part aerospace epoxy adhesive (3M)
ECSS	European Cooperation for Space Standardization
EO	Earth Observation
ESA	European Space Agency
FEA	Finite Element Analysis
FEM	Finite Element Method
FSO	Free-Space Optical (Instruments, company name)
FSOC	Free-Space Optical Communication
G-CVI	Gradient Chemical Vapor Infiltration
GEO	Geostationary Orbit
I-CVI	Isothermal-Isobaric Chemical Vapor Infiltration
IR	Infrared
JWST	James Webb Space Telescope
LC	Load Case
LC1, LC2, LC3, LC4, LC5	Load Cases 1–5
LCT	Laser Communication Terminal
LDPC	Low-Density Parity-Check (coding)
LEO	Low Earth Orbit

Abbreviation	Definition
LSI	Liquid Silicon Infiltration
LWR	Longwave Radiation (thermal IR)
MAC	Mass Acceleration Curve
M1	Primary Mirror (in telescope systems)
M2	Secondary Mirror (in telescope systems)
MEO	Medium Earth Orbit
MIRI	Mid-InfraRed Instrument (JWST instrument)
MLI	Multi-Layer Insulation
MPa	Megapascal
MTS	Methyltrichlorosilane (CVI precursor)
NBF	Narrow Band Filter
PEEK	Polyether ether ketone
PV	Peak-to-Valley (surface deviation metric)
PAT	Pointing, Acquisition, and Tracking
PBS	Polarization Beam Splitter
PyC	Pyrolytic Carbon
QWP	Quarter Wave Plate
RBM / RBMs	Rigid Body Motion(s)
RF	Radio Frequency
RMS	Root Mean Square
RS-80	Model name of a Laser Communication Terminal (by FSO Instruments)
SD / SDs	Surface Deformation(s)
SiC	Silicon Carbide
STOP	Structural, Thermal, and Optical Performance analysis
SWaP	Size, Weight, and Power
TNO	Netherlands Organisation for Applied Scientific Research
TVC	Thermal Vacuum Chamber
UV	Ultraviolet
WFE	Wavefront Error
W/mK	Watts per meter-Kelvin
ZEMAX	OpticStudio (optical design software)

Symbols

Symbol	Definition	Unit
A	Cross-sectional area for conduction	[m^2]
A	Aperture area (link budget antenna gain context)	[m^2]
c_p	Specific heat capacity	[J/(kg·K)]
c_i	Zernike polynomial coefficient	[-]
D_R, D_T	Receiver and transmitter aperture diameters	[m]
D_x, D_y	Decentering in x and y	[μm]
D_z	Piston (axial displacement)	[μm]
d_{M1_M2}	Distance between M1 and M2 surfaces	[m]
E	Radiant exitance (Stefan–Boltzmann law)	[W/m^2]
E	Young's modulus	[GPa]
f_1	First eigenfrequency	[Hz]
G	Shear modulus	[GPa]
G_R, G_T	Receiver and transmitter antenna gains	[-]
g	Standard gravity acceleration	[m/s^2]

Symbol	Definition	Unit
h_c	Cylinder height	[m]
h_f	Flexure height	[m]
h_t	Terminal height	[m]
k	Thermal conductivity	[W/(m·K)]
$k_\parallel, k_\perp$	In-plane and through-thickness conductivity	[W/(m·K)]
L	Distance between conduction nodes	[m]
L_{new}	Scaled M1–M2 separation	[m]
L_{ref}	Reference M1–M2 separation	[m]
L_s	Space loss factor	[-]
l_s	Spider arm length	[m]
m	Azimuthal Zernike index	[-]
n	Radial Zernike index	[-]
N	Number of Zernike modes used in fit	[-]
P_R, P_T	Received and transmitted optical power	[W]
q	Heat flux density	[W/m^2]
Q_{ij}	Heat flow between nodes i and j	[W]
r	Normalized radial coordinate	[-]
r_c	Cylinder radius	[m]
r_{m1}	M1 radius	[m]
r_{m2}	M2 radius	[m]
$R_{mn}(r)$	Zernike radial polynomial	[-]
R_{max}	Aperture radius for Zernike normalization	[m]
R_x, R_y	Tip/Tilt rotations about x and y axes	[rad]
t_c	Cylinder thickness	[m]
t_f	Flexure thickness	[m]
t_{m1}	M1 thickness	[m]
t_s	Spider thickness	[m]
t_t	Terminal wall thickness	[m]
T	Absolute temperature	[K]
u	Displacement in x direction	[m]
v	Displacement in y direction	[m]
w	Displacement in z direction / sag	[m]
w_{clean}	Sag after RBM removal	[m]
w_f	Flexure width	[m]
w_s	Spider width	[m]
w_t	Terminal width	[m]
x, y, z	Cartesian coordinates	[m]
Z_i	ith Zernike mode (OSA/ANSI)	[-]
WFE	Wavefront error	[nm RMS]
α	Absorptivity	[-]
α_T	Truncation ratio (Tx aperture)	[-]
Δ	Difference operator	[-]
ϵ	Emissivity	[-]
η_R, η_T	Receiver/transmitter optical efficiency	[-]
η_{TP}	Pointing loss factor	[-]
η_λ	Narrow band filter transmission	[-]
η_ℓ	Additional optical losses (path loss)	[-]
γ_R, γ_T	Obscuration ratios (Rx/Tx)	[-]
λ	Wavelength	[m]
ν	Poisson's ratio	[-]
ρ	Density	[kg/m^3]
σ	Stefan–Boltzmann constant	[W·m^{-2}·K^{-4}]
σ_y	Yield stress	[MPa]

Symbol	Definition	Unit
θ	Angular coordinate	[rad]

List of Figures

List of Tables

1

Introduction

1.1. Ceramics in precision optical systems

Ceramics are among the oldest synthesized materials in human history and are perhaps most (in)famously known for their brittleness or tendency to fracture. Nevertheless, some specific ceramics, have found their way into high-performance aerospace applications. Due to a variety of unique properties, one example is silicon carbide (SiC), used for structures in telescopes, such as the Euclid telescope and other optical instruments, e.g., the Gaia basic angle monitoring system (BAM). SiC is chosen because of its low coefficient of thermal expansion (CTE), high thermal conductivity, stiffness, and low weight. Both the SiC parts for Euclid and Gaia are and were produced by a French company, Boostec, now part of the Mersen group. Figure 1.1 shows the BAM optical bench and the details of the SiC assembly [34, 35].

Figure 1.1: The SiC BAM optical bench at TNO, whose intricate design and SiC material enable thermally stable precision. A key part of the Gaia system. Image courtesy of Fred Kamphues [1].

The Gaia BAM system was in part designed and assembled at the Dutch organization for applied scientific research TNO. Gaia BAM uses pico meter ($10^{-12}m$) accuracy measurements in optical path difference to monitor the relative deformation of the 2 Gaia primary mirrors. These extreme requirements

could at the time only be met through SiC-based optics, due to its unique properties. But SiC also has drawbacks, for example, its brittleness, which during handling and assembly makes it vulnerable to chipping or breaking. In addition, it is extremely hard, making it time-consuming and expensive to machine, which, due to that same brittleness, is a risk. A few examples of the brittleness causing a fracture are shown in Figure 1.2 below:

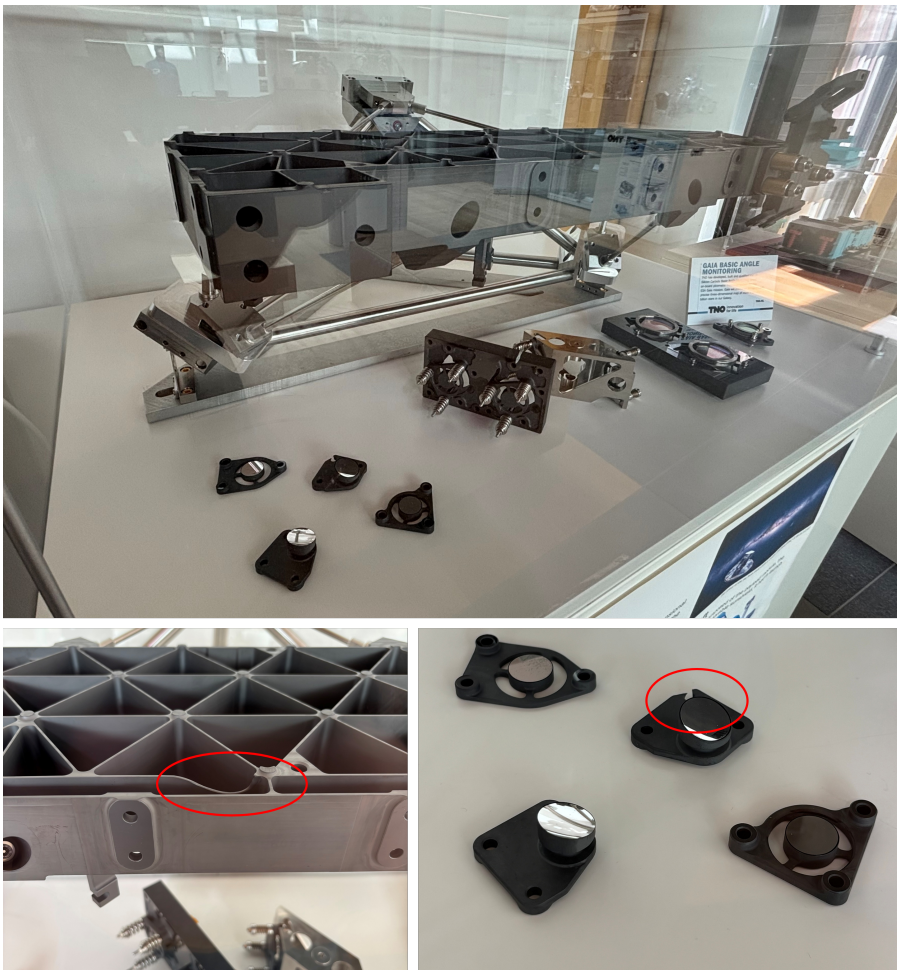

Figure 1.2: A show model of the BAM optical bench at TNO, at the bottom: encircled on the left, a chip in the bench structure*, on the right, a broken mirror support connection.

* The chip in this example is polished/machined to minimize stress concentrations. In which case it is possible to qualify the part for flight.

But what if we could retain or even improve these properties while reducing brittleness? One strategy to achieve this is through a material developed over the last few decades, it involves reinforcing the ceramic with fibers. For example, carbon fibers are well known for their strength, stiffness, and low weight. When SiC and carbon fibers are combined with a weak interface between them, a fracture, which would cause a failure in a ceramic part like the examples in Figure 1.2, can be halted at the fiber–matrix boundary. Here the crack is deflected along that weak interface instead of propagating through the bulk material, as schematically shown in 1.3.

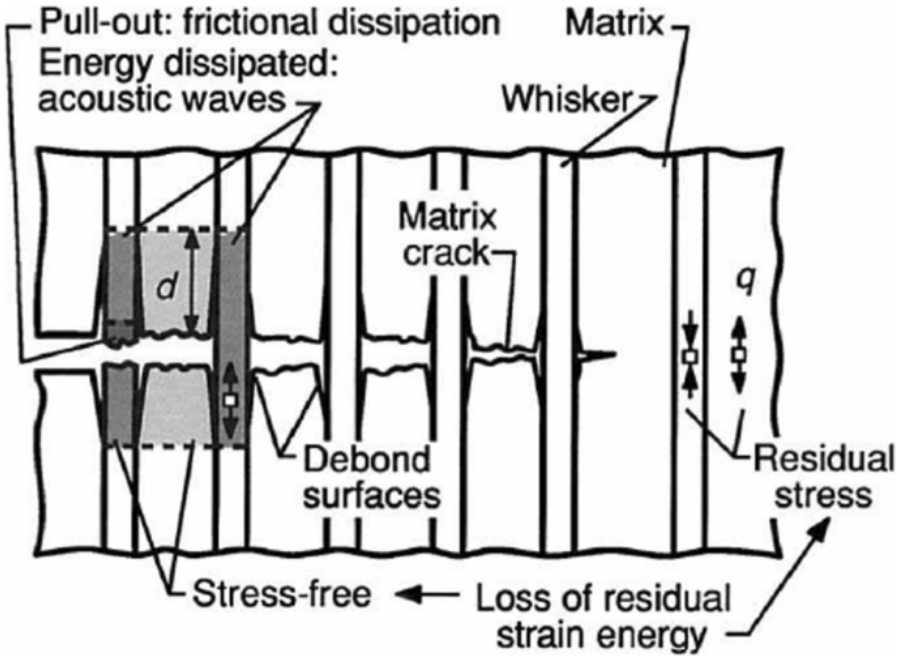

Figure 1.3: Schematic crack arrest by different dissipating mechanisms through the introduction of a fiber as reported by [2]

This type of material, a ceramic matrix composite (CMC), has been in development since the end of the 1980s at the German Aerospace Center (DLR). An example of the first parts in which they were used is lightweight structures for thermal protection systems of reentry vehicles. Exploiting their oxidation resistance and low weight. Carbon carbon silicon carbide (C/C-SiC) is one example of many different types of CMCs.

Compared to SiC, C/C-SiC is even more dimensionally stable w.r.t. temperature changes, commonly quantified by the coefficient of thermal expansion. This material property is generally a constant (over a specific temperature range) for example, aluminum has a CTE of 23 $[\mu m/mK]$. This can be reduced to 10 $[\mu m/mK]$, by adding significant amounts of Silicon and using special production techniques. Titanium has a CTE of roughly 9 $[\mu m/mK]$, where SiC's CTE is 4 $[\mu m/mK]$ nominally but reported to be as low as 2.2 by Boostec. [21, 22, 35]

A. Schöppach et. al. (2001) have found that C/C-SiC can be tuned to have a $0 \pm 0.1[\mu m/mK]$ value for samples of flat plates. This was achieved by varying the percentage of its constituents, C/C and SiC. In a follow up study, B. Heidenreich et. al. reported a number of sample tubes, 2 of 78 and 3 of 150 $\varnothing mm$ the axial CTE values were measured to be between -0.1 and 0.21 $[\mu m/mK]$ by an interferometric measurement. The aim of the follow up study was in part to investigate the effect of manufacturing choices on the CTE values. Their conclusion was that by varying fiber type, volume content, and orientation, and most importantly the SiC volume percentage, the CTE of C/C-SiC could be influenced in a range from -0.5 to 0 $[\mu m/mK]$. [19, 20]

After some development liquid silicon infiltration has emerged as the method to most cost-effectively make C/C-SiC parts. [12] Arceon is a company based in Delft using and developing this manufacturing technique for both continous and short fiber parts.

1.2. C/C-SiC for large telescopes

C/C-SiC's low CTE, high specific stiffness, and fracture toughness make it a highly interesting candidate for sensitive optical equipment. Moreover, a domestic manufacturer of low-CTE materials is still absent in the Netherlands. Consequently, both ESA and TNO Opto-mechatronics are interested in further developing Arceon's material. They have joined forces in the Carbon and Silicon-Carbide Telescope Tube (CASTT) project to de-risk Arceon's production techniques and to design and manufacture a $\varnothing$200 mm C/C-SiC tube-based telescope structure. Which currently is the largest continuous fiber

C/C-SiC component of this type known to have been produced.

Although the CASTT project improves manufacturing consistency at a scale not previously achieved—while also demonstrating the in-situ joining technique for creating larger monolithic parts, questions remain about the achievable performance improvements in practical applications. From the user side (TNO & ESA), it is uncertain whether the development effort is justified; from the developer side (Arceon), it remains unclear exactly which material properties should be targeted for a given use case. From the developer point of view tuning the material properties is possible but takes effort and is achieved by parameters like fiber type, layup and silicon carbide percentage, for a specific part it takes time, resources, and experience. These costs could be mitigated by analysis if it is possible to provide a range of inputs for which the material properties and design are likely to be valid.

This thesis answers these questions in the context of a case study. Choosing one, is done by considering the following principles, first the information available, second, the need in industry and the limits of feasibility given the current state of development. This still leaves a multitude of possibilities for a use case to consider. But given the relative cost-effectiveness of the material, ongoing developments at TNO, previous research, and current trends within the Dutch space market, the telescope of a satellite-based laser communication terminal (LCT) has been identified as a most suitable candidate.

Partially motivating this choice is prior research at TNO, which has shown that LCT telescope designs could significantly benefit from low-CTE structural materials. A structure appropriate for such an optical design is currently being developed and produced within the present project(s) at TNO. Furthermore, an LCT is presently under development at TNO in collaboration with FSO Instruments, providing relevant background information to inform the requirements and design of the model. Additional background of such systems is discussed in the following section.

1.3. Free-space optical communication from a satellite

The reasons for the development of laser communication terminals (LCTs), their network architecture, and application details are covered in Chapter 3. In short, the rapid growth in global data demand is placing increasing strain on traditional radio-frequency (RF) communication systems, prompting the exploration of alternative technologies. One such candidate is laser-based communication, known in academia as free-space optical communication (FSOC). It uses laser transmission in the near-infrared/visible spectrum to enable high-bandwidth, secure, low-latency links. Figure 1.4 shows a schematic of an FSOC (laser satellite communication, LSatCom) network as envisioned and being developed by TNO and, in part, FSO.

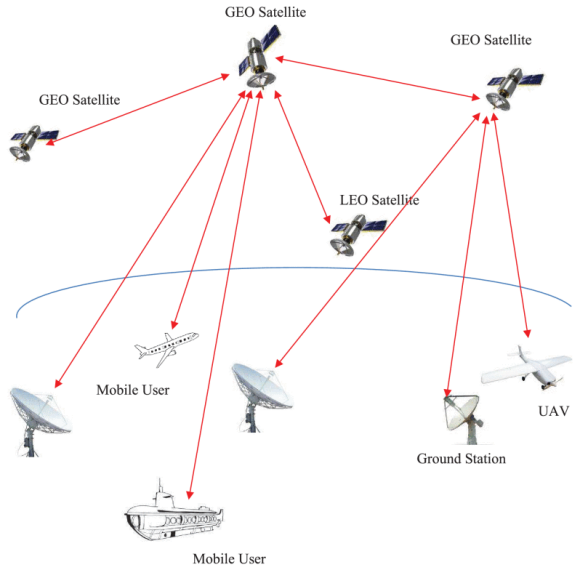

Figure 1.4: Example of the application environment, from [3].

Free-Space Optical Instruments (FSO) is a Delft-based company aiming to commercialize laser communication terminals. The company plans to offer a range of terminal sizes as off-the-shelf products, developed in cooperation with several partners, including TNO. In satellite applications, every kilogram is critical; therefore, the increasing demand for data transfer poses a significant challenge, as the required communication system typically scales with the volume of data. A system that reduces both size and mass, while also being substantially more secure against interception, represents a highly attractive proposition [36].

However, selling an off-the-shelf product poses a challenge because the LCT must operate across a much broader range of environments than conventional optical systems. LCT performance is sensitive to thermal and mechanical disturbances, especially in the harsh and variable conditions of space. For example, in Low Earth Orbit (LEO) a satellite takes roughly 1.5 hours to complete an orbit around Earth and may move in and out of Earth's shadow up to 16 times per day. Thermally induced deformations can severely impact optical alignment and link quality.

Quantifying these effects is complicated; however, wavefront error (WFE) is a commonly used metric to assess the performance of an optical system. It summarizes the deviation of the incoming wavefront with respect to (w.r.t.) the expected (unaberrated) wavefront. Thermal and mechanical disturbances shift and deform the beam in distinctive, measurable ways. This wavefront deviation summarizes the performance of an LCT telescope well for the purposes of this thesis project [3].

1.4. Research description

This thesis investigates the potential of C/C-SiC as a structural material for telescope assemblies through a specific telescope designed for an LCT. The design is modelled numerically with C/C-SiC as the main structural material. Using this model, the academically shown tunable material properties are varied to find a feasible set for which the structure performs in the LCT use case.

The case study is used to investigate this material's performance under a representative thermal loading scenario by means of finite element analysis. The aim is to quantify the effect of temperature changes on deformation and to evaluate whether C/C-SiC's near-zero coefficient of thermal expansion and high specific stiffness offer advantages in a realistic FSOC context. Hence, the research question this thesis answers is the following:

Research Question

Can a ⌀100 mm telescope structure made from C/C-SiC be used to maintain wavefront error within acceptable limits under representative LEO thermal load cases for laser communication applications?

The effect of the environments and phenomena to which an LCT is subjected in space based platforms as well as common strategies to model these effects are reported by [8]. This framework is used and extended to model the telescope structure. It serves both as the analytical backbone for the case study and as a transferable process for follow-up studies.

A semi-modular approach is achieved by parametric setup of the FEA model. Which allows for the integration of material-specific behavior—such as the orthotropy and thermal property uncertainty associated with C/C-SiC and the phase in which the developments are currently at. The approach also provides a means to assess performance across a range of mission-relevant conditions and design parameters. Together, the case study and extended methodology form an example for evaluating the use of advanced composite materials in thermally sensitive optical space systems.

1.5. Report structure

The initial chapters establish the context and information for the method used to answer the research question. Chapter 2 reviews prior work at TNO, Arceon, and FSO alongside the relevant literature. Chapter 3 discusses the laser communication telescope (LCT) use case in detail, providing the contextual basis for constructing the FEA models used to evaluate telescope performance. Chapter 4 examines the manufacturing techniques associated with C/C–SiC and outlines alternative materials relevant to the LCT application and used in the model. Together, these chapters serve in part to address the following guiding questions:

- What prior research and work at TNO, Arceon, FSO, and in the relevant research communities informs this thesis, and how is it applied to the project?
- What is the objective of the LCT telescope, how can its performance be quantified for thermo-mechanical assessment, and how is the operational environment defined, incorporated, and reported within the analysis?
- How does melt-infiltration manufacturing of C/C–SiC work, and what are its implications for defining a preliminary LCT telescope geometry and the material property range to be considered?

The second part of the report focuses on the implementation of a thermo-mechanical modeling methodology to evaluate the performance of a C/C–SiC-based telescope structure. The modeling workflow covers radiative and conductive heat transfer and the resulting structural deformation in Chapter 5. The model is constructed parametrically, enabling the investigation of performance with varying geometric as well as material input parameters. The results are reported in Chapter 6. Together, these chapters serve in part to address the following guiding questions:

- How is the LCT telescope modeled in COMSOL Multiphysics, and how is this modeling linked to the requirements?
- How do CTE and thermal conductivity variations affect thermoelastic deformation in the preliminary model, and which model/design updates are needed to better meet the objective and improve predicted performance?

In the final chapters of the report, the results and supporting information are used to substantiate the concluding statement in Chapter 7, after which recommendations and directions for future work are presented in Chapter 8.

2

Background & Prior work

To assess the research questions of this thesis, it is essential to first establish a clear background on both the material under study (C/C-SiC) and the use case's application field (laser satellite communication). These two domains are technically complex and not widely familiar outside their specialist communities. Both remain active areas of research and engineering practice. Hence, additional clarification is required to explain their role in the current project. Accordingly, the following chapter provides a structured overview of the background to position this study.

First, the chapter highlights internal (i.e., TNO and Arceon) and external activities in the field of C/C-SiC, focusing on material development and related activities that directly inform the present research. This includes an introduction to the processes, applications, and properties of C/C-SiC compared to other relevant materials.

Second, the chapter turns to FSOC, reviewing both internal developments and background information from the broader research landscape. The overview addresses the context of free-space optical communication, its operational requirements, and the status of satellite communication links.

Finally, once these topics are introduced, the concepts of CTE matching and rigid body deformations are covered. Both are multidisciplinary in nature and strongly influence the design of an LCT and its telescope. These concepts depend on an understanding of the system, its objectives, and the materials involved.

The structure of the chapter is therefore organized around the following five points:

- Internal activities in C/C-SiC material development.
- External background on C/C-SiC and its applications in optics.
- Internal activities in laser satellite communication and LCT development.
- External background on laser communication and its system-level context.
- CTE matching and rigid body motions.

Using the search to answer of the following guiding question as the overarching goal :

What prior research and work at TNO, Arceon, FSO, and in the relevant research communities informs this thesis, and how is it applied to the project?

2.1. C/C-SiC at TNO and Arceon

At the time of writing, TNO is working on the Carbon And Silicon-Carbide Telescope Tube (CASTT) project, which aims to develop and test a C/C-SiC tube structure. This project forms the basis of the present thesis, and the following section summarizes its implications and experiences, which have influenced and informed both the approach and results of this work.

As mentioned, the near-zero CTE and damage tolerance of C/C-SiC make it a promising solution for highly stable structural components. In addition, its high specific stiffness and strength properties are particularly valuable in space environments, where low Size, Weight, and Power (SWaP) requirements are critical for space systems and LCTs [36]. From this premise, ESA, TNO, and Arceon have joined forces in the CASTT project, which aims to manufacture and test a 200 mm telescope support structure made from C/C-SiC.

A CAD rendering of the proposed thermal vacuum chamber (TVC) test assembly is shown in Figure 2.1. It provides an example of the production possibilities of C/C-SiC and how the material can be integrated into an optical assembly similar to a telescope. The hypothesis driving the CASTT project is that C/C-SiC can be effectively utilized to manufacture optical support structures that maintain very precise alignment under the thermal conditions encountered in orbit. Hence, the campaign envisioned to test this by thermal vacuum chamber (TVC) was designed.

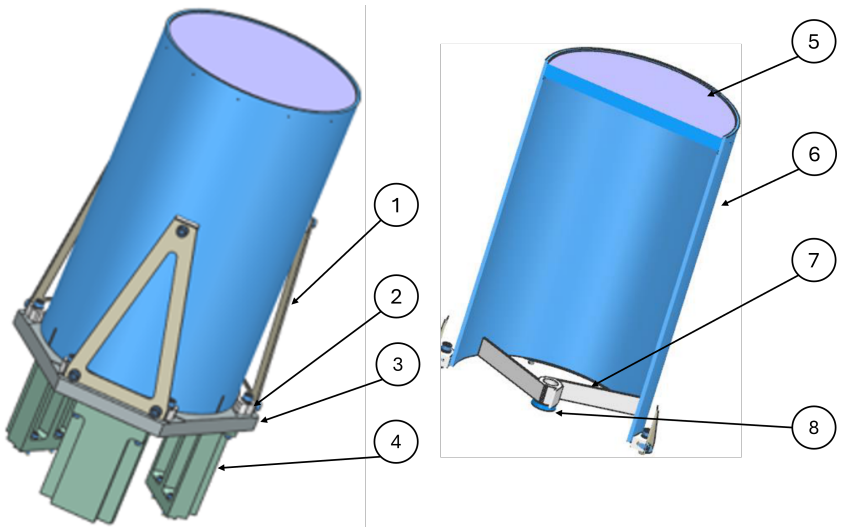

Figure 2.1: Shows the test object design, (1) leaf spring (2) leaf spring connection block (3) support plate (4) distance blocks (5) M1 mirror (6) C/C-SiC Tube (7) C/C-SiC spider (8) [4]

In parallel, TNO and ARCEON are both interested in other use cases and applying the lessons learned to other applications. From this context the thesis research project, as it is presented in this report, was conceived.

2.2. Synthesizing and manufacturing, C/C-SiC, C/SiC

Before the challenges encountered in the CASTT project are covered in more detail, an introductory explanation is provided about the composition and history of the material.

C/C-SiC is made up of two parts or constituents: the C/C and the SiC. Both have distinct origins and unique properties that contribute to the overall performance of the composite. To better understand their combined behavior, it is essential to first examine the individual characteristics of carbon carbon and silicon carbide.

Carbon-fiber-reinforced carbon (C/C) materials were developed in response to the need for materials that can withstand very high temperatures while remaining lightweight. The first applications for which they were intended are in the space and military fields. For example, rocket nozzles or engine flaps.

Carbon/carbon materials were originally developed in the late 1960s to meet the demand for high-temperature, lightweight materials in military and aerospace applications, such as rocket nozzles and missile re-entry components. Their excellent thermal stability, remaining stable above 3000°C, and low density made them ideal for these extreme conditions. C/C is typically manufactured by reinforcing carbon fibers with a carbon matrix, produced through the carbonization of polymer precursors.

However, despite their high temperature resistance, C/C materials have limited oxidation stability above 400°C, which restricts their use in oxidative environments. To overcome this limitation, silicon (Si) infiltration is applied, enhancing the composite's oxidation resistance by reacting with the carbon to form SiC. Thus extending its service life in air at elevated temperatures. [37]

Silicon carbide is a ceramic material known for its hardness, thermal conductivity, and excellent oxidation resistance at elevated temperatures. Unlike C/C, SiC maintains its structural integrity and performance in oxidative environments. SiC is typically produced through chemical vapor deposition, sintering, or infiltration processes, resulting in a dense, stable phase that enhances the composite's durability and thermal stability. When combined with C/C, SiC improves the overall oxidation resistance and mechanical strength of the resulting composite, enabling its use in more demanding high-temperature applications.

The two constituents are combined in a three-step process. First, a carbon-fiber-reinforced part is produced using a specific resin. The resin is then removed through pyrolysis, a controlled heating process that causes its evaporation and leaves behind a porous structure. Finally, these pores are infiltrated with silicon, which at high temperatures (> 1420°C) reacts with the carbon to form silicon carbide (SiC). The infiltration is achieved through different methods, yielding different quality and types of products.

2.2.1. Applications C/C-SiC

The complexity of the process comes at a cost, which in its original applications, e.g., thermal protection systems, is acceptable due to the unique combination of properties. However, with the development of liquid infiltration processes, the reduced cost generated interest in other applications as well [38]. Several early application examples and their cost distributions were reported in [39]. Arceon's materials are based on the liquid silicon infiltration (LSI) method. They illustrate the types of products that are currently manufactured successfully.

The low CTE and high specific properties have not gone unnoticed. One example is a telescope tube for the LCT on the NFIRE and TerraSAR-X satellites. As is shown in figure 2.2. The LCT referenced here used a roughly 130 mm aperture C/C-SiC telescope in its periscope design.

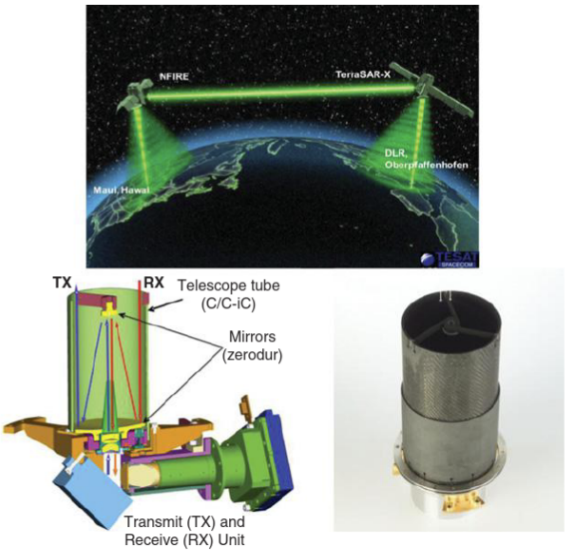

Figure 2.2: From the top in a clockwise direction, an artist's interpretation of the NFIRE and TerraSAR-X communication link, the final telescope structure design based on two tubes, and a CAD model with a section of the telescope. From figure 6.62 in [5]

In addition to oxidation resistance, maintained structural properties at high temperatures enable the material for use in rocket or re-entry vehicle nose cones, jet vanes, or gas turbine engines. Other applications include ballistic protection, high-temperature furnace devices, and brake systems. [20].

Over the years, a multitude of applications have been considered and executed. Some notable high temperature examples are reported in [5]. They include at least 3 re-entry vehicle nose caps shown the X38 is shown in figure 2.3.

Figure 2.3: C/SiC and C/C-SiC structures for the X38 spacecraft (NASA). Bottom left, a C/SiC (G-CVI) body flap assembly (two flaps, each 1600 mm × 1400 mm × 150 mm, t = 5–15 mm, m = 68 kg, MT) based on substructures joined with C/SiC (CVI) screws. Bottom right, a C/C-SiC (LSI) nose cap (about 740 mm × 640 mm × 170 mm, t = 6 mm, m = 7 kg, DLR). From figure 6.62 in [5].

C/C-SiC is most widely adopted in high-temperature friction systems. It is known for its high-performance tribological properties, hence their found in high-performance cars, airplane propeller engines, high-speed maglev trains, and elevator brakes. An example from the same section of the aforementioned chapter is found in figure 2.4.

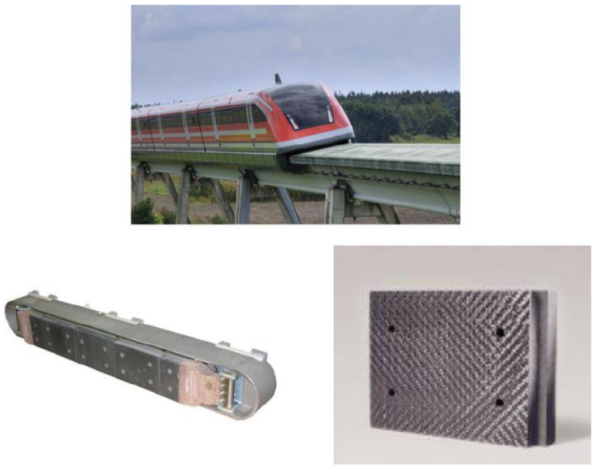

Figure 2.4: From the top, the emergency runner system for the Transrapid in Shanghai (ThyssenKrupp Transrapid GmbH © Fritz Stoiber Productions GmbH). Bottom left, a sliding unit (SKT) equipped with five C/C-SiC (PCI) pads (600 mm × 110 mm × 22 mm in total). Bottom right, a single C/C-SiC pad (159 mm × 110 mm × 28 mm, SKT). From figure 6.64 in [5].

2.2.2. C/C-SiC compared to Common Materials Used in Space

C/C-SiC properties are relatively dependent on manufacturing parameters such as fiber direction, or fiber volume fraction. For example, in case of the latter, increasing fiber volume fraction in a composite along a given direction typically results in increased stiffness and thermal conductivity, while reducing the CTE in that direction. However, not all combinations of material properties are physically feasible due to these intrinsic correlations.

Common metallic materials used in spacecraft include aluminum and titanium alloys, valued for their strength-to-weight ratio, machinability, and established heritage in space systems. While these

materials generally offer isotropic properties and reliable long-term behavior, their relatively high CTE values render them suboptimal for precision optical applications in cases where thermally induced deformations must be minimized and thermal gradients cannot be avoided. However, their proven track record and CTE matching strategy make them the material of choice for a lot of applications. [40]

Ceramic materials such as fused silica, Zerodur, and SiC are frequently employed in optical systems due to their low thermal expansion, dimensional stability, and polishability. However, these materials are often brittle and require careful mechanical integration. A summary of their properties compared to structural materials is shown in Table 2.1

Table 2.1: Reports the typical thermo-mechanical properties of the relevant materials. Note both C/C-SiC and M55J/EX-1515 are orthotropic materials, i.e., their properties are orientation dependent. * Twill woven quasi-isotropic layup. **Yield strength is not as relevant for composite materials. Hence, interlaminar shear strength is provided. *** Normalized to 60% fiber volume. Lay-up Configuration:0°, 45°, 90°, 135° symmetrical. [5, 21–24]

Property description	Secant CTE	Young's modulus	Yield strength	Density	Conductivity	Specific heat capacity
Property [unit]	CTE [μm/mK]	E [GPa]	σ_y [MPa]	ρ [kg/m^3]	k [W/mK]	c_p [J/kgK]
RSA6065-T6 Alu	22.6	70	315	2700	169	900
Timet-550 Plate	8.8	110	900	4500	21.9	522
C/C-SiC in-plane*	1.1 to -1	70*	σ_{ILSS}: 30**	1900	17–33	620
C/C-SiC out-plane*	4 to 2.1	10-30	12	1900	9–18	620
Zerodur	0.1	90	100	2530	1.46	820
Fused Silica	0.55	73	54	2200	1.38	703
Invar	1.2	130	260	8100	10.5	510

Polymeric composites, such as carbon fiber reinforced polymers (CFRPs), offer high specific stiffness and the ability to tailor thermo-mechanical properties via layup design. Their anisotropic behavior and low mass make them attractive for space basee optics, though challenges remain regarding moisture absorption, outgassing, and long-term stability under UV and atomic oxygen exposure. These concerns are further discussed in Appendix A.

Table 2.2: Overview of the specific thermal and mechanical ratios of material properties around 20°C. The values are scaled such that the largest entry in each row lies in the range 10–100, with the corresponding power of ten indicated in the units. D_{ss} represents steady-state thermal distortion, and D_t quantifies how quickly heat-induced distortion dissipates per unit of temperature gradient. [21] [25] [20] [26]

Unit	Material Property		RSP 6065-T6	Invar	Ti-6Al-4V	C/C-SiC
Specific Mechanical properties						
$[10^{-2}\,\mathrm{GPa}\cdot\mathrm{m}^3/\mathrm{kg}]$	E/ρ	Specific stiffness	2.6	1.6	2.6	3.2
$[10^{-2}\,\mathrm{MPa}\cdot\mathrm{m}^3/\mathrm{kg}]$	σ_y/ρ	Specific yield strength	11.7	3.2	19.9	4.2
Thermo-mechanical properties						
$[10^{-6}\,\mathrm{K}^{-1}]$	CTE	Coefficient of thermal expansion	22.6	1.2	8.6	0.1
$[10^{-2}\,\mu m/W]$	D_{ss}	Steady state distortion (CTE/k)	13.4	11.4	128.4	0.7
$[10^{7}\,s/(m^2K)]$	D_t	Transient distortion ($\rho C_p CTE/\lambda$)	3.3	4.7	30.1	0.1

For the structural materials, the key mechanical and thermo-mechanical figures of merit are reported in table 2.2. It summarizes the material property ratios for designing weight-efficient, stiff, and strong structures, as well as materials that remain dimensionally stable under both transient and steady-state thermal loads. In the case of orthotropic materials, the reported values correspond to the in-plane properties. The tabulated values have been rescaled such that the largest entry in each row lies between 10 and 100, with the appropriate power of ten indicated in the units.

C/C-SiC distinguishes itself through its near-zero coefficient of thermal expansion and very low distortion parameters, making it well suited for applications requiring thermal dimensional stability. Ti-6Al-4V offers high specific yield strength, while RSP 6065-T6 provides balanced stiffness. These trade-offs underline why C/C-SiC is of particular interest for the present study.

2.2.3. Challenges encountered Within the CASTT project

Before addressing the use case and its background, this subsection briefly outlines the current developments at TNO which is context for the thesis project.

An initial objective of the CASTT project was to measure the thermal stability of the complete structure with high precision using interferometric techniques during thermal cycling in the TVC. However, one of the key challenges encountered during the project was ensuring the cleanliness of the C/C-SiC structure. This issue primarily stemmed from the following factors:

- The absence of cleanroom facilities and related infrastructure at Arceon, which prevents mitigation of particulate contamination to the level required for compatibility with TNO's cleanroom and vacuum testing environment.
- The surface roughness of the C/C-SiC design, which complicates cleaning procedures due to the possibility of particulates becoming embedded in the surface.

Both of the aforementioned challenges have solutions, which were explored during the course of the project. Nevertheless, the cleanliness requirement remains non-negotiable for most space applications, particularly in the vicinity of sensitive optical instruments such as telescopes. The test facilities, similar to an optical application, run the risk of becoming contaminated. Such contamination can damage the vacuum pump of the thermal vacuum chamber (TVC) or compromise subsequent activities. As such, Appendix B in the materials chapter addresses this issue, discussing its causes as well as viable mitigation strategies.

At the time of writing, the CTE test has been postponed because the requirements for the TVC test could not be met. The project scope has been adjusted to prioritize achieving consistent manufacturing quality at the scale of the test article. The thermal vacuum test will be pursued as part of follow-up activities.

Adhesive testing with EC2216

Due to the fibrous and, relative to metal, hard-to-machine nature of the C/C-SiC material, implementing mechanical connections such as bolted joints is non-trivial. [41] Moreover, given the material's traditional use in high-temperature applications, the performance of adhesive joints is not extensively documented in the literature. For this reason, TNO initiated a preliminary investigation into the performance of adhesive bonding prior to the start of this thesis project.

A rudimentary lap shear test was conducted using both machined and unmachined samples derived from C/C-SiC plate material. The results indicated that, when using a heritage-based bonding procedure, the strength of the bond between C/C-SiC and EC2216 was at least comparable to that of a bond between aluminium and EC2216.

EC2216 is a two-part epoxy adhesive, qualified for aerospace use by 3M, with which TNO has extensive prior experience. Therefore, for the purposes of this thesis, it is assumed that adhesive bonding using EC2216 is a viable approach for the structural integration of C/C-SiC components.

Delamination in C/C

A key motivation behind the aforementioned re-scoping of the project is to demonstrate consistent manufacturing capability for C/C-SiC components with a diameter of 200 mm. At the time of writing, the revised primary objective focuses on mitigating delamination and wrinkling—issues that were observed during the pyrolysis phase of the manufacturing process.

Significant progress has been achieved by altering the material layup from a conventional 0°/90° orientation to a ±45° configuration. This adjustment has, at first sight, successfully eliminated the observed defects. However, at the time of writing, the final results of the siliconized version had not yet been subjected to CT scanning.

It is important to note that such a change in layup inevitably affects both the mechanical and thermal properties of the material, which must be considered in subsequent design and analysis efforts.

2.3. Optical communication developments at TNO and FSO

TNO has been developing the LCT use case and similar systems on various platforms since at least 2018 [36], resulting in substantial experience and the first successful LCT launched onboard Nordsat in April 2023 [42].

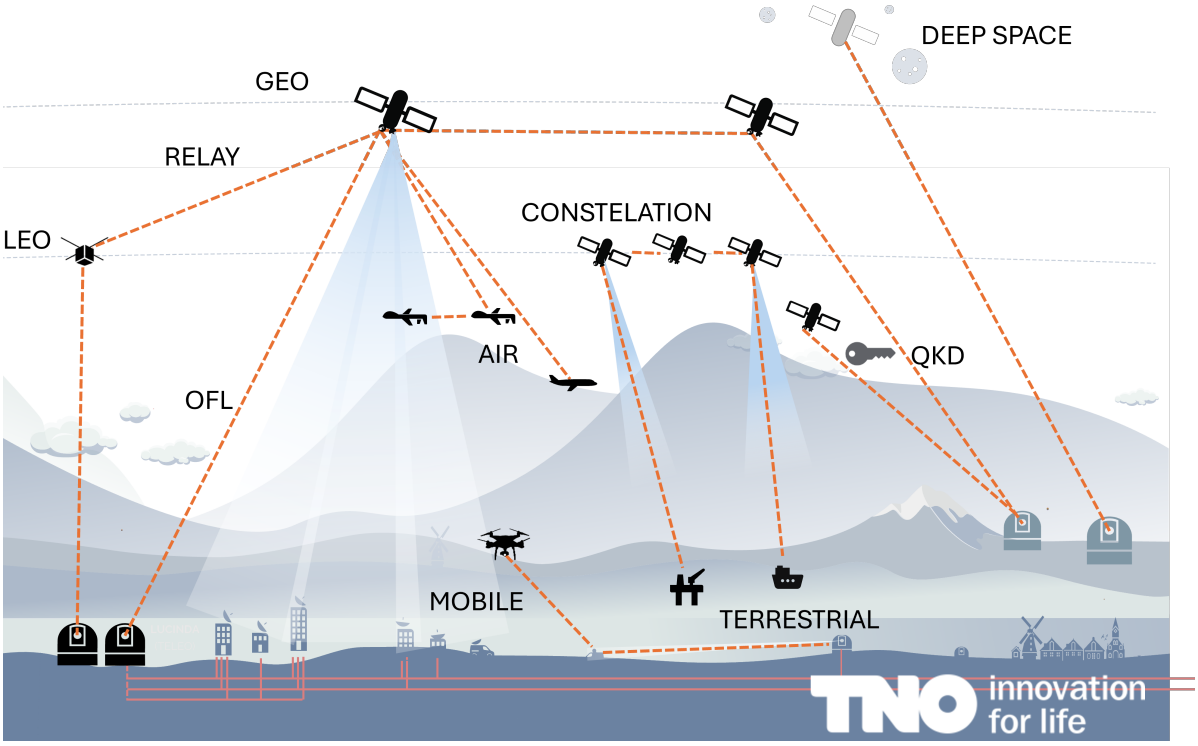

Figure 2.5: The laser communication network platforms as envisioned and in part being developed by TNO.

One of TNO's earlier internal projects investigated a 200 mm diameter telescope design. Completing a trade-off including the sensitivity to thermal distortions, for different optical designs. One concept was abandoned due to the lack of commercially viable low-CTE materials at the time. C/C-SiC may address this. The implications and relevant results of these projects are addressed in this section. Because the optical analysis done at the time is used to create performance requirements.

The study compared several candidate architectures—both on-axis and off-axis—evaluated, which is a common categorization; an example is shown in Figure 2.6. The work focused primarily on their sensitivity to rigid body motion (RBM), nominal wavefront error, cost, and envelope volume.

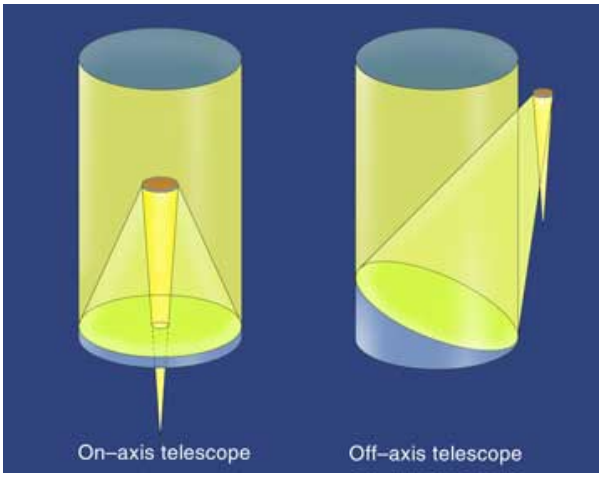

Figure 2.6: Schematic representation of the fundamental difference between on- and off-axis telescopes [6]

Following this initial survey, a focal Cassegrain design emerged as a promising candidate due to its compactness and symmetry. However, subsequent analyses identified a key shortcoming: the optical

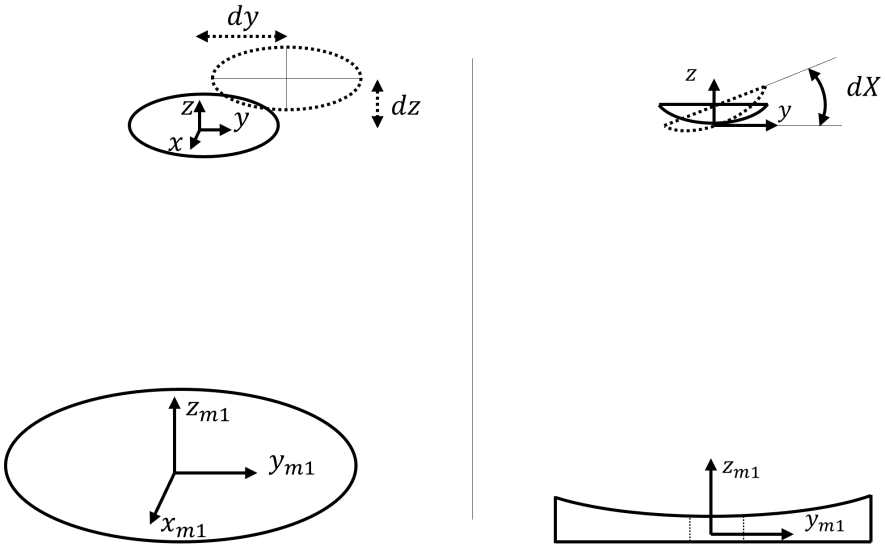

Figure 2.7: Schematic representation of relative rigid-body motions between M1 and M2, illustrating translations along the y (dy)- and z (dz)-axes and rotation about the x (dX)-axis.

performance is highly sensitive to thermally induced misalignments. Especially in the axial direction of the primary (M1) and secondary (M2) mirrors. Under anticipated orbital gradients, the Cassegrain system's WFE exceeded acceptable limits unless constructed from a material with a low CTE, such as silicon carbide (SiC). At the time, SiC was considered commercially unfeasible due to the cost and manufacturability for this application.

The mentioned axial sensitivity is one of a number of useful results. The axial sensitivity refers to the relative motion between the two mirrors. Since each has an assigned axis system and origin, three relative translations and three relative rotations can be distinguished. This is schematically shown for translations in the y- and z-directions and for rotation about the x-axis, ΔX, in Figure 2.7. These deformations are generally measured in micrometers (μm) or microradians (μrad). The completed optical analysis reports the effect of a shift or rotation of $1, \mu m$ or $1, \mu rad$ on the WFE of the on-axis optical design.

This trade-off highlights a potential role for C/C-SiC as an enabling material because of its low CTE. Consequently, the Cassegrain design—initially set aside is reconsidered in this project and adopted as the baseline concept for this study, supported by ongoing developments within TNO, FSO and the CASTT project.

It is important to emphasize that this optical architecture was fixed before the scope of this thesis began. In light of this, detailed optical engineering such as lens configuration, tolerancing, or stray light control falls outside the scope of the present work. Nevertheless, the availability of prior sensitivity data (e.g., mirror displacement versus WFE) ensures that optical performance implications of thermo-mechanical deformations can still be reasonably assessed. This enables the present research to focus on evaluating the structural and thermal behavior of a C/C-SiC telescope tube and assessing its feasibility in supporting high-performance LCT systems under representative orbital load cases.

2.3.1. Terminal Concept Selection

To define realistic boundary conditions for the thermo-mechanical analysis, the design presented in this thesis adopts the dimensional characteristics of the RS-80 laser communication terminal, currently under development by FSO Instruments in collaboration with TNO. FSO Instruments is a Delft-based company aiming to commercialize free-space optical communication systems, and the RS-80 represents one of their key product lines for low Earth orbit applications [43].

The RS-80 serves as a representative terminal class not only in terms of aperture diameter (approximately 80 mm), but also in terms of enclosure size, surface area, and integration constraints. These characteristics

directly influence the thermal boundary conditions of the structural components, particularly the radiative input from the orbital environment. Additionally, the external dimensions of the RS-80 nacelle constrain the packaging of optics, electronics, and structural supports, making it a realistic reference.

It should be emphasized, however, that the optical design adopted in this thesis differs significantly from that of the RS-80. The present study focuses on a Cassegrain-type two-mirror system, selected for its axial symmetry making it suitable for a C/C-SiC structural design. Despite these architectural differences, if the aperture diameter and output beam characteristics are the same, the telescope can be treated as a system component whose output is functionally interchangeable. From a system-level perspective, the rest of the terminal (e.g., fiber coupling, pointing assembly) would not require fundamental redesign.

Nonetheless, in real-world applications, the difference in optical layout leads to substantial changes in the telescope's envelope volume, mass distribution, and mounting geometry. These, in turn, significantly influence the dynamical and thermal behavior of the full terminal assembly. Hence, while the optical output may remain comparable, the structural and thermal behavior of the terminal is strongly affected by the selected telescope configuration.

By tying the system-level constraints to the RS-80, the thermo-mechanical assessment of the C/C-SiC telescope stays anchored to a realistic, industry-relevant baseline.

2.4. Laser communication

Before addressing the requirements, the chosen LCT and telescope are placed into context in the following section. The background information relevant to the project as a whole is reviewed, providing insight into the use of the telescope within the LCT and how its performance is measured. This information enables the formulation of a set of requirements. The section proceeds top-down, gradually zooming in on the LCT and its telescope.

There are various visions of what a network might look like, but it will likely consist of many different links between many different types of platforms. Where a platform is a vehicle or ground station that uses an LCT to communicate.

In space, the platforms can be distinguished by their orbit. in low Earth orbit (200–2,000 km), medium Earth orbit (MEO, 2,000–$\tilde{3}$5,000 km), and geostationary orbit (GEO, $\tilde{3}$6,000 km). GEO platforms are especially suited for relay satellites due to their large field of view. On Earth, in the short term platforms could range from aircraft to buses. [44]

2.4.1. Low Earth Orbit applications

Before moving on to the specific implications for the telescope the environment and primary use cases for satellites in LEO are discussed in the following paragraph.

Low earth orbit is the most used orbit in space. In a laser communication satellite network, the low Earth orbit environment presents both unique opportunities and challenges. Satellites in LEO, benefit from low latency and high data throughput due to their proximity to the Earth's surface. However, they move rapidly relative to the ground, requiring fast and precise beam steering to maintain inter-satellite and ground links. The environment is also characterized by fluctuating thermal conditions, increased atomic oxygen exposure, and a high density of orbital debris, all of which impact the performance and durability of optical components.

In an Earth observation(EO) satellite, the laser communication terminal is mainly used to send collected data back to the ground. Since the satellite's orientation is driven by imaging needs, the terminal only points toward a ground station during planned downlink periods. One example can be found on the sentinal 2A satellite as shown in Figure 2.8.

The location of the terminal on the satellite is a constrained choice. In case of the sentinal 2A, the terminal is put on top or in the zenith direction. This is clear in the configuration shown in figure 2.8. Because the EO instruments need to look down to Earth i.e., nadir direction, that side is a coveted space used by most instruments. Combining with the fact that the relay satellite, which in this example is used to transfer the data, is in geostationary orbit ($\tilde{3}$6.000 kms) and thus above the sentinal 2A makes for a compelling argument to put the FSOC terminal on the zenith side. In other applications, this decision

is more complicated and might even change over the design cycle. [7,20,45–47]

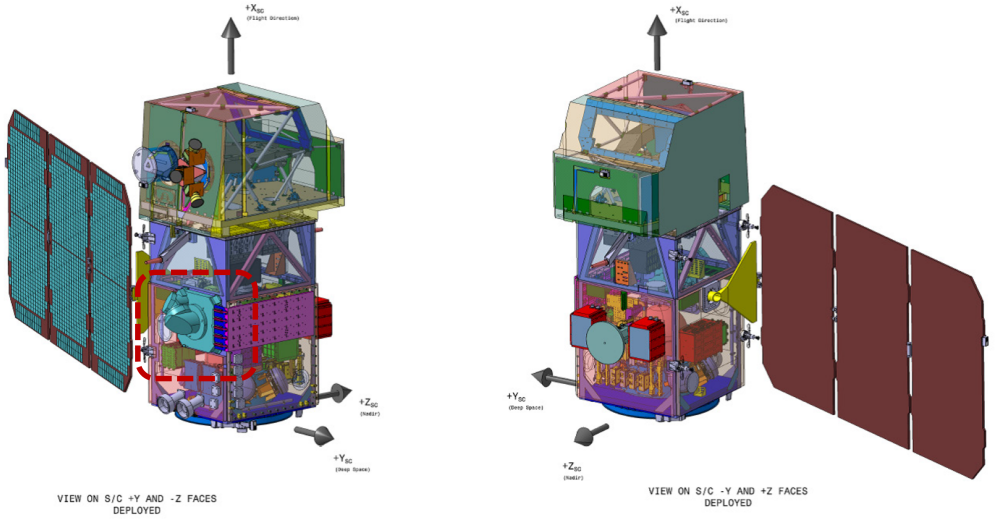

Figure 2.8: Shows the flight configuration of the Sentinel 2 satellite. On the left the zenith side with the LCT in turquoise encircled in red and on the right the Nadir side. [7]

In large low Earth orbit constellations, such as planned by the US department of defence, laser communication terminals are used to link satellites directly with one another. This allows data to be relayed through space. Terminals in these networks need to track nearby satellites and maintain stable links while moving at high speeds. Unlike terminals on Earth observation satellites, which mostly point toward the ground, these are designed to operate continuously as part of a wider system. SpaceX has already deployed 4 experimental spacecraft of this kind using TESAT terminals. [48] This is all to show that even within the LEO environment there are many different objectives for satellites.

2.4.2. A free space link

The objective of a single link between two platforms, e.g., 2 LEO satellites or a plane and a GEO satellite is to transfer data from 1 platform to the other. Be it quantum keys, private banking data, military intel or a YouTube video. The performance of a link is generally calculated by a link budget. Which summarizes and simplifies all the facets involved in the link into different factors, allowing the user to make a starting calculation on the required power and accuracy of different parts of the link. For example the receiver aperture, i.e. the diameter of the primary mirror of the telescope.

In this project the link and thus required power and aperture are chosen by emulating the current project with FSO which helps develop their RS-80 LCT. However to understand the context that influence that decision and its effect in the LCT application the following section will review the relevant parts of the link budget and show a specific example relating the thermal deformation of the telescope to the detriment on the system level.

A detailed formulation of the link budget is provided in the link feasibility study by Kaushal et al. [27]. In this example, the received optical signal power at the photodetector at the receiver side is computed using the so-called range equation:

$$P_R = P_T \cdot G_T \cdot \eta_T \cdot \eta_{TP} \cdot L_s \cdot G_R \cdot \eta_R \cdot \eta_\lambda \tag{2.1}$$

where P_T and P_R represent the transmitter and receiver optical power, G_T and G_R the transmitter and receiver antenna gains, η_T and η_R their optical efficiencies, (L_s) the space loss factor, η_{TP} the pointing loss, η_λ the narow band filter (NBF) transmission loss.

These parameters are categorized into transmitter-side parameters (P_T, G_T, η_T, η_{TP}), and receiver-side parameters (P_R, G_R, η_R). This formulation helps quantify how each subsystem contributes to overall link

performance and is crucial for assessing link feasibility under various mission scenarios. The example mentioned earlier estimates the link budget for a 40.000 km link with 30 cm receiver diameter and a 5.94 and 9.42 cm transmitter diameter. The values used in that example typical for a GEO link are reported in Table 2.3

Table 2.3: Link budget parameters and results for a GEO uplink at $\lambda = 1064$ nm and $\lambda = 1550$ nm, showing both linear and dB values for each parameter, from [27]

Parameter	$\lambda = 1064$ **nm**		$\lambda = 1550$ **nm**	
	Linear	dB	Linear	dB
P_T [mW]	3000	34.77	3000	34.77
G_T [–]	3.13×10^{10}	105.00	3.64×10^{10}	105.61
η_T [–]	0.65	-1.87	0.65	-1.87
η_{TP} [–]	0.9	-0.45	0.9	-0.45
L_s [–]	4.48×10^{-30}	-293.48	9.50×10^{-30}	-290.21
G_R [–]	6.88×10^{11}	118.37	3.24×10^{11}	115.11
η_R [–]	0.7	-1.54	0.7	-1.54
η_ℓ [–]	0.7	-1.54	0.7	-1.54
P_R [W]	8.97×10^{-8}	-40.74	9.72×10^{-8}	-40.12
$P_{R,\text{min}}$ (LDPC) [W]	9.97×10^{-9}	-50.01	6.91×10^{-9}	-51.59
Link Margin (LDPC) [dB]	–	9.27	–	11.47

Before moving on to the fiber coupling example, the different components of the LCT are reviewed. As is clear from the range equation (2.1) and the mentioned example there are many facets involved in the successful communication link both within a single LCT and outside of it in a whole network. A schematic of the optical components that form a version of an LCT as provided by Badas et. al. [8] is shown in Figure 2.9.

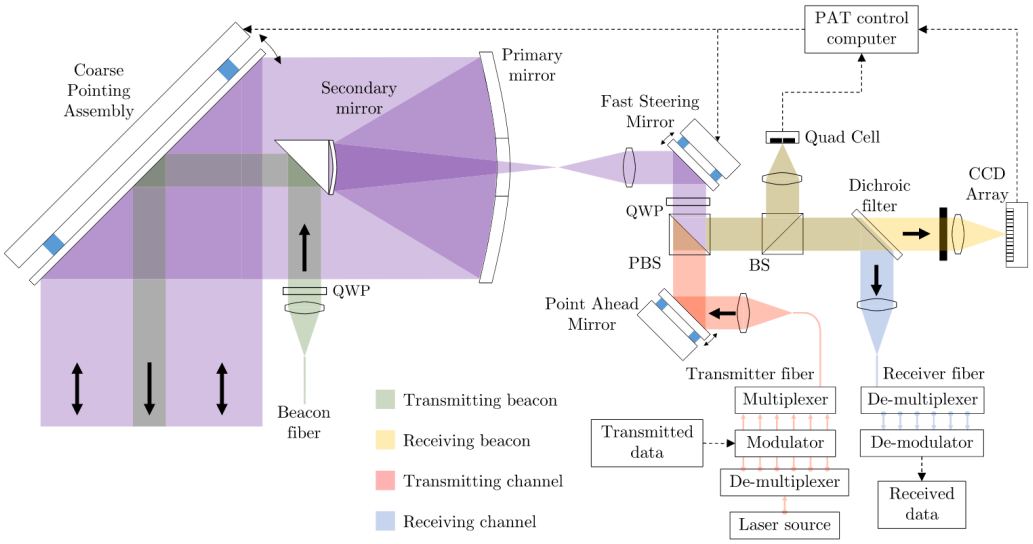

Figure 2.9: General system diagram for satellite FSOC transceiver terminal. The lenses shown are a simplified representation of lens assemblies. Colors not stated in the legend are combinations of others (BS, beam splitter; CCD, charge-coupled detector; PAT, pointing, acquisition, and tracking; PBS, polarization beam splitter; QWP, quarter wave plate), by (Badás et al., 2023) [8].

The LEO LCT will function as a so called tranceiver which is combination of the receiving and transmitting parts of the link. Meaning it can both send and receive. The telescope subsystem and its size directly effect the G_T and G_R of the link. Both of them being functions of the diameter and the obscuration ratio. First the equation

$$G_T = \left(\frac{\pi D_T}{\lambda}\right)^2 \tag{2.2}$$

Which when substituting the Area = $\pi D_T^2/4$ and taking into account the obscuration ratio. Results in the following equation given an on-axis gain of gaussian beam with central obscuration. [49]

$$G_T = \left(\frac{4\pi A}{\lambda^2}\right) \cdot \left[\frac{2}{\alpha_T^2}\left\{e^{-\alpha_T^2} - e^{-\alpha_T^2\gamma_T^2}\right\}^2\right] \tag{2.3}$$

Where α_T is the truncation ratio which is defined as the ratio between the gaussian beam diameter and spot diameter. Which function of g γ_T which is the obscuration ratio.

$$G_R = \left(\frac{\pi D_R}{\lambda}\right)^2 \cdot (1 - \gamma_R^2) \tag{2.4}$$

For the use case of interest i.e. the telescope structure this means the gains would increase with a lower obscuration ratio and a larger diameter. Given the diameter is already determined the obscuration ratio is minimized.

Altough, the gain equations place the telescope or antenna in the context of the whole link and clearly show that this is a small piece of the whole LCT puzzle. It is not a very intuitive explanation connecting the thermo-mechanical performance increase claimed in the introduction to the optical link. In reference to the range equation the actual G_T is primarily linked to the beam divergence angle with an inverse square relation. In addition the efficiency is in the example is assumed as a value from experience. Both of these are also effected in a different manner by the telescope which is not fully captured in the antenna gain parameter.

Fiber coupling example:
The following example provides a direct connection between the thermo-mechanical behavior of the telescope and the performance of the whole LCT. One of the crucial performance losses within the whole system is fiber coupling efficiency. Some simplifications w.r.t. to the real case are made in the example.

At the receiver end, when the link is established, a part of the light (beam) from another LCT is collected through the telescope. Hence, a larger aperture also results in a larger antenna gain; it collects more light.

In the ideal case, the incoming light would have a completely flat wavefront. This results in the well-known Airy disk distribution of light at the fiber in the LCT. Different shapes of the wavefront propagate through the telescope and the rest of the optical components, e.g., a beam splitter.

There are many factors that can distort the received light, such as atmospheric turbulence or system vibrations. Sources of thermal and mechanical origin are summarized in [8]. For the telescope specifically, a schematic interpretation of these effects on the focal spot is shown in Figure 2.10.

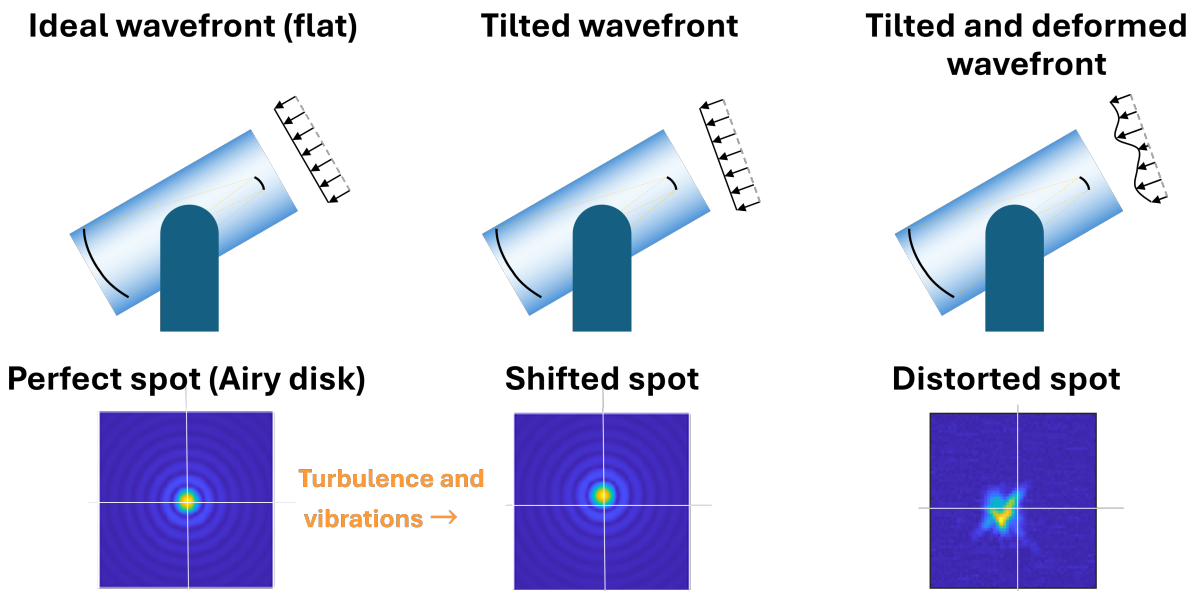

Figure 2.10: Shows a schematic of the light spot on the detector and how it is affected by distortions.

One of the LCT's main functions, on the receiver side, is to couple as much incoming light as possible into a single-mode fiber. More light in the fiber means higher received power, improving the signal-to-noise ratio, lowering the bit-error rate, and ultimately increasing data throughput—put simply, more light equals faster, more reliable data transfer.

A typical single mode fiber has a diameter of roughly 10 μm. A schematic of the fiber and its coupling efficiency as effected by an angle error is shown in Figure 2.11.

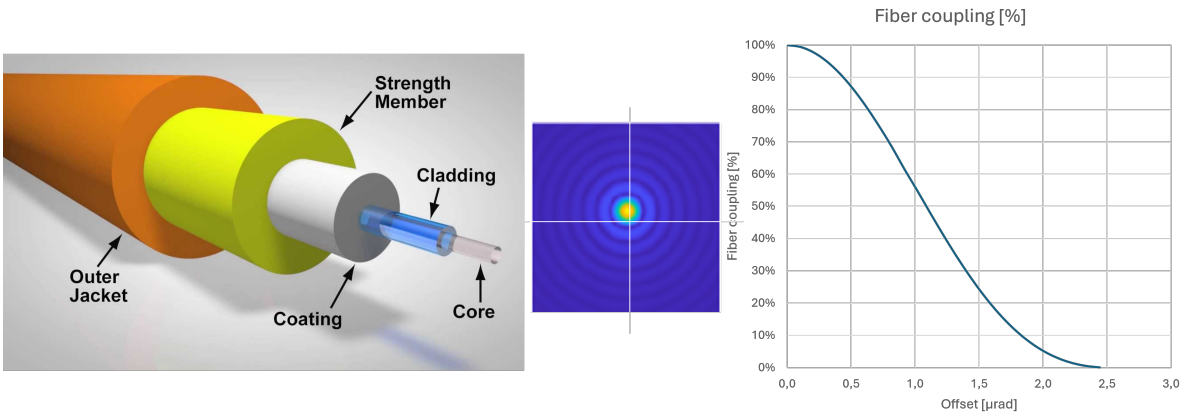

Figure 2.11: The small size of the fiber requires extremely precise (μrad) pointing to maximize coupling efficiency

The distortion shown in the light spot at the fiber in both Figures 2.10 and 2.11 can be described by so called Zernike modes. For the purposes of this section it is enough to know the following: The modes are a set of orthogonal polynomials in a radial axis system defined on the unit circle. They form a basis which can be used to describe planar deformations but also optical aberrations by summing them.

Both the deformations and RBMs of the mirrors can be described by summing these Zernike modes. A relation of a few of the first modes to the changing spot size and shape can be seen in Figure 2.12. The Tip and Tilt modes on the second row correspond to rotations of the mirror about the x and y axis. Going back to Figure 2.7, it would $dX \wedge dY$. A larger rotation would result in the center of the spot being removed further from the center of the receiving wire. As shown in 2.11, this quickly decreases the fiber coupling efficiency.

From these figure, it is clear that the deformations spread the light over a larger area missing the fiber causing a decrease in fiber coupling efficiency.

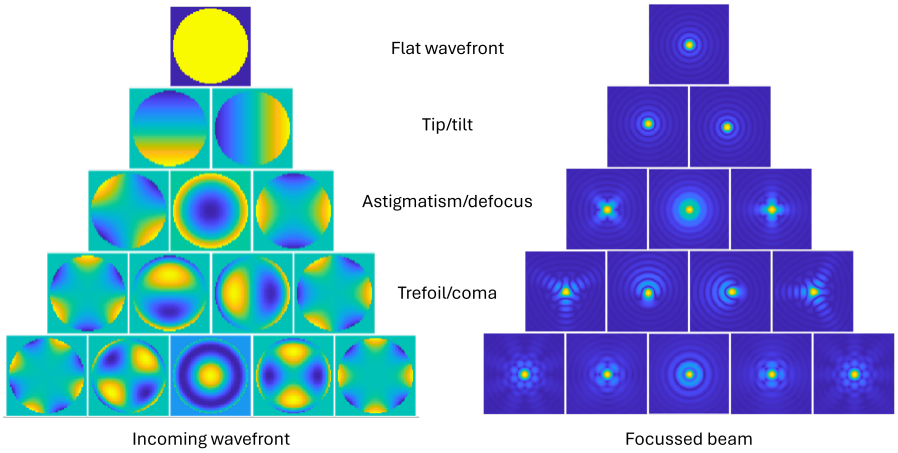

Figure 2.12: The relation between the first 15 Zernike modes and the effect on the spot at the receiving end. [9].

The other rigid body motions induce different types of errors. For example, in a Cassegrain design, a defocus may occur due to an RBM in the z-direction. The combined effect of thermo-mechanical behavior is more complex than these single modes can describe. One could imagine that the mirror not only displaces but also deforms or contains manufacturing defects. Hence, in practice, the focal spot resembles the distorted spot shown in Figure 2.10.

A complete analysis of thermo-mechanical behavior would also include an optical analysis. However, as mentioned, that discipline is outside the scope of this work and is instead addressed by relying on analyses completed in previous projects. The resulting requirements take the form of a RBM displacement and are described in section 2.6.

2.5. Mitigation by CTE matching

Preventing these distortions in telescopes is a common issue in space missions. A sensitive example can be found in the ARIEL mission, which shows the importance of material choices within thermal design strategy. It is an extreme case compared to the LCT telescope in terms of thermo-mechanical stability. Which leads to a very advanced thermal design driven by the sensitivity of the optics. Or as the consortium put it : "One of the main objectives of the ARIEL cold PLM thermal design is to ensure as much as possible an isothermal environment for the Telescope Assembly" [50]. The application is very different, but the main thermal challenge stems in part from a similar objective, i.e., gathering light.

Its concept design is a clear example of CTE matching, which is a commonly used strategy in optical structures. The strategy works on the principle that if every part, including the optics, has the same CTE, everything expands equally when the temperature changes isothermally. In the ideal case, this results in no relative deformation and no induced stresses due to differences in CTE. This would mean the whole optical design scales in all dimensions, effectively without changing any of its characteristics.

Note that this strategy works best if the temperature distribution is isothermal, i.e., uniform across the entire structure and the optics. This is facilitated by the high thermal conductivity of aluminum used in optical structures. For C/C-SiC, however, there are only a limited number of examples of optical components made from this material. Consequently, the mirrors must be manufactured from a different material. If the matching strategy is applied, the CTE of the mirror material must fall within the tunable range of C/C-SiC. To what extent this is feasible will be addressed in part by the analysis presented here. The material properties relevant for CTE matching are summarized in Table 2.4 below:

Table 2.4: Thermal properties of selected materials used in the thermoelastic modelling [5, 21–24, 28]

Material	CTE [μm/mK]	Conductivity k [W/mK]	Specific Heat c_p [J/kgK]	Density ρ [kg/m^3]
	Secant CTE	Thermal conductivity	Specific capacity	Mass per unit volume
Aluminium RSA-6061-T6	22.6	169	900	2700
Titanium (Sheet Timet-550)	8.8	21.9	522	4500
C/C-SiC in-plane	1.1 to -1	17–33	720–750	1900–2200
Zerodur	0.1	1.46	820	2530
Fused Silica	0.55	1.38	703	2200
EC2216	102	0.427	-	-

When using C/C-SiC, CTE matching ensures that all parts expand equally under temperature changes, minimizing deformation. Since its thermal conductivity is lower than aluminum, keeping the structure isothermal is more challenging. But the decrease in CTE is larger and will compensate. Using this strategy helps to fulfill the requirements covered in the next section

2.6. Performance Metrics and Requirements

Given that this project focuses on the effect of uncertainty in material properties on telescope performance, the conventional design approach—where a design must meet fixed requirements does not cover the full intentions. Nonetheless, an interesting example, of a preliminary requirement set for the NFIRE C/C-SiC telescope can be found in literature [19], and is reported in Table 2.5. While not definitive, these requirements offer a valuable reference point for evaluating and comparing models and alterations to them.

Parameter	Specification
Mass	$\leq$ 2 kg
Structural resonant frequency	$>$ 160 Hz
High Random Vibration Loads	–
Telescope aperture	65 mm
Magnification	10
Field of view	$\pm$0.3°
Wavefront quality	$\leq \lambda/30$ RMS
RX / TX axis stability	$\leq$ 5 μrad
Straylight	$< 10^{-9}$
Temperature range	−30°C to +65°C
Lifetime	10 years

Table 2.5: Optical system specifications for a preliminary design of the NFIRE LCT, reported by A. Schöppach et al. [19]

The comparison between models is ideally limited to a small set of critical performance values. When these are combined with sensitivity data from the earlier conceptual study, they provide insight into how much rigid body deformation can be tolerated before optical performance degrades beyond acceptable limits.

Using the wavefront quality specification of $\lambda/30$ RMS as a performance bound, an upper limit for tolerable rigid body deformation can be derived. This is where the optical analysis of the prior project comes in. As mentioned, it quantified the relation between the RBMs and the WFE. This was achieved by an optical analysis in ZEMAX.

Where the results are reported in terms of root mean squared wavefront error, i.e., an average distortion of the wavefront w.r.t. an expected wavefront. This value takes the unit in nanometers $10^{-9}m$ (nm). For example in case of the Wavefront quality $\leq \lambda/30$ this value would be equal to 51.67 $nm\ RMS$.

The sensitivity data is presented in Table 2.6, and assuming statistically orthogonal deformation modes, the total RMS wavefront error due to rigid body motion can be approximated via:

$$\text{WFE} = \sqrt{\left(s_{Dxy} \cdot \Delta Dxy\right)^2 + \left(s_{Dz} \cdot \Delta Dz\right)^2 + \left(s_{Rxy} \cdot \Delta Rxy\right)^2} \tag{2.5}$$

Where s_i denotes the sensitivity (in $nm[RMS]\ /\mu m\ or\ \mu rad$ of RBM) of the wavefront error to each rigid body degree of freedom, as shown in Table 2.6, and Δi is the corresponding applied rigid body motion.

Table 2.6: Rounded-down values from the alignment table (sensitivity values) including the compensation done by the lens. Translation values converted from mm to μm (WFE halved) and rotations converted from degrees to μrad.

Mirror	Rigid body motion	WFE RMS (nm)	focus compensation (nm)
M1	Dx [1 μm]	10.5	0
	Dy [1 μm]	10.5	-2
	Dz [1 μm]	70.5 (7.7)	-67
	Rxy [1 μrad]	1.43	0
M2	Dx [1 μm]	10.5	0
	Dy [1 μm]	11	0
	Dz [1 μm]	70.5 (7.7)	-68
	Rxy [1 μrad]	1.43	0

As an example, let us consider a hypothetical case with the following rigid body misalignments:

$\Delta Dy = \Delta Dx < 2\ \mu$m, $\Delta Dz < 0.5\ \mu$m, $\Delta Rxy < 1 \mu rad$,

Read: "a maximum horizontal shift of the mirrors of 2 micron, a maximum vertical shift of 0.5 micron, and a maximum rotation of a microradian."

Given the sensitivities for Rx and Ry and Dx and Dy we can also take the RMS of those, simplifying the equation. :

$$\text{WFE} = \sqrt{(10.5 \cdot 2)^2 + (10.5 \cdot 2)^2 + (0.5 \cdot 70.5)^2 + (1 \cdot 1.43)^2} \approx 46 \text{ nm RMS} \tag{2.6}$$

This result, $\text{WFE}_{\text{M1}} \approx 46$ nm, is below the $\lambda_{1550}/30 \approx 52$ nm threshold for a wavelength of $\lambda = 1550$ nm, indicating that the telescope design would be considered optically stable under the assumed deformation scenario, ignoring the focus compensation provided by the lenses. Including that compensation, the sensitivity to Dz drops to $7.7\ nm\ RMS/(\mu m)$ resulting in :

$$\text{WFE} = \sqrt{(10.5 \cdot 2)^2 + (10.5 \cdot 2)^2 + (0.5 \cdot 7.7)^2 + (1 \cdot 1.43)^2} \approx 30 \text{ nm RMS} \tag{2.7}$$

A summary of practical performance targets based on this reasoning is listed in Table 2.7. These metrics can be used to assess the sensitivity to material properties and design changes.

In addition to the performance parameters, a key requirement is trivially for the parts not to break. In a general case the materials should be stressed only within their yield limit. In the thermo-mechanical discipline the highest stresses are found in the highest, lowest, or largest gradient temperature cases.

2.6.1. Minimum First Eigenfrequency Requirement

To avoid dynamic amplification during launch, components are often required to have a first natural frequency above a specified minimum, typically above 100 Hz for secondary structures. This requirement ensures that the component behaves more rigidly relative to the primary input frequencies of the launch environment. It is often verified using finite element modal analysis during the early design stages. Meeting this criterion reduces the risk of resonance.

Altough in case of the LCT additional requirements might be set because of the required rotations and stability during operation. The extremely accurate pointing is in large part enabled by an active control system which has to mitigate resonance effects from an array of sources. Hence introducing noise or other sources of instability needs to be avoided.

The coming chapter reports how the environments in which the LCT telescope needs to perform are modeled. In addition to how they are derived or approximated. This chapter can be concluded by summarizing the requirements/performance targets for the telescope, which can be found in Table 2.7.

Table 2.7: Performance limits for the telescope

Parameter	**Focal correction**	**No correction**
Mass	Minimized	
Volume	Minimized	
First eigenfrequency (structural)	Maximize ($\geq$ 100 Hz)	
Strength compliance	Survive all load cases; per-part stresses $\leq$ allowable (margin of safety $\geq$ 0)	
Operational rigid body translation (Dx, Dy, Dz)	$< 1, 1, 3$ μm	$< 0.5, 0.5, 0.4$ μm
Operational rigid body tip/tilt (Rxy)	< 8 μrad	< 5 μrad

Both of the budgets above are calculated to leave 40, nm, RMS margin for surface deformation. Using low-CTE materials for M1 and M2 will help reduce the WFE induced by surface deformation. However, the optical analysis needed to directly link these effects is outside the scope of this project. Therefore, the larger portion of the total 50, nm, RMS budget is allocated to surface deformation.

3

Laser communication use case: a near-zero CTE Beam expander

The goal of this chapter is twofold: first, to explain the selection process by which the relevant load cases are derived, and second, to establish the requirements that follow from the chosen terminal.

To assess the effect of C/C-SiC's material properties on the performance of a Cassegrain telescope designed for the RS-80, additional information is required. Specifically, the load cases that describe the extremes of the thermal environment encountered in LEO, as well as a design that can be modeled.

The first part of this chapter therefore explains how the load cases are derived, starting with the conceptual mission profile and orbit selection and resulting in five thermal cases supplemented with a MAC curve case to represent launch conditions. The model geometry, whose design is based on the C/C-SiC LSI process, is presented in the next chapter.

During the lifetime of an LCT telescope, a multitude of environments are encountered. All of which it has to survive, and, after surviving, in which it has to perform. These environments can be represented by load cases. Given the main subject of the case study is limited to a telescope structure for space-based FSOC applications, the environments discussed in this chapter are scoped to that application. Answering in part the question posed below and in the introduction.

What is the objective of the LCT telescope, how can its performance be quantified for thermo-mechanical assessment, and how is the operational environment defined, incorporated, and reported within the analysis?

As mentioned in Section 2, the terminal is still in development and may serve as a secondary component on the satellite. Consequently, the orbit around Earth that it will experience is not yet known, nor is its location on the satellite or the orientation of the satellite to which it is attached. This uncertainty poses a significant challenge, as both the thermal and mechanical loads depend on these three variables. For instance, each launcher—or even each launch—has its own profile, and each satellite has its own thermal environment. If the terminal is designed to be suitable for any possible situation, the resulting requirements become overly stringent due to overlapping extremes. The challenge addressed in this chapter is therefore to strike a balance between conservatism in the load cases and avoiding unnecessary over-constraining.

3.1. Impact of Orbit environment on Optical Performance

The coming generation of LCTs is marketed as off-the-shelf products, and therefore they must withstand the full range of orbital conditions considered. This dictates the operational and survival environments in which the telescope must perform, from which most requirements are derived, along with other relevant information.

The following section reviews the necessary information used to model these environments. The primary interest lies in the thermo-mechanical behavior of the structure and its potential performance

benefits. Accordingly, the thermal environment is discussed first. However, before orbit is achieved, the system must also endure rocket launch conditions, which impose significant mechanical loads and must therefore be considered as well. This is addressed in the subsequent part.

3.1.1. Thermal Environment in Orbit

In space-based systems, radiation is one of the primary methods of heat transfer. Due to the vacuum of space, convective heat transfer is absent, and conduction is limited to within and across structural interfaces. As a result, thermal radiation plays a central role in shaping the spacecraft's thermal environment. Although it does not govern all thermal behavior alone, an accurate representation of radiative exchange is essential, especially for components with high thermal sensitivity, such as precision optics and laser communication terminals.

A correct understanding of both external radiative sources and internal heat dissipation is critical to predicting temperature distributions and maintaining structural and optical performance. This section outlines the primary environmental and internal contributions to the spacecraft thermal environment, which form the boundary conditions for the radiation exchange model.

Orbital environment

In orbit, the spacecraft experiences alternating periods of solar exposure and Earth-shadow eclipses, with eclipse durations typically ranging from a few minutes to up to 45 minutes depending on the orbital parameters. A geometric schematic of the orbit and its parameters, including an eclipse envelope, is shown in Figure 3.1.

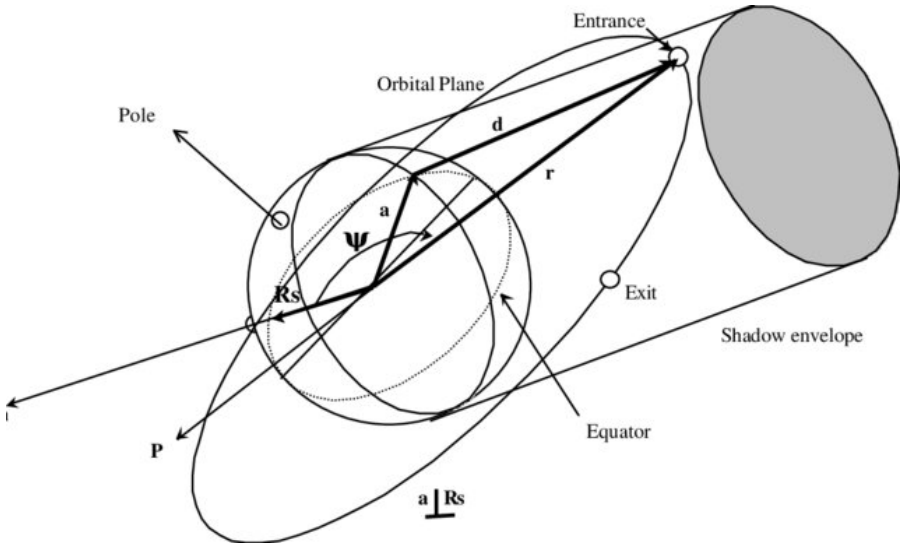

Figure 3.1: Schematic of orbital parameters and the Earth's shadow through which the satellite travels, from [10].

The parameters shown in the eclipse geometry diagram describe the spatial relationship between the satellite, the Sun, and the Earth at the points of eclipse entry and exit. They are used to formulate the shadow function and determine the satellite's position in relation to the Earth's cylindrical shadow. These definitions are as follows:

- $\mathbf{R_s}$: Sun vector, position of the Sun with respect to the Earth's center.
- $\mathbf{r}$: Satellite position vector with respect to the Earth's center.
- d : Component of $\mathbf{r}$ parallel to the Sun vector $\mathbf{R_s}$.
- a : Component of $\mathbf{r}$ perpendicular to the Sun vector $\mathbf{R_s}$.
- Ψ : Angle between the Sun vector $\mathbf{R_s}$ and the satellite vector $\mathbf{r}$, given by

$$\cos\psi = \frac{\mathbf{r}\cdot\mathbf{R_s}}{rR_s}.$$

- **Pole** : Direction of the Earth's rotational axis.
- P : Projection of the orbital plane in the direction perpendicular to $\mathbf{R_s}$, used in eclipse entry/exit conditions.
- **Entrance / Exit** : Locations in the orbit where the satellite enters or leaves the Earth's shadow zone (cylindrical model of the umbra).
- **Shadow envelope** : Cylindrical region extending from the Earth opposite to the Sun, representing the total eclipse zone.

The thermal conditions during the orbital phase are influenced by the listed external sources. A schematic overview is provided in Figure 3.2:

- *Direct Solar Flux:* The Sun's radiation at one astronomical unit (AU), is on average 1366 W/m^2 with a seasonal variation due to Earth's elliptical orbit. It ranges between 1322 end 1414 W/m^2
- *Planet-Reflected Solar Flux (Albedo):* Earth's albedo, averaging around 0.3, reflects part of the incoming solar radiation. The albedo effect varies with surface type; snow and ice reflect more than oceans or vegetation. The eclipsed side of the earth obviously does not reflect any radiation. it ranges between 0 and 0.5.
- *Planet-Emitted Infrared Radiation:* Earth continuously emits infrared radiation with an average intensity of approximately 237 W/m^2. This flux depends on surface temperature and atmospheric conditions. It ranges between 150 and 350 W/m^2

The information values above, as well as a selection criteria for Hot and Cold case values and the correlation between albedo and planet infrared, is reported by [51].

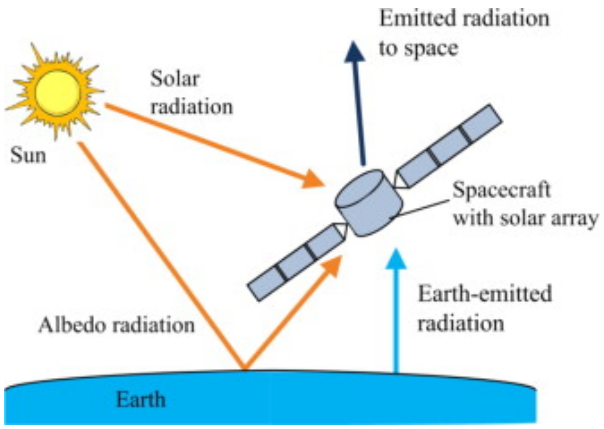

Figure 3.2: Schematic of radiation input and output for an Earth-orbiting satellite, from [11].

Internal heat dissipation

The satellite generates internal heat through operational equipment, including onboard electronics and laser systems. Effective thermal management of these internal heat sources is essential to prevent temperature-induced structural deformations, which may affect pointing stability, optical alignment, or overall system performance. The extent of this generation is logically dependent on the satellite, and the effect on the LCT is dependent on its location.

The internal heat dissipation can be modeled by an energy source or a model artifact at a certain temperature. The range of dissipation power depends on the electronics and operational state. For the telescope the effect is more nuanced because the design also affects whether there is a strong conductive or radiative coupling.

In the load cases the temperature/heat dissipation is accounted for by setting the terminal nacelle to a certain temperature. For deformation investigations this will suffice, but in case of thermal control more detail might be needed. This does not suffice for a transient analysis in which the source needs to be accounted for.

The satellite

Given that the terminal is sold off-the-shelf, the satellite can be of any type. Hence, its surface properties and shape are unknown; these affect the thermal-radiation input of the LCT through reflection and infrared emission. Additionally, there is a conductive connection between the LCT and the satellite through its bearings, power supply, structure, or a combination of these. The radiative connection depends strongly on the design of the satellite; if it is reflective or emits strongly, this might be a significant input.

3.2. Thermal Load cases

Based on the use case, the following section outlines the load cases used for further analysis, which serve as the basis for assessing the telescope model and investigating design. Design iterations are analyzed in terms of their impact on RBM performance metrics.

To investigate the thermo-mechanical behavior of the telescope structure, the initial model is subjected to five steady-state thermal load cases (LCs). These cases represent simplified but conservative conditions that may occur in the LEO environment; they conservatively bound the thermal gradients and temperature extremes the structure may experience.

By assuming steady-state conditions, the analysis ensures that the resulting temperature distributions are more severe—both in terms of gradient magnitude and maximum temperature—than those typically encountered during orbital transients. This conservative assumption thereby serves to identify worst-case scenarios for structural deformation and wavefront error performance.

The transient temperature experienced within the terminal is a thermal control problem influenced by all of its components. In general, most LEO systems are designed to remain within a specified temperature range. In most cases, a range of −30°C to +65°C covers the conditions under which optical and electrical systems operate successfully. Therefore, in a final design, the temperature is most likely to be controlled within these limits, which are thus used as bounds [52].

This simplification neglects the fact that the telescope itself is part of the thermal control problem. If it becomes too hot or too cold, it will complicate this aspect of the terminal design. Depending on whether the system struggles more on the cold or hot side, the telescope might be thermally isolated. Other solutions are possible, but all depend on the system-level design and thermal control philosophy. Hence, assuming a worst-case temperature for the LCT is deemed the most appropriate approach at this stage of the project.

The five thermal load cases adopted in this study are derived from a previous system-level concept trade-off investigation. Their reuse enables a direct, qualitative comparison between the structural performance predictions obtained in the model and the thermal modeling results from the trade-off study. An overview can be found in the figure below

The geometry, combined with the orbit, provides the information required to simulate the radiation input, which in turn leads to the radiation load and its effect on temperature. However, it is computationally inefficient and infeasible to analyze the complete lifetime of the LCT. Therefore, different strategies have been developed to distill worst-case scenarios for a given system. For example, [53] recently scrutinized the 1994 NASA guidelines for selecting environmental parameters in low Earth orbit [51], using real data.

Applying either method to the current application is possible, though with limitations. The aforementioned off-the-shelf objective is one such constraint. The range of orbits and satellite interactions of the LCT would be so extensive that this approach might reach its limits and not necessarily capture the true worst cases. At the very least, it would be difficult to argue convincingly that it does.

Thus the load cases are used as schematically shown in 3.3. They encompass worst-case hot, worst-case cold, and operational thermal gradients due to solar, planetary infrared (IR), and albedo radiation and the terminal maximum and minimum temperature ($-30\ °C\ and\ +65\ °C$). Figure 3.3 illustrates the schematic of the thermal loads applied in the various cases.

All of these cases are steady-state. Given a successful thermal control strategy, the resulting temperature fields can be expected to be at least as extreme—if not more so—than those that would occur in orbit,

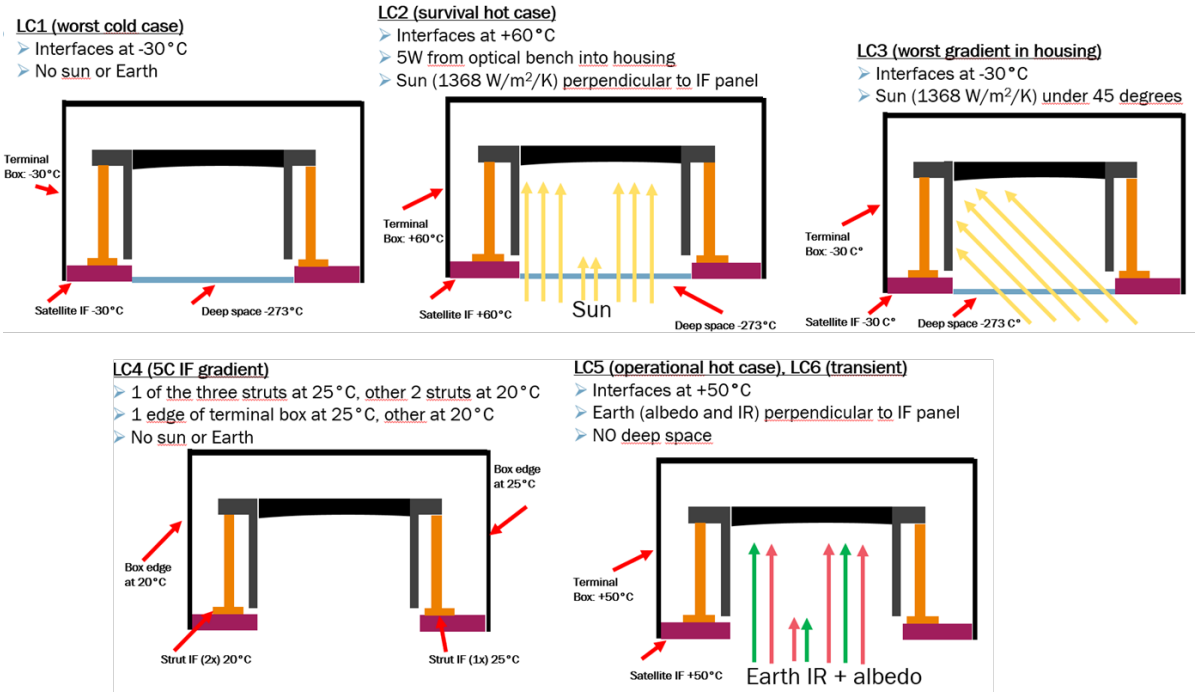

Figure 3.3: The load cases schematically shown starting with the survival situations (LC1 & LC2) and the operational load cases (LC3, LC4 & LC5)

particularly for the hot, cold, and gradient cases. The reason is that in orbit, temperatures oscillate due to eclipses, varying view factors, and fluctuating satellite temperatures.

Table 3.1: Qualitative overview of radiative input conditions and affected interfaces for each load case.

Load Case	Solar Radiation 1368 [W/m^2]	IR Radiation 237 [W/m^2]	Albedo Radiation [%]	Interfaces [° C]
1 Worst-case Cold	-	-	-	-30
2 Worst-case Hot	Yes 0° incedence	-	-	+60
3 Worst-case Gradient	Yes 45° incedence	-	-	-30
4 Conductive Gradient	-	-	-	20 / 25
5 Operational Hot	-	0° incedence	30% | 0 °incedence	50

The approach taken here is more conservative than either of the aforementioned ones and may lead to over-dimensioning or to temperature fields that are unrealistically extreme. However, given that both the application and the material are still under development, this is deemed a sound approach—at least for the preliminary evaluation.

3.2.1. Transient example

The varied orbits, satellite geometries, relative terminal locations, and link objectives all influence the thermal environment. Therefore, it is challenging to generalize a transient analysis to demonstrate performance for an off-the-shelf LCT. Nevertheless, a transient orbit case for an LCT still provides valuable insight into the problem, as well as reference data for the proposed load cases. To this end, a simplified model was built to assess the radiative loads. In this case, a relatively low LEO orbit (500 km) was chosen, and five orbits were simulated.

The model consists of a cube with roughly the same size as the LCT, exposed to varying albedo output over Earth's surface. Figure **??** illustrates the resulting average incoming radiation per wavelength band. Where the eclipses are clearly visible in the green solar band, in this case lasting around 30 minutes. Furthermore, the behavior of the graph is very close to periodical. No 5 orbits cover roughly 8 hours.

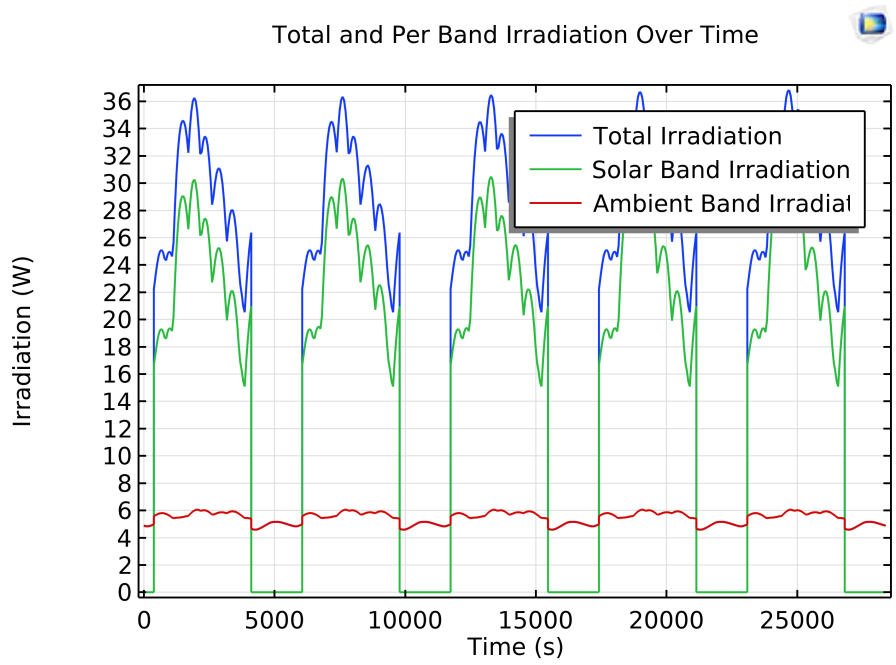

Figure 3.4: Received average radiation per wavelength band in W over 5 near-polar orbits at an altitude of 500 km.

3.3. Launch phase

The launch phase subjects satellite communication terminals to demanding mechanical loads. Pre-launch phases—such as transportation, ground handling, and integration involve lower intensity loads that are mitigated through protective packaging [54]. These are, minor compared to the environments encountered during ascent, where the nature and origin of the dominant loads are described in more detail below.

The velocity required to put a satellite into orbit is immense: >7 km/s. Hence, rocket launches produce extreme accelerations through their engines, which generate intense acoustic and vibrational energy. This energy transfers through the structure of the rocket and through the air in a vibrating manner. The 4 main types of mechanical loads a satellite experiences and their sources are reported in Table 3.2 by [29].

Table 3.2: Sources of launch vehicle environments by [29]

Origin	**Induced Load(s)**
Lift-off	Acoustics
Aerodynamics / Buffet	Acoustics
Separation (stage, fairing, spacecraft)	Shock
Motor burn / Combustion	Random Vibration, Sine Vibration

As noted before, the versatility of the application results in the possible use of different launchers. All of the mechanical launch loads are dependent on the type of launcher used. Because most use different types of engines, they do not have the same shape, flight profile, mass or payload interface. Therefore, the loads experienced by the satellite and, in turn, the terminal can differ significantly. An example of this fact is reported in Table 3.3 for the maximum steady-state acceleration.

Table 3.3: Reports the longitudinal and lateral maximum quasi-static launch loads. * Depend on mass of spacecraft by [30].

Launch Vehicle	Longitudenal [g]	Lateral [g]	Vehicle origin
Ariane 4	4.5	0.2	Europe
Ariane 5	5.5	0.4	
Atlas	5.5	0.4	USA
Delta	5.5 – 7.1*	0	
Pegasus	7 – 10	0	
Proton	4	0	Russia
Long March 2E	5.2	0.6	China
Long March 3	5.5	0.6	

Maximum steady-state acceleration is the highest constant acceleration experienced by a rocket, which increases during launch as the vehicle's mass decreases while thrust remains unchanged. This acceleration is primarily in the launch direction and maximum at the end of the launch.

This is however not the complete picture because any vibrating structure can be subject to resonance. Which increases the load experienced by the system do to unstable oscillation of interfaces or the assembly itself. There are multiple avenues to mitigate this risk, namely, the mass acceleration curve (MAC) a minimum first eigen-frequency requirement and or random vibration analysis. Commonly most or all of these are applied within the design process.

The Mass Acceleration Curve (MAC)

The MAC defines quasi-static design limit loads derived from the low-frequency dynamic response during launch. It is commonly used when the launch vehicle is not yet known, providing an envelope of expected mechanical loads across a wide range of masses and structural stiffnesses. Each component or assembly is evaluated based on its mass and the first fundamental frequency, particularly if it or its mounting structure is below 80 Hz. The MAC ensures conservative load estimates for preliminary sizing and structural margin assessments. A representative curve and tabulated load values are provided in [31]. For the LCT telescope the complete mass will not exceed 5 kg and as mentioned by Koca et. al. linear inter- or extrapolation may be used between the break points.

Table 3.4: MAC Design Limit Loads for components up to 10 kg [31]

Mass (kg)	Limit Load (g)
1	68.0
5	49.0
10	39.8

Random Vibration

Random vibration analysis models the high-frequency excitation experienced during launch, primarily caused by acoustic pressure and engine-induced vibrations transmitted through the structure. It is used to determine stress and displacement responses in components—especially those with lower damping or complex geometries. This analysis is essential for capturing the distributed loading across the payload and is typically performed once specific launcher acoustic profiles or interface environments become available. For components over 20 kg or with modes below 80 Hz, MAC-based analysis may take precedence instead.

4

C/C-SiC Materials and Manufacturing for near zero CTE aplications

Designing and modeling C/C-SiC parts requires a detailed understanding of the available processes. The aim of this chapter is to motivate the model geometry and describe the parameters available when designing a C/C-SiC part, as well as how they affect the material properties. These parameters form the basis of the model study and are the drivers behind the behavior of the telescope in the load cases introduced in the previous chapter.

The solutions to overcome engineering challenges largely depend on the manufacturing process. This is true for any engineering project, but especially so for composite materials—and even more so for ceramic matrix composites (CMCs). Hence, it is necessary to understand the steps involved in producing this material and using it to construct parts. Accordingly, the different strategies for synthesizing C/C-SiC and the process steps involved are reviewed in this chapter. The following guiding question is addressed in the coming sections:

How does melt-infiltration manufacturing of C/C–SiC work, and what are its implications for defining a preliminary LCT telescope geometry and the material property range to be considered?

This question is implicitly answered in three sections:

- First, the manufacturing processes by which C/C-SiC parts are made are explained, including a deeper dive into the LSI method used for cost-effective production.
- Second, the model geometry of the on-axis Cassegrain concept is reported, constrained and informed by the manufacturing process.

Furthermore, some materials commonly used in optical space systems are bound to be encountered and required to construct a complete LCT or alternative optical system. Examples include aluminum, titanium, and structural adhesives (such as EC2216). Since they are used in the design, they also influence the model's performance.

C/C-SiC is a subclass of ceramic matrix composites, which themselves represent a niche subgroup of composite materials. The following section assumes that the reader has some basic knowledge of composites—for example, fiber types, the relation between matrix and fiber materials, and the difference between short- and long-fiber composites. Examples of composites used in (optical) space applications are reported in Appendix A.

As with all composites, fiber orientation, dimensionality of the preform, and thermal treatment conditions are important parameters in manufacturing, as they strongly influence the performance of the final CMC part or product. Various types of CMCs exist, most of which are used to make load-bearing structures for high-temperature applications. An overview of the general manufacturing processes for C/C-SiC materials is shown in Figure 4.2 [12].

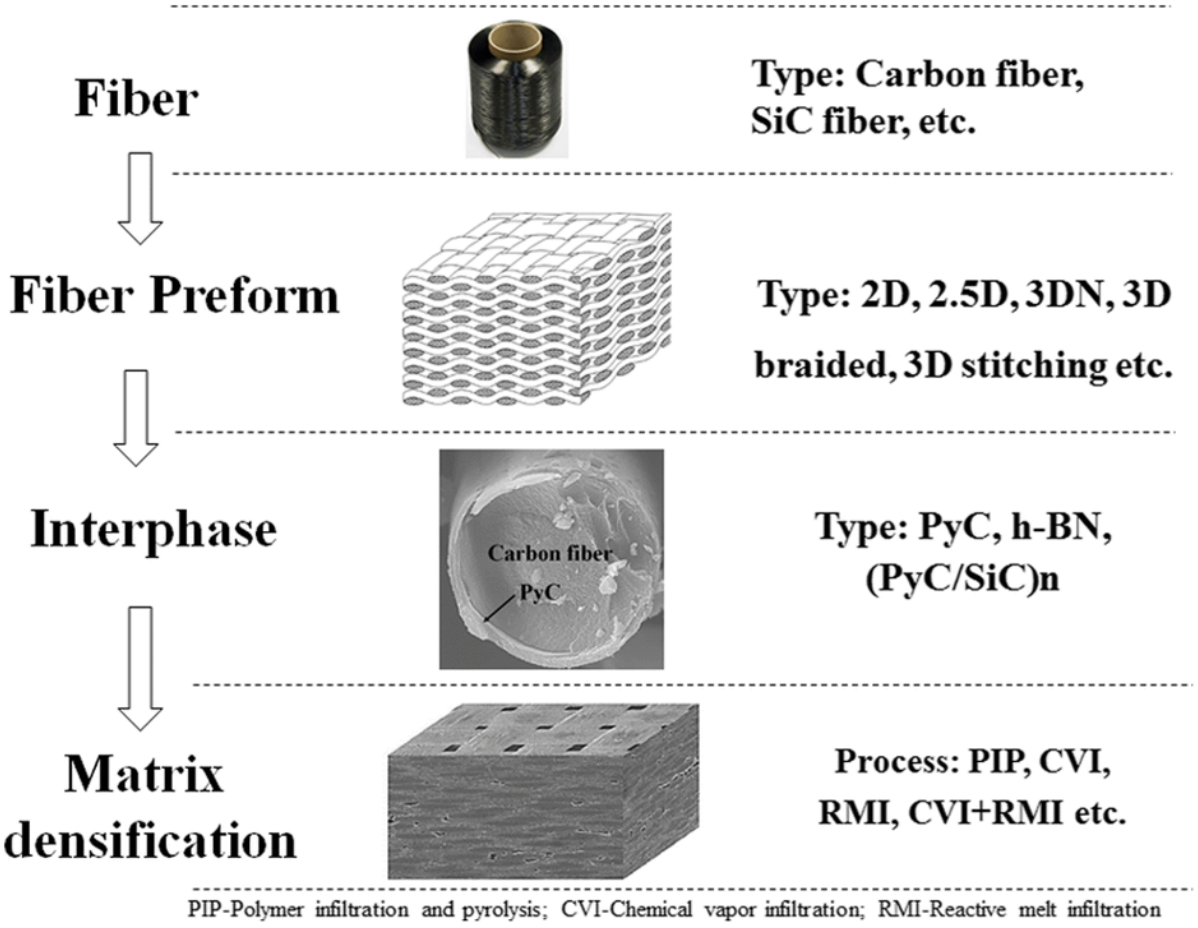

Figure 4.1: The general processing steps involved in the synthesis of different versions of C/C-SiC materials [2].

Carbon–carbon silicon carbide (C/C-SiC) is a specific type of CMC and, more precisely, a specific form of carbon–silicon carbide-based CMCs. C/C-SiC specifically refers to carbon–carbon parts that have been siliconized through liquid silicon infiltration (LSI). The key aspects of this description are the words “liquid” and “infiltration.”

There are different methods by which a carbon–carbon part can be infiltrated, the main difference being the phase of the silicon carrier. Simply put, the three options are gas, liquid, and solid*. Figure 4.2 provides an overview of the different infiltration mechanisms and how they differ, while Figure 4.1 outlines the steps involved in synthesizing C/C-SiC and its counterparts. These processes are reviewed in greater detail in the following section.

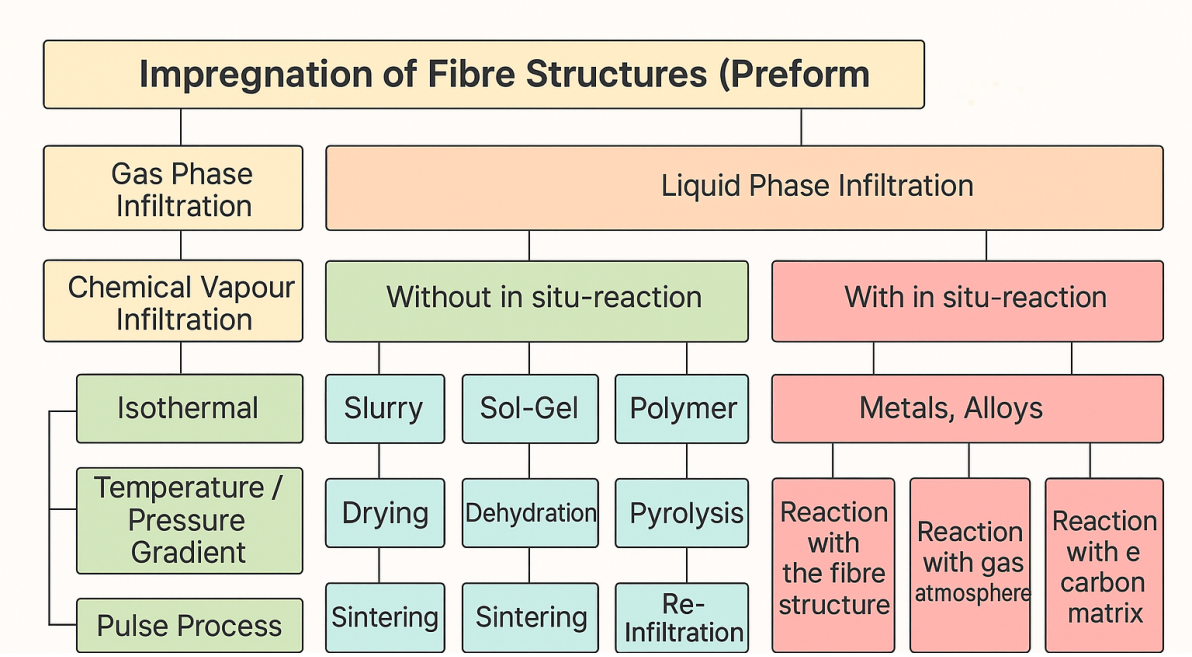

Figure 4.2: General overview of the manufacturing processes for CMC materials, adapted from Figure 9 in [12].

*The "solid" classification refers to the slurry-based polymer (re)infiltration process, in which carbon is added to a liquid polymer to form a slurry. This slurry is then infiltrated into the porous C/C preform in a manner similar to resin infiltration in conventional composite manufacturing.

4.1. Manufacturing by C/C-SiC by melt infiltration of Carbon-Carbon parts

The design process is also aided by understanding the manufacturing process. Therefore, the manufacturing process itself and the relations to the properties of interest, e.g., the coefficient of thermal expansion (CTE) are documented in this subsection.

The LSI process has 3 main steps shown schematically in Figure 4.3 [12]. In between these steps different kinds of composite materials are synthesized. First a Carbon fiber reinforced composite(CFRP) is cured. After which, through pyrolysis a carbon carbon fiber composite (C/C) part is formed. Finally through capillary infiltration of liquid Si into the C/C part the C/C-SiC is formed. These steps are the outline of this section

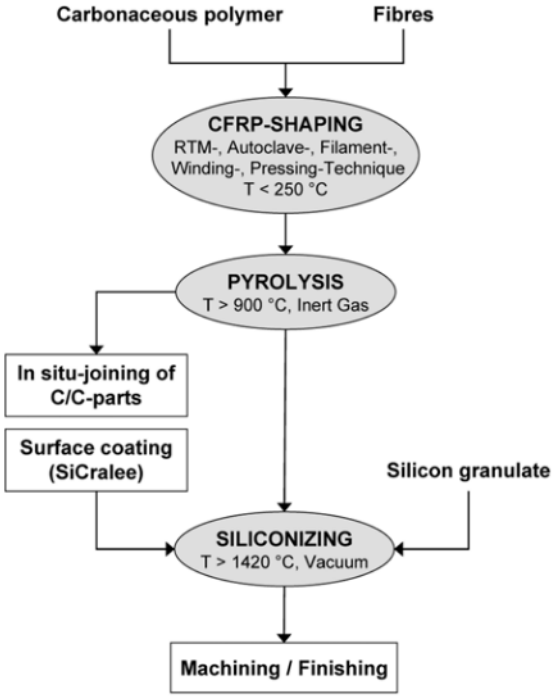

Figure 4.3: Schematic of the liquid silicon infiltration process (LSI) [12]

4.1.1. The carbon fibre reinforced polymer step

The first step in the LSI process involves the manufacturing of a carbon fiber reinforced polyme composite, which acts as the precursor for the carbon-carbon material. This step starts with the selection and arrangement of carbon fibers—typically PAN- or pitch-based—whose orientation and type strongly influence the mechanical behavior of the final C/C-SiC composite. The fibers provide the primary load-bearing capacity throughout all stages of the composite's evolution.

The matrix used at this stage is typically a thermosetting resin, most commonly phenolic due to its relatively high carbon yield (up to 74%) and ease of processing. A high carbon yield is crucial for minimizing shrinkage during pyrolysis and achieving sufficient densification in the resulting C/C material without excessive reimpregnation cycles. Moreover, a high carbon content in the matrix helps shield the fibers from chemical attack during the subsequent silicon infiltration step, preserving their mechanical integrity.

Phenolic resins are selected in this process not for their mechanical performance in cured CFRP parts, but for their high carbon yield during pyrolysis, which makes them particularly suitable for producing carbon matrices in carbon/carbon and carbon/silicon carbide composites. While not as widely used as epoxies in conventional CFRP manufacturing partly due to their toxic emissions during curing and handling complexity phenolics remain the preferred choice when carbonization efficiency and thermal stability take precedence over mechanical performance of the polymer phase.

In RTM, for example, the resin is injected into a mold containing a dry fiber preform and cured under heat and pressure. Autoclave curing uses vacuum bagging to ensure resin distribution and minimize porosity. Hot pressing compresses resin-impregnated fiber layups at moderate temperatures, while filament winding wraps resin-coated fibers around a mandrel before curing. The chosen method must ensure minimal defects, as flaws in the CFRP preform can propagate through subsequent processing stages, degrading the final composite.

To summarize, the CFRP step requires careful optimization of both fiber architecture and resin system. The phenolic resin must be thoroughly infiltrated and uniformly cured to form a defect-free green body. After curing, the composite undergoes pyrolysis at approximately 900°C in an inert atmosphere, converting the polymer matrix into a carbon matrix and forming the intermediate carbon-carbon (C/C) composite, which is ready for further densification and silicon infiltration. [12] [37]

4.1.2. Pyrolysis forming the carbon-carbon part

The pyrolysis step transforms the cured CFRP into a carbon/carbon (C/C) structure. This conversion is carried out in an inert atmosphere, typically under nitrogen or vacuum, and requires heating to temperatures around 900°C. During this process, the phenolic resin matrix decomposes, releasing volatile gases and leaving behind an amorphous carbon residue that forms the carbon matrix.

A key challenge in this step is the significant volume shrinkage of the polymer matrix. Phenolic resins, which are often used due to their relatively high char yield, still experience substantial shrinkage—up to 50% of their volume—during carbonization. The presence of carbon fibers reduces the overall shrinkage at the macroscopic level, particularly along the fiber axis where contraction is close to zero. However, transverse shrinkage remains substantial and can introduce internal stresses, especially in geometries such as cylinders, an example is found Figure 4.4.

Figure 4.4: Delaminations in tubular C/C preforms (Ø 51/40 mm, DLR) were caused by circumferential fiber orientation and constrained contraction during pyrolysis. [5]

Such anisotropic shrinkage was observed during this project to result in delamination in cylindrical parts. While redensification cycles (such as additional resin infiltration) can reduce porosity and reinforce the matrix, they are generally avoided in C/C-SiC production using LSI, due to cost constraints and because the porous structure facilitates later silicon infiltration.

As the polymer matrix degrades and volatile compounds escape, internal voids and pores are formed. Without proper support, this shrinkage and outgassing can cause warping, fiber wrinkling, or cracks. Therefore, the green body must be mechanically supported by a mold or die during pyrolysis to prevent distortion. This is especially critical for thin-walled or curved components, where fiber buckling or separation between layers may otherwise occur.

Even with mold support, the matrix–fiber interface is subjected to differential stresses, which can result in microcracking or debonding. Debonding or delamination is a detriment to the performance of the part and should be avoided. However, counterintuitively, microcracks are a necessary part of the process: they provide the channels for the capillary effect during the siliconization step.

Because LSI processing favors simplicity and cost-effectiveness, achieving a defect-minimized C/C part in a single pyrolysis step is paramount. This places increased emphasis on selecting resins with optimal carbon yield and shrinkage characteristics. Thus maintaining uniform fiber volume percentage and enabling the forming of the carbon around the fiber bundles in one step.

4.1.3. In situ joining of C/C preforms prior to siliconization

For complex structural components, individual C/C segments can be joined prior to the liquid silicon infiltration (LSI) step, enabling the fabrication of monolithic, integrated C/C-SiC structures with high dimensional stability and mechanical continuity. This process, schematically indicated in Figure 4.3, is referred to as *in situ joining*, since the bonding interface is co-converted into a SiC-rich region during the siliconization cycle.

To realize such joints, the C/C subcomponents are first machined with sufficient surface precision and topology to ensure contact in the joining regions. A carbon-rich joining paste typically based on phenolic resin and fine carbon powders is then applied to the prepared interfaces. Following application, the assembly is subjected to a curing cycle analogous to the initial CFRP preform, resulting in a bonded assembly. During subsequent LSI, the paste undergoes carbonization and reacts with infiltrated silicon during the heating cycle. The heating cycle ramps to 1450 °C, the temperature required to melt Si. At around 900 °C, pyrolysis of the binder occurs. Therefore, the carbon slurry is pyrolyzed before the Si melts and infiltrates. Yielding a SiC bond line that is chemically and structurally integrated with the base material.

This method eliminates the need for a separate pyrolysis step after bonding, as the molten silicon operates at temperatures significantly exceeding typical pyrolysis thresholds (e.g., $T_{Si} > 1410°C$), allowing simultaneous infiltration and reaction at the joint interfaces. Experimental characterization has shown that the resulting SiC interfaces exhibit homogeneous morphology and comparable mechanical performance to the monolithic C/C-SiC material [5, 55, 56].

Nevertheless, the placement and quantity of applied silicon or silicon powder around joint interfaces are critical to ensure complete infiltration and reaction, and these parameters are often based on proprietary process know-how. While some qualitative guidelines are published [55], precise volumetric control remains part of industrial heritage knowledge. Additional implications for surface preparation and machining tolerances of the preforms are discussed in Section 4.1.5.

4.1.4. Silicon infiltration

LSI is also known as reactive melt infiltration, because the silicon melts and subsequently reacts with the carbon (fibers) to form Silicon carbide (SiC). The final stage in the production of C/C-SiC composites via the LSI route is the siliconization of the porous carbon-carbon preform. This process is governed by capillary infiltration of molten silicon into the preform's open porosity, followed by an in-situ reaction with carbon to form silicon carbide. The LSI step is typically performed under vacuum or low-pressure inert atmosphere at temperatures exceeding the melting point of silicon ($T_{\mathrm{melt,Si}} = 1414°\mathrm{C}$), often reaching 1650°C or higher to promote infiltration kinetics and complete reaction across the microstructure [5].

Silicon is introduced in the form of granules, which melt and infiltrate the C/C component driven solely by capillary forces. The infiltration is relatively fast (on the order of minutes), given the low viscosity of molten silicon and its excellent wettability with carbonaceous surfaces (contact angle $\theta < 22°$). Analytical and experimental models indicate that infiltration depths up to a maximum of 500 mm can be achieved within several minutes, depending on the pore structure and temperature profile [5,57].

The warming phase, raising the furnace and components to infiltration temperature, typically requires up to 24 hours and constitutes a major cost driver in the LSI process due to high thermal inertia and strict temperature uniformity requirements. During the dwell period, molten silicon percolates into the interconnected pore network of the preform and reacts exothermically with the solid carbon ($\Delta H = -68\,\mathrm{kJ/mol}$), forming a dense SiC matrix phase. The infiltration proceeds until most of the accessible porosity is filled, although some residual, unreacted silicon remains due to excess Si supply required.

The resulting CMC microstructure is a tri phase system consisting of:

- Unconverted carbon fiber (tows) embedded within the partially converted to SiC, carbon matrix
- SiC formed in-situ by chemical reaction between the Si melt and the carbon matrix.
- Residual (free) silicon occupying large pores and interstitial regions.

This microstructural composition defines the material as C/C-SiC. The mechanical and thermal properties are strongly influenced by the relative volume fractions and morphology of each phase, particularly the residual silicon, which can be minimized via careful control of precursor porosity and carbon yield [5].

In the case of in-situ joined assemblies, the joint interface, typically comprising a cured carbon-rich paste, is simultaneously pyrolyzed and infiltrated during this step. As the silicon infiltrates both the base C/C structure and the joint seam, it reacts with the carbon at the interface, forming a continuous SiC layer that chemically bonds the two subcomponents. This enables robust mechanical integration of complex or modular geometries without requiring post-processing or intermediate joining steps. An example is shown in Figure 4.5, where the machined joining areas and the resulting homogeneous morphology across the SiC bond line are clearly visible [5,55].

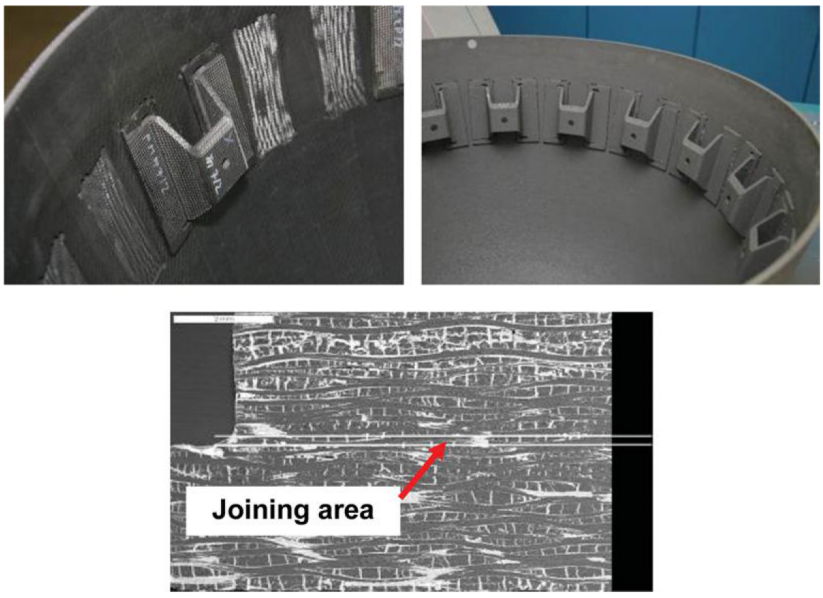

Figure 4.5: In-situ joining of a structural C/C-SiC component, showing a C/C profile with an Ω-shaped cross section bonded to a machined area on the nose cap using a carbon-rich joining paste. The structure is joined during the LSI step, resulting in a continuous SiC matrix across the interface. The lower image shows an SEM micrograph of the joint, indicating homogeneous morphology of both the substrate and the bonding region, figure from [5].

4.1.5. Machining CMC

By nature, SiC-based ceramic matrix composites are hard and brittle relative to metals, orthotropic, and heterogeneous. This makes machining them non-trivial. Conventional approaches suggest using the near-net-shaping process to avoid machining

where possible. However, this approach does not always provide a solution. Given the common μm tolerance requirement in satellite and FSOC applications, machining of the material needs to be considered.

The material-removal mechanisms, several processes, and the effect of material properties and tool parameters were discussed extensively in [**?**]. They concluded that the weak fibre matrix interface, while beneficial to toughness, causes interface defects during machining. In addition, ultrasonic- and laser-assisted machining were investigated and shown to have significant potential by increasing efficiency and reducing tool wear and surface roughness.

A common method for finishing near-net-shape parts employed in industry is grinding. A comprehensive overview of the status of understanding and solutions for mitigating grinding damage in CMCs is provided by [**?**], which also provides insight into the machining challenges encountered in CMCs and C/C-SiC.

[58] established some good practices for selecting/designing tool types specifically in C/C-SiC drill hole and slot machining. Along with investigating free-form surface machining. They concluded on using a diamond abrasive and a bronze expedient with an electroplated layer for drill hole machining and slot machining, respectively.

Resulting CASTT preliminary test object
To validate the manufacturing approach and assess in-situ joining, a preliminary version of a telescope tube in the CASTT project was fabricated and processed via a single LSI cycle. The part featured a preimpregnated wound outer shell with three arms, joined to a central hub using the phenolic carbon-rich paste using the in-situ joining method. The resulting C/C-SiC structure demonstrated successful integration using SiC joints.

As seen in Figure 4.6, the outer geometry was largely preserved, though surface irregularities appeared. Delaminations and wrinkling were observed, likely stemming from the known shrinking induced internal stress combined with the inherently constrained cylindrical geometry during pyrolization. Despite these defects, the demonstrator supports the viability of the in-situ joining concept.

This first iteration provides a proof-of-concept for a structurally integrated C/C-SiC telescope tube. Future refinements will focus on defect mitigation and improved preform stability to meet optical system requirements.

Figure 4.6: Photographs of the first iteration siliconized C/C-SiC test structure featuring integrated in-situ joints. **Left:** Full view of the cylindrical component, showing the outer surface finish with visible fiber architecture. **Right:** Zoomed-in top view of the joint regions, showing the machined interfaces and bonded sub-components.

The aim now is to guarantee reproducible manufacturing, and the first tests have been completed with a new layup.

4.1.6. Alternative C/C-SiC manufacturing techniques

The distinctiveness of the processing techniques used to make C/C-SiC components derives from the infiltration method. The SiC is either supplied through gas carrying SiC, liquid Si or a liquid polymer carrying SiC. The chosen approach effects a.o. the interphase/FMB and the porosity and thus the final properties of the component.

Chemical Vapor Infiltration
An alternative method to form the SiC matrix in C/C-SiC components is through Chemical Vapor Infiltration (CVI), wherein a porous C/C preform is infiltrated with a gaseous silicon carbide-containing precursor. A key advantage of CVI lies in its compatibility with near-net-shape, complex geometries, and its ability to uniformly deposit high-purity, fine-grained SiC. The rate of matrix growth is governed by both the chemical reaction kinetics and the transport of the reaction products into the porous network. The structure of the open pore system within the preform, typically 10–500 μm in diameter, affects the homogeneity and depth of infiltration.

A commonly used precursor for SiC deposition is methyltrichlorosilane (MTS), which reacts with hydrogen according to:

$$CH_3SiCl_3 + H_2 \rightarrow SiC + 3HCl$$

Hydrogen acts as the carrier and reducing gas, facilitating the decomposition of MTS and the deposition of SiC on the fiber surfaces.

Compared to the LSI process, CVI-derived materials exhibit superior thermo-mechanical and fracture toughness properties, largely due to the high purity of the SiC matrix and the absence of free silicon. Another significant advantage is the precise control over the fiber/matrix interphase, typically realized by applying a thin PyC coating (0.1–0.3 μm) via CVI prior to SiC deposition. This weak interphase enables the crack deflection and damage tolerance.

However, a main drawback of the CVI process is its inherently slow deposition rate, resulting in prolonged processing times. For instance, the densification of a C/C preform with 5 mm wall thickness may require 40–60 hours, yet still result in a residual porosity of approximately 12%—a value roughly three times higher than that typically achieved via a well-controlled LSI route. The trade-off between deposition rate and infiltration depth is particularly pronounced: higher temperatures and pressures accelerate surface deposition but hinder pore penetration, often sealing the surface before the core is fully densified. As such, isothermal-isobaric CVI (I-CVI) and thermal/pressure gradient CVI (G-CVI) are employed depending on component geometry and desired material homogeneity.

Despite its limitations, CVI remains a preferred technique for producing components with stringent thermo-structural requirements, especially in aerospace and high-temperature applications. [5].

Liquid Polymer Infiltration Polymer Infiltration and Pyrolysis
The infiltration can also be completed using liquid preceramic polymer which is silicon and carbon within its polymer molecule. Which is called allylhydridopolycarbosilane and characterized by an alternating chain of C and Si atoms. The polymer is pyrolyzed in a subsequent step where the SiC is already deposited at a relatively low temperature 850 - 1050 °C. Therefore the process is also known as polymer infiltration and pyrolysis (PIP).

LPI is regarded as the most advanced manufacturing method for large and complex-shaped CMC parts. The main drawback is that infiltration and pyrolysis steps have to be repeated 5–7 times for a porosity of less than 10%. In addition to the high cost of the carbosilane polymers, which range up to 1800 $ /kg. [5]

Most of the information provided in this section was obtained from Walter Krenkel's chapter on C/SiC and C/C-SiC composites. In this chapter, a summary of the advantages and disadvantages of the different process parameters can be found as well. [5, 12]

4.2. C/C-SiC LCT telescope geometry and model

The design information required for the model is gathered by using three sources. Namely, the Cassegrain design analyzed within TNO, the information gathered through the literature research and CASTT project, and some information from current developments of the RS80 project.

Detailed optical analysis is left out of scope, but with some primary assumptions and basic geometric optics the geometry required for the model can be deduced. Given the optics, i.e., the M1 and M2 drive the structural support, they are used as a starting point. From the prior research of the focal Cassegrain introduced in **??**, the optics are scaled to RS80 diameter.

This telescope and its sensitivities, reported in Table 2.6, are in theory insensitive to the size of the design as long as they are scaled equally in 3 dimensions. This is achieved by keeping the ratio of the diameter and distance between the M1 and M2 constant:

$$L_{\text{new}} = L_{\text{ref}} \times \frac{D_{\text{new}}}{D_{\text{ref}}} = 144.34 \times \frac{105}{200} = 75.75$$

where $L_{\text{ref}} = 144.34\,\text{mm}$ is the reference distance between M1 and M2, $D_{\text{ref}} = 200\,\text{mm}$ is the original primary mirror diameter, and $D_{\text{new}} = 105\,\text{mm}$ is the scaled diameter. The resulting distance $L_{\text{new}} \approx 75.75\,\text{mm}$ preserves the original design ratio.

For the Cassegrain telescope, the design has an inherent trade-off between volume and sensitivity. The closer the mirrors are placed to each other, the more sensitive they are to disturbances, e.g., thermo-elastic deformation. But decreasing the distance means less volume and thus mass, decreasing the cost. Their sensitivity is increased due to the need for smaller mirror radii, which means that the reflection angles of the light are larger, leading to a dislocation having a larger effect on the WFE.

The distance is rounded and set to 75 mm, and treated as a variable input in the model to allow for future adjustment. The variables in 4.1 that are not functions can be changed within reasonable limits to change the geometry and investigate the effect on the results.

The preliminary telescope design geometry is built up from the mirror dimensions parametrically within COMSOL. Meaning the key geometric values are defined as functions of a small number of inputs. One such input is the distance between the primary

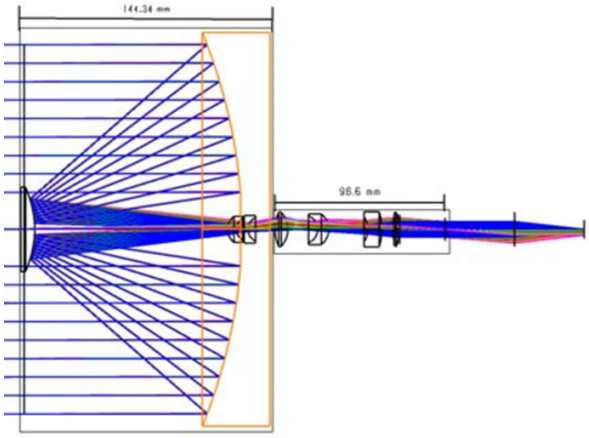

Figure 4.7: The ZEMAX model of the 200 mm focal Cassegrain design from previous research within TNO.

mirror (M1) and secondary mirror (M2). Although it is set for the RS80 design, using it as an input enables scaling to the test object in subsequent activities.

Considering the current manufacturing in the CASTT project, the choice is made to keep the structural design as simple as possible, thus very similar to the CASTT design for the telescope. There are two additional reasons for this geometry: Arceon has shown that it is capable of synthesizing an assembly of C/C-SiC parts to such a shape, which is not trivial as was reported in Chapter 2. Finally, the model can be easily scaled due to the parametric setup, allowing for a pathway to analyses for possible testing activities within the CASTT project. A schematic is shown in 4.8.

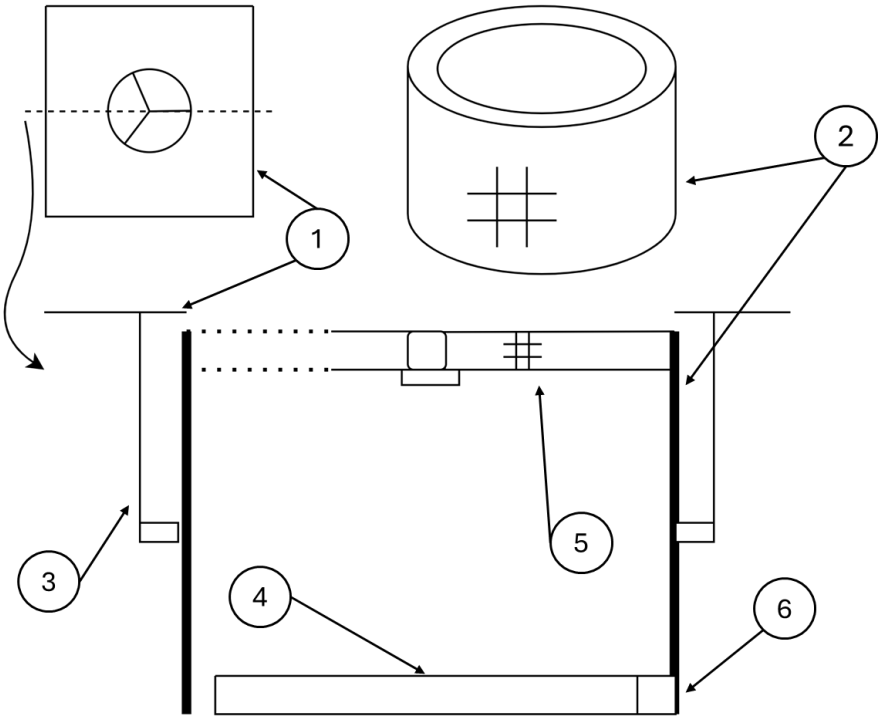

Figure 4.8: Schematic of the parts of the preliminary model including the fiber orientation of C/C-SiC where relevant. 1, RSA 6065-T6 Nacelle ; 2, C/C-SiC 0/90 cylinder ; 3, Timet-550 Flexures ; 4, Fused Silica M1 ; 5, C/C-SiC 0/90 plate ; C/C-SiC short fiber connection plate.

The complete set of geometric parameters used for the preliminary design is listed in Table 4.1. Each value is derived in a similar parametric fashion and defines key dimensions of the cylinder, spider arms, mirrors, and support features.

Table 4.1: Geometric parameters for the preliminary telescope design

Parameter	Value (mm)	Value (m)	Description
d_{M1_M2}	75	0.075	Distance between mirror surfaces
h_c	$d_{M1\_M2} + w_s + t_{m1} = 86$	0.086	Height cylinder
r_c	$r_{m1} + t_{a2} + t_c = 53.2$	0.0532	Radius cylinder
t_c	3	0.003	Thickness cylinder
l_s	$r_c \times 1.1 = 58.52$	0.05852	Length spider arm
w_s	6	0.006	Width spider arm
t_s	1	0.001	Thickness spider arm
r_{m1}	50	0.05	M1 radius
r_{m2}	5	0.005	M2 radius
t_{m1}	$\text{round}(r_{m1} \times 2/20, 3) = 5$	0.005	M1 thickness (D/20)
th_{m2}	$15° = 0.2618$	0.2618	Half angle glue spot M2
w_t	$r_c \times 6 = 319.2$	0.3192	Terminal dimensions
h_t	$h_c + 100 = 186$	0.186	Terminal height
d_t	$r_c \times 4 = 212.8$	0.2128	Terminal diameter
t_t	1	0.001	Terminal thickness
w_f	20	0.02	Flexure width
t_f	1	0.001	Flexure thickness
h_f	$h_c \times \frac{2}{3} = 57.33$	0.05733	Flexure height

While the geometry is defined parametrically for flexibility, this approach has its limits. The automatic generation fails when the spider arm length becomes shorter than the M1 diameter. Such conditions result in non-physical or overlapping geometry and must be manually guarded against when adjusting input parameters.

4.2.1. C/C-SiC material model in heat transfer and solid mechanics

The manner by which the material is implemented is reported. The material properties are imposed within the solid mechanics module using local axis systems to orient the CTE and stiffness for the C/C-SiC. As shown in Figure 4.8 for one of the spider arms. For the cylinder, a cylindrical system is used, the fiber orientation is shown in Figure 4.8 as well.

As mentioned before, the material properties of C/C-SiC are tunable. The designer and supplier aim to reach a certain set of values. However, in most cases ARCEON limits the choices, preferably by using woven sheets of high-tenacity fibers. However, the main interest in this thesis is the thermo-mechanical performance of the telescope. Hence, the starting point for varying the material properties will be the CTE and conductivity.

The in-plane and out-of-plane properties required are the conductivity, coefficient of thermal expansion and E modulus or stiffness. Given the dependence on the process, the exact values are not 100% certain, even for the supplier themselves. However, an estimation can be made based on the available literature, the experience of the supplier, and the experience within TNO.

The CTE and conductivity expected with the 0°/90° or ±45° can be estimated from literature. They vary with SiC percentage, fiber type and layup. Here, one of the primary questions within the design of the LCT telescope would be what exact properties should be aimed for during the process. Hence, this range of values is investigated in the coming sections. The specific values applied within the model are a linear distribution between the extremes reported in [5] and shown in Table 4.2.

The SiC percentage is controllable based on process parameters like siliconization time. Hence, the effect of this property is the point at which the variation of parameters can be started.

Table 4.2: Material cases with anisotropic thermal properties for C/C-SiC: In directions parallel (∥) and perpendicular (⊥) to the fiber orientation. The first set is based on high SiC % (35–40 vol%) decreasing with each. *Note values are rounded.

Material cases	**CTE [μm/mK]**		**k [W/mK]**	
Parallel Perpendicular	∥	⊥	∥	⊥
1	1,1	4,0	33,6	18,1
2	0,6	3,5	29,5	15,8
3	0,1	3,1	25,3	13,6
4	-0,5	2,6	21,2	11,3
5	-1,0	2,1	17,0	9,0
Step size	0,525	0,475	4,15	2,275

The Young's modulus in the same source is reported to decrease with SiC vol.% as well from 100 GPa to 60 GPa. Given the

orthotropic / quasi-isotropic nature of C/C-SiC, a Young's modulus on its own does not fully represent the stiffness of the material accurately. However, there has been research completed and reported in literature that characterizes the stiffness of a C/C-SiC twill woven high-tenacity fiber in [33], from which the stiffnesses can be implemented in the model in all directions. Taking a conservative approach, these are rounded down to the values found in 4.3.

Table 4.3: Orthotropic material constants *Carbeon* for material model

E_X **[GPa]**	E_Y **[GPa]**	E_Z **[GPa]**	ν_{xy} **[-]**	ν_{yz} **[-]**	ν_{zx} **[-]**	G_{xy} **[GPa]**	G_{yz} **[GPa]**	G_{zx} **[GPa]**
70	70	20	0.3	0.3	0.3	20	5	20

5

Method: Thermo-Elastic Modelling

The space environment has several facets that affect the deformation and position of the telescope mirrors. For example, the aforementioned temperature gradients, i.e., one hot side expanding the telescope out of shape. Calculating that shape change and its effects is achieved through finite element analysis and reported in this chapter. Specifically, using the COMSOL multiphysics software, chosen at the start for their orbit mechanics module. The guiding question for this chapter is thus:

How is the LCT telescope modeled in COMSOL Multiphysics, and how is this modeling linked to the requirements?

Modelling the deformation behavior during a satellite orbit involves several disciplines of physics, i.e., orbit mechanics; radiative and conductive heat transfer; and solid mechanics through thermal expansion. As each is connected to the others, an interconnected model is required; a simplified schematic is shown in Figure˜**??**fig:3models.

For example, starting with the radiative heat-transfer model, the orbit of the satellite determines the incident angle of UV radiation, which in turn dictates the heat load received by the LCT surfaces. This time-varying radiative input influences the temperature distribution across the structure. The temperature of the LCT and telescope affects the infrared radiation that their parts re-emit, which is represented by the feedback arrow. The temperature also results, due to the material's tendency to expand, in relative motion or deformation of the mirrors, thereby degrading the optical performance by increasing the WFE, which determines whether the modelled design is valid. If the total WFE is above the aforementioned $\sim 50nm\ RMS$, $the design needs to be updated and reassessed$.

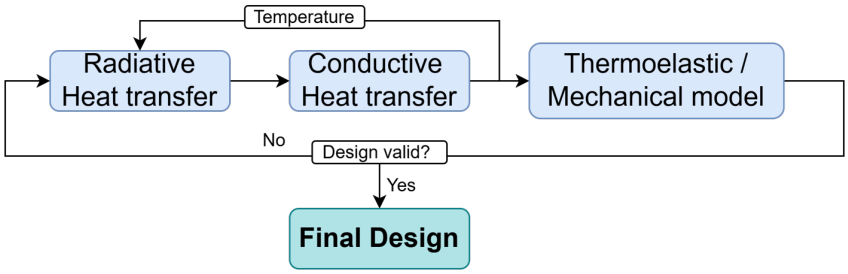

Figure 5.1: The fundamental models required in the thermo-elastic analysis of the LCT.

The example and figure above are simplifications to highlight the most basic formulation of the activities involved in modelling the LCT telescope. The complete workflow is reported in the next section; an extensive schematic can be found in Figure˜**??**fig modeltree. The method and steps involved are based on the paper by Badás etāl. (2023) **[?]** and are extended and altered where necessary—for example, orthotropic material models for C/C-SiC are implemented. They also extensively report the thermo-mechanical phenomena that affect the other parts of the LCT.

5.1. The modelling framework

While the individual steps are discussed in detail in the coming sections, an overview is first provided, shown schematically in Figure 5.2, to place them in context. The method's final product is ideally a compliant design, shown in turquoise on the bottom left—compliant w.r.t. the requirements, which are reiterated below in Table 2.7. The first step is making a preliminary design, which is reported in Section 4.2, or, in case of non-compliance, an indication of how far the design is from being compliant.

The next steps are the models needed to calculate the temperatures and deformations. These are shown in light blue and need to be built; this is achieved using the FEA tool COMSOL Multiphysics, chosen because of its availability, its capability to model all the phenomena involved within one software package, and its integrated orbit-modelling capability.

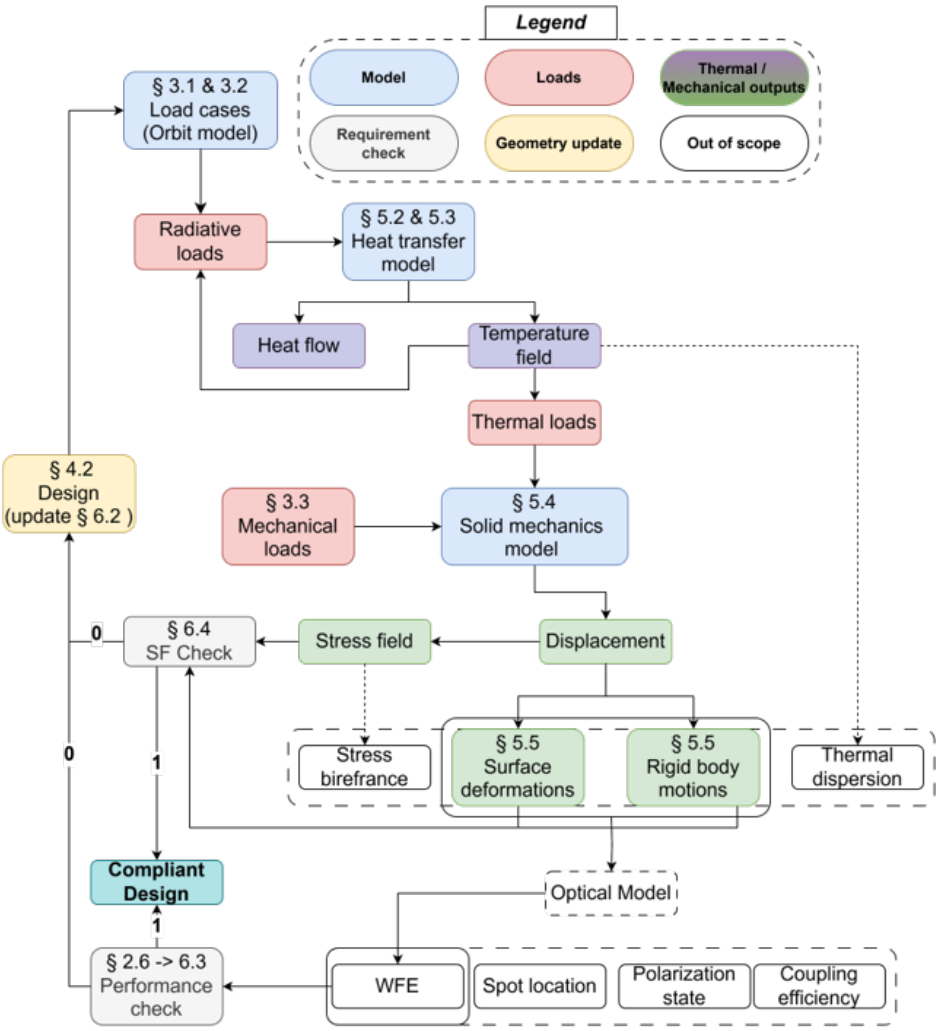

Figure 5.2: Complete overview of the modelling tree summarizing inputs and outputs, starting with the load cases and moving through heat transfer, solid mechanics, and optical regimes, where the feedback loop through the design update represents the iterative nature of design activities.

Although each modelling step focuses on different physical phenomena, they share a common structure and are typically implemented using finite-element methods. Each model in the workflow relies on the following components:

- Inputs—shown in red—e.g., the UV radiation and its direction, as well as design information, i.e., material properties, the geometry, and boundary conditions.
- Physical phenomena to model, e.g., radiative or conductive heat transfer, or deformation through thermal expansion.
- Discretisation schemes for time and space—a common step in FEA; in layman's terms, cutting the problem into manageable parts known as elements.
- A solving algorithm, generally implemented semi-automatically by the FEM software, but which can be tweaked, for example, to reduce solving time in exchange for accuracy.
- Outputs—shown in purple for thermal and in green for mechanical—e.g., temperature or displacements at each element, which also serve as inputs for the subsequent model, or even for the previous one in the case of infrared radiation.
- Post-processing, performed after the models, condenses the information into a summary result, allowing for a review of a large set of outputs; for example, converting displacement fields to the rigid-body motions of the mirrors.
- Finally, the results of the models are checked against the requirements, answering whether the design is compliant with the set requirements. This also provides an indication of the performance of the telescope as a whole, i.e., how far the result is from what is required.

The remainder of this chapter follows the modelling workflow outlined above, moving sequentially through each stage of the analysis. While the diagram in Figure 5.2 provides a useful high-level overview, the individual models and steps are more effectively understood through examples. Therefore, the following sections will review each stage using the preliminary design, which serves as a starting point for all subsequent modelling activities.

NOTE: The following sections report the COMSOL model and its workings using only 1 out of the 5 load cases. The complete results are left to Chapter 6. The LC used in the coming section is the maximum gradient (LC3). It provides an interesting case in terms of telescope behaviour.

For convenience, a short review of the load case and how it is implemented in the COMSOL geometry is given below. LC3, the gradient load case, is imposed by a cold LCT at −30 °C and a Sun input at a 45 ° angle. The surfaces on which the temperature is applied are, however, segmented so that some can be changed to impose the boundary conditions for, for example, LC4 (the conduction gradient). The surfaces on which these are imposed are shown in Figure 5.3.

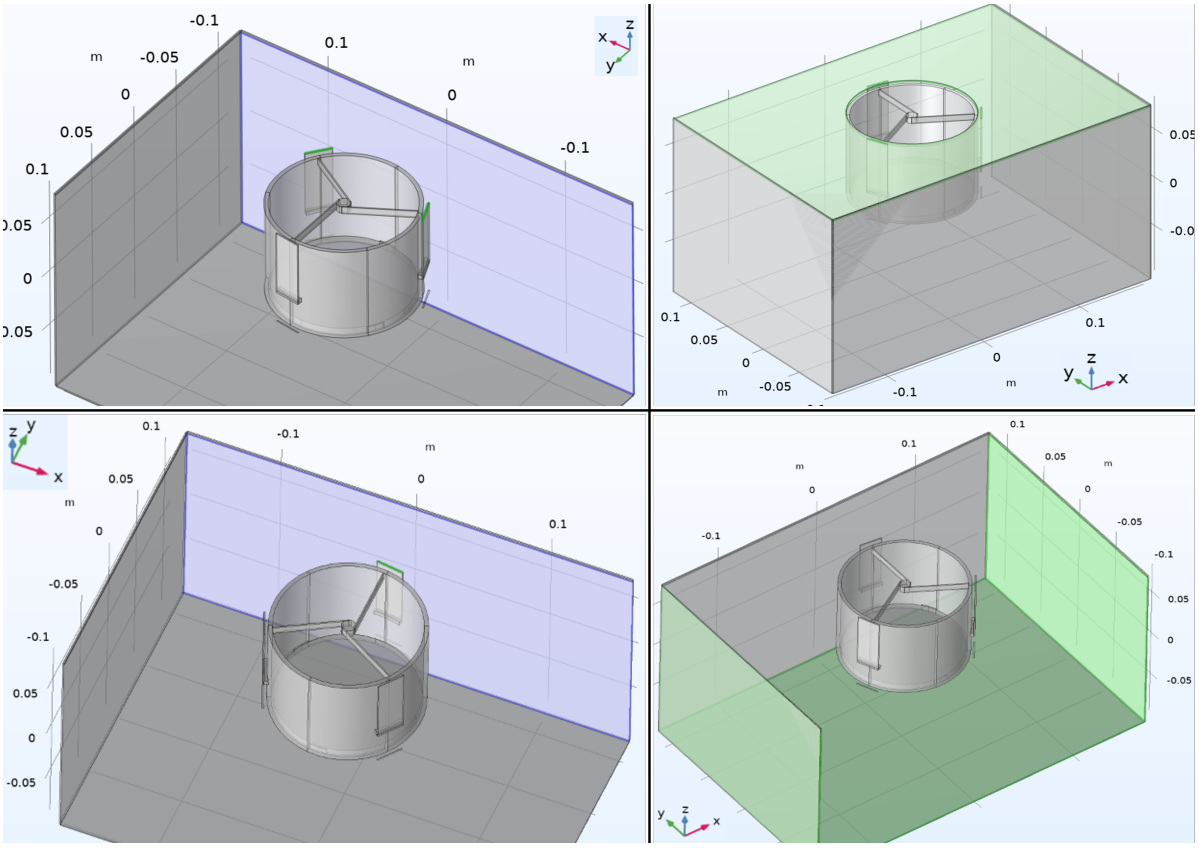

Figure 5.3: In clockwise direction the -y faces, front side faces , + y faces (inlcuding flexures), the other leftover faces, and finaly on the bottom left. the - y face.

The remaining load cases are using these boundary conditions, but change the magnitudes for each. As reported in table below 3.1, which is adapted from Table 5.1.

Table 5.1: Qualitative overview of radiative input conditions and affected interfaces for each load case.

Load Case	Solar Radiation 1368 [W/m^2]	IR Radiation 237 [W/m^2]	Albedo Radiation [%]	Interfaces [° C]
1 Worst-case Cold	-	-	-	-30 (all)
2 Worst-case Hot	0° incedence	-	-	+60 (all)
3 Worst-case Gradient	45° incedence	-	-	-30 (all)
4 Conductive Gradient	-	-	-	20 / 25 ($-y$/$+y$)
5 Operational Hot	-	0° incedence	30% (all) | 0 °incedence	50(all)

5.2. Radiative Heat Transfer Model

With convection being absent due to vacuum, thermal radiation becomes a much more significant heat transfer mechanism in space compared to on Earth. It is modeled in COMSOL using surface-to-surface radiation physics.

The emission of thermal radiation is dependent on temperature and described by the Stefan-Boltzmann law. It describes the total thermal radiation emitted by a blackbody as a function of its temperature. It is given by:

$$E = \sigma T^4 \tag{5.1}$$

where E is the total radiant exitance (W/m^2) emitted per unit area of the surface, T is the absolute temperature of the blackbody expressed in kelvin (K), and σ is the Stefan-Boltzmann constant, with a value of

$$\sigma = 5.670374419 \times 10^{-8}\ \mathrm{W\,m^{-2}\,K^{-4}}.$$

A blackbody is the term for the theoretical object that is a perfect emitter; for real surfaces, emission depends in part on the chemical composition and roughness of the surface. The total power emitted by a non-blackbody, or grey body, depends on its material and is commonly estimated by the emissivity factor, which is the ratio between the perfect theoretical blackbody emission and the actual emission of a material. For example, black paint, like a blackbody, has a high emissivity (0.8), whereas aluminium has a low emissivity (0.15). Each surface is assigned material-specific *emissivity* (ε) and *absorptivity* (α), which define how much radiation energy is emitted and absorbed [**?**].

The real optical properties are wavelength-dependent; however, the radiation encountered in space by the LCT has 2 sources, namely the Earth and the Sun. They emit in different parts of the electromagnetic spectrum, i.e., at different wavelengths of light.

The radiative emission is wavelength-dependent and described by Planck's law. Thus, the former explanation is not complete, but it holds for the solar part of the spectrum, given the caveat that the ratio between the real and blackbody emission is then called absorptivity. In both bands, by Kirchhoff's law, the percentage of radiation emitted equals the percentage absorbed. However, since the temperature of the LCT is never near that of the Sun ($\sim $5000Å), $the emission within the LCT is centered around the infrared part of the spectrum. Thus, int$

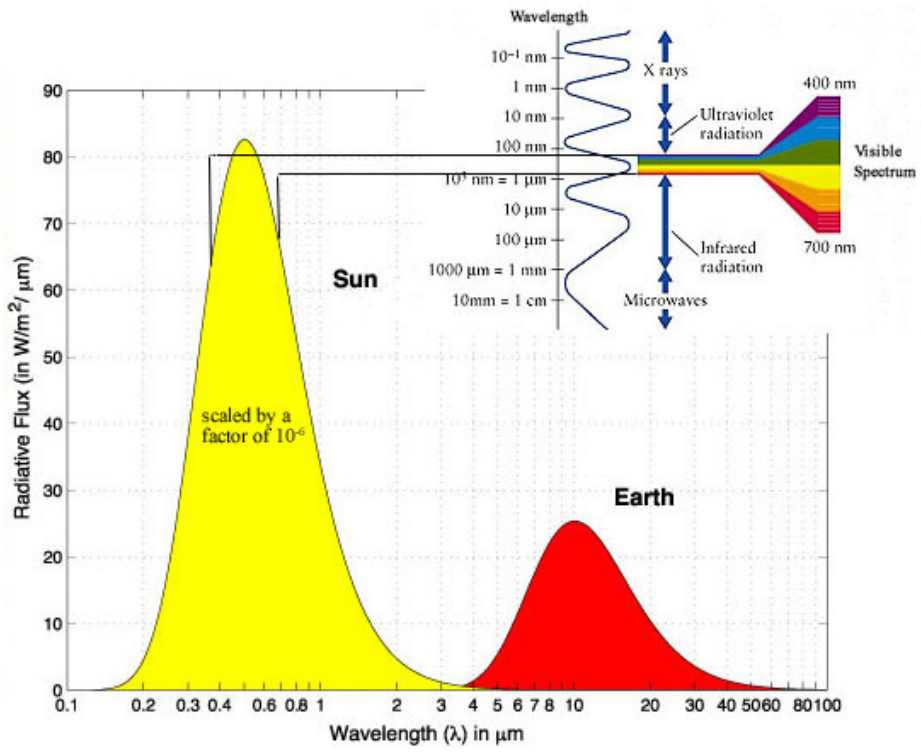

Figure 5.4: Shows the wavelength dependence of theoretical radiative flux of both the earth and sun. Note the solar flux is scaled by 10^{-6}. Source: © Yochanan Kushnir [13].

The radiation is emmited in all directions but only a part of it falls onto the LCT or a part of the LCT. The relation between the emmited radiation and received is captured in the radiative exchange factor. Which in part depends on the geometry of the design.

COMSOL calculates radiative exchange between surfaces based on mutual visibility, shadowing, and reflection between components. Is handled using the hemicube method, which approximates the visible surface area from each element. A conceptual figure explaining the computation of the viewable area is shown in 5.5.

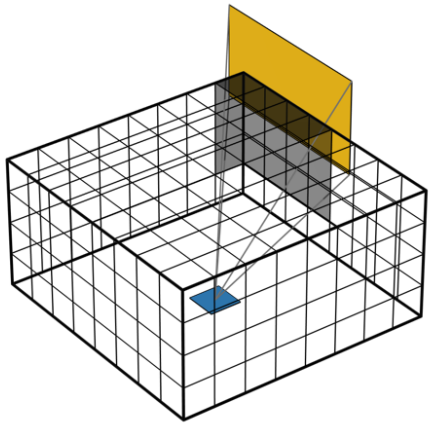

Figure 5.5: Shows a schematic of the hemicube method, which projects surrounding faces onto a set of pixelated boundaries to compute irradiance [14].

The figure above represents a surface or element, in blue. In yellow, another surface, the geometric part of their radiative exchange calculation is represented in the figure. Each surface has a virtual segmented box around one side of its surface hence, hemicube, "hemi" stems from "hemisphere". Drawing the lines for the element to the vertices of that surface provides a projection on the element's hemicube. This projection and the % on the segmented hemicube can be used to calculate the view between the two surfaces. This is a constant for given the model geometry does not change.

Reflected radiation, particularly on low-emissivity surfaces, is also taken into account. Multiple reflections between surfaces are modeled using a radiosity-based approach, allowing accurate prediction of net radiative heat transfer in enclosed or complex geometries.

In Table 5.2 below, the emissivity and absorptivity properties of the materials used in the model are reported. As well as the properties for some common paints and coatings used for passively controlling the radiative connection.

Table 5.2: Absorptivity (α), emissivity (ε), and their ratio (ε/α) for the materials used in thermal modeling. Adapted from values used in internally sourced documents at TNO.

Material	α **(Absorptivity)**	ε **(emissivity)**	ε/α
Aluminium	0.30	0.15	0.50
Titanium	0.50	0.30	0.60
C/C-SiC woven	0.80	0.80	1.00
Mirrors	0.04	0.10	2.50
White paint	0.20	0.85	4.25
Black anodised	0.90	0.80	0.89
Black paint Z307	0.95	0.82	0.86

In the preliminary model, raw material properties are used. It is likely that significant parts of the interior of the LCT will be coated with black paint to reduce stray light effects. The outer surface, which significantly increases radiation uptake, will most likely be coated white. However, the final decision depends entirely on the thermal control philosophy that is applied.

In an ideal case, the temperature is controlled passively by selecting appropriate coatings. This approach removes the need for heaters, which reduces cost, weight, volume, and complexity. However, this is a system-level decision that depends on several other variables. In the preliminary study the heaters and their effect are not incorporated. It may be the case that the C/C-SiC material properties allow a passively controlled thermal design. [59]

If the telescope can be shown to operate in the thermal load cases without the need for active thermal control, it provides a strong justification for further investigating the C/C-SiC material for this application. On the other hand, if it cannot operate under these conditions, the C/C-SiC telescope has a less favorable position.

Once the material properties and radiation input are applied to the geometry, the radiation received by the surface can be calculated; for example, in load case 3 this results in the surface irradiation shown in Figure **??**LC3 Prelim Irradiationfig LC3 Prelim Irradiationably, both the shadow from the spider and the reflection from the mirror surface can be seen in the figure. The latter is evident because the maximum at the bottom of the cylinder (1698$\tilde{\mathrm{W}}/\mathrm{m}^2$) is higher than the input radiation reported in Figure **??**LC13fig LC13able **??**rad loadstab rad loadsch can be explained by the reflection of the mirror.

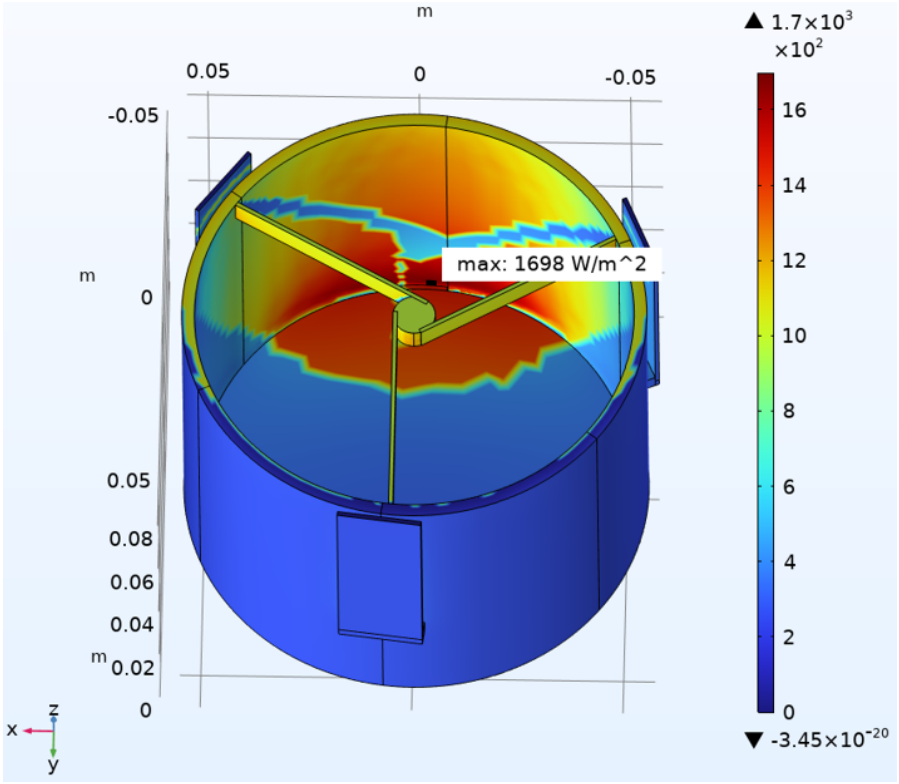

Figure 5.6: The radiation flux received in the preliminary model for load case 3 (gradient).

Part of the radiation received at each surface is IR, or long-wave radiation (LWR), from the temperature of the parts themselves. For example, using Equation~**??**eq: Stephan Boltzman for the nacelle surface at -30°C$:

$$E = \sigma T^4 = (273.15 - 30)^4 \times 5.67 \times 10^{-8} = 198 \left[\frac{W}{m^2} \right]$$

However, the temperature of the parts depends on their conductive connection. Therefore, the next section covers the modelling of this phenomenon within COMSOL. Wŕt. the modelling graph, the last two sections (5.2 **??**) cover the load-cases radiative exchange part of the heat-transfer model and radiative input loads, as well as the feedback connection from the temperature field, leaving the conduction model for the next section.

5.3. Conductive Heat transfer Model

To complete a thermal model and obtain the temperature fields, the conductive heat transfer between the components is incorporated. The material properties required are conductivity, density, and specific heat capacity. The conductive heat transfer between two parts or nodes is described by Fourier's law of heat conduction:

$$q = k \nabla T \tag{5.3}$$

Where q is the rate of heat transfer per unit of area, k is the material property describing how well it conducts, and ∇T is the temperature change between two points. When discretized for, the heat flow Q_{ij} from node i to node j is given by:

$$Q_{ij} = \frac{k \cdot A}{L}(T_i - T_j)$$

where:

- Q_{ij} is the rate of heat transfer from node i to node j [W],
- k is the thermal conductivity of the material between the nodes [W/m·K],
- A is the cross-sectional area through which conduction occurs [m^2],
- L is the distance between node i and node j [m],
- T_i and T_j are the temperatures at nodes i and j, respectively [K or °C].

Area and length are determined by the geometry and, together with the thermal conductivity, define heat conduction in the steady-state case. In the case of transient effects, the material's resistance to temperature change must be taken into account. This

thermal inertia is proportional to the mass and depends on the specific heat capacity of the material. When the specific heat capacity is multiplied by the material's density and volume (of a part or node), it gives the amount of energy required to raise its temperature by 1 Kelvin. Therefore, these properties must be assigned in the model. The values used in this model are reported below in Table 5.3.

Table 5.3: Thermal properties of materials used in the preliminary model [5, 21–24]

Material	**Conductivity** k [W/mK]	**Specific Heat** c_p [J/kgK]	**Density** ρ [kg/m^3]
Aluminium RSA-6061	169	900	2700
Titanium (Sheet Timet-550)	21.9	522	4500
C/C-SiC woven	25	620	1900
Zerodur	1.46	820	2530
Fused Silica	1.38	703	2200

Combining these with the thermal radiation model and the load cases, the complete temperature field over the telescope structure is calculated. For example, in load case 3 the temperature field is shown in Figure 5.7. Where the maximum temperature is experienced in one of the spider arms.

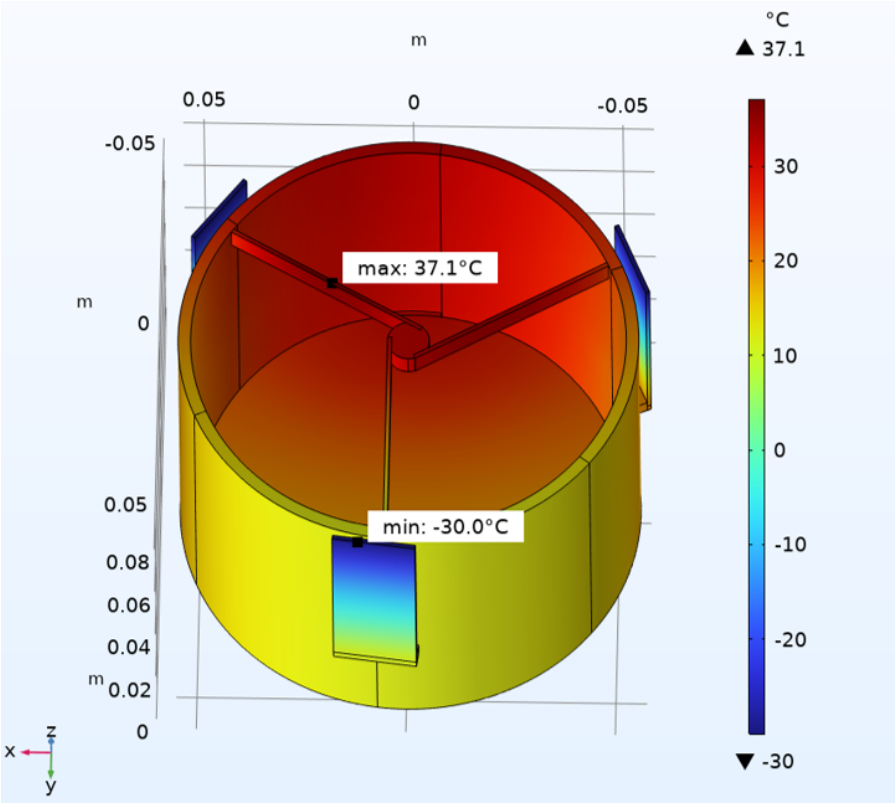

Figure 5.7: LC3 temperature field for the preliminary model showing a gradient over the whole structure of -30 to 35 °C

5.4. Structural Model

Given the temperature field solution is found it is used as input to obtain the deformation result. However first the boundary conditions need to be imposed as well as the relevant material properties. To limit the computation time required, the LCT nacelle is not incorporated in the solid mechanics analysis. The flexures are however taken into account, and this is where the boundary condition of the assembly is set. In this case, with a rigid connection to the flexure nacelle interface.

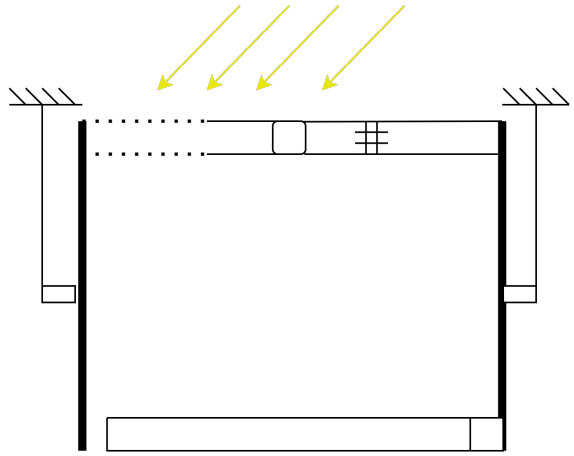

Figure 5.8: A cross section schematic of the parts involved in the Solid mechanics calculation of Load case 3. The yellow arrows representing the Solar incidence radation.

The deformation originates from the thermal strain induced by a temperature change w.r.t. a zero strain temperature. The latter is assumed to be $20^{\circ}C$ which is commonly the clean room temperature in which the telescope is assembled thus near zero strain/stress state is assumed. This assumption could be invalidated by the shrinkage of the epoxy adhesive after application and the fact that C/C-SiC is manufactured at a much higher temperature.

Finally a secant CTE model is used which is a linear approximation over a range of expected temperatures. Not all material suppliers provide a CTE over the range of interest. The ones gathered for the materials used in the model are reported in Table 5.4 and extrapolated where necessary.

Table 5.4: Material properties used in the solid mechanics module [**?**, 5, 21–23, 28, 32]. * C/C–SiC properties are typical literature values and depend heavily on the methods used and base materials chosen [33]. ** 20, MPa is the shear-stress yield point.

Material	**CTE** $[\mu m/mK]$	**E[GPa]**	**G[GPa]**	ν	$\sigma_y\,[MPa]$
	Secant coefficient of thermal expansion	Youngs modulus	Shear modulus	Poissons ratio	yield stress
RSA6065-T6 Alu	22.6	70	27	0.3	315
Timet-550 Plate	8.8	110	41	0.33	900
C/C-SiC in-plane	1.1 to -1	70*	20*	0.3*	230
C/C-SiC out-plane	4 to 2.1	20*	5*	0.3*	230
Zerodur	0.1	90	36	0.24	100
Fused Silica	0.55	73	31	0.16	54
EC2216	102	0.070	0.0022	0.592	20**

The Solid Mechanics module, once set up, can be used for structural analyses, i.e., determining the first eigenfrequency or g-load based on the MAC curve, as well as thermo-mechanical analysis using the thermal expansion interface. Figure 5.9 shows the deformation resulting from the temperature field shown in Figure 5.7. The deformation is much higher on the cold side, which might seem counterintuitive. However, its cause becomes evident when considering that the strain-free temperature is set at 20 °C. The cold side, at 30 °C, is farther from equilibrium and therefore shrinks more than the hot side expands. This effect is also visible in the side view shown on the right.

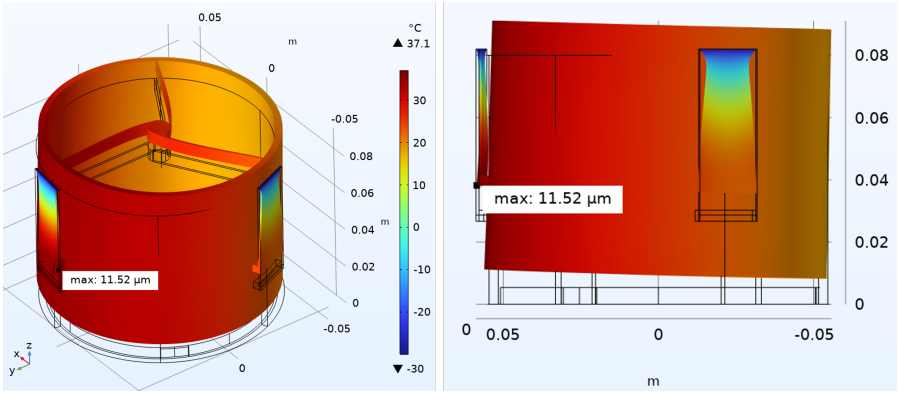

Figure 5.9: The total deformation with a 1000x scale factor in the preliminary model for LC3 including a side view on the right. Where the coloring coresponds to the temperature

An additional observation from the deformation pattern is that the shrinkage is driven mainly by the flexures, which obscures the deformation of the mirrors and/or their support surfaces. To close the modelling loop for this preliminary design, the mirrors' rigid-body motions and surface deformations are required. Therefore, the mirror surface deformation is obtained from the final result and post-processed. In this way, the effect on the mirror itself can be isolated and the results of multiple load cases can be summarised. The required post-processing is reported in the following.

The deformation of the spider and M1 is shown in Figure 5.10, in which the rigid-body motions—tip (Rx), piston (Dz), and decenter (Dy)—are clearly visible, with both mirrors moving upward and tilting diagonally about the x-axis.

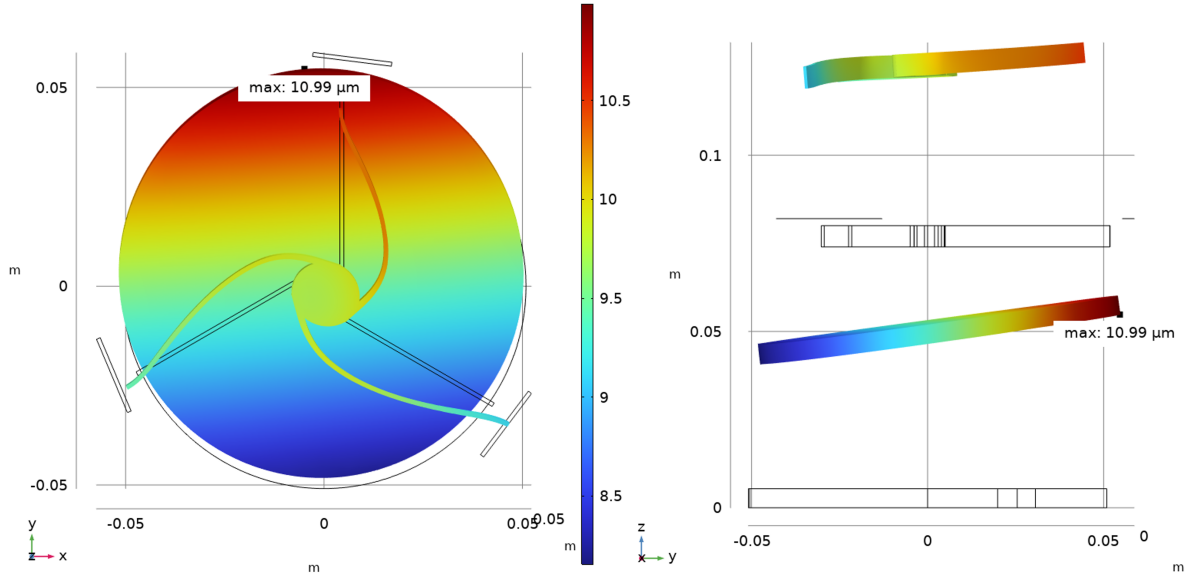

Figure 5.10: Deformation in the preliminary model of the spider support and mirror, amplified by a factor of 5000.

The figure above also motivates the required post-processing: the telescope moving as a whole does not necessarily affect performance. As reported in Section 2.6, the performance metrics relate to relative rigid-body motions, which are clearly much smaller than the total displacement shown above.

Solver configuration

Finally, a steady state, or what is known in COMSOL as a stationary solver, is added. In which the load cases are imposed. As well as setting up the variable sweep extension for each of the 5 load cases.

The variable sweep allows the efficient use of the solver set up and the solved model to find the solutions of the same model when certain variables are changed. In this case the sweep extension is used in the next chapter to vary the material properties in the model.

5.5. Post-Processing of Thermo-Mechanical Results

To interpret the results of the finite element analyses and evaluate the thermo-mechanical performance of the optical components, a dedicated Python-based post-processing pipeline was developed. The Python scripts focus on quantifying both rigid body motions and surface deformations of the optical faces. These scripts enable the analysis of the full the design by considering the primary information and summarizing it.

However, the trade-off is a loss of information compared to considering the complete FE solution. Figure 5.11 shows the deformation results of the preliminary model for each of the 5 LCs and each of the 5 material cases. The results are covered in the next section, but the figure conveys the need for a method which summarizes the information. The information of the optical surfaces is convoluted and harder to deduce if one has to comb through all of the 25 solutions for each model change.

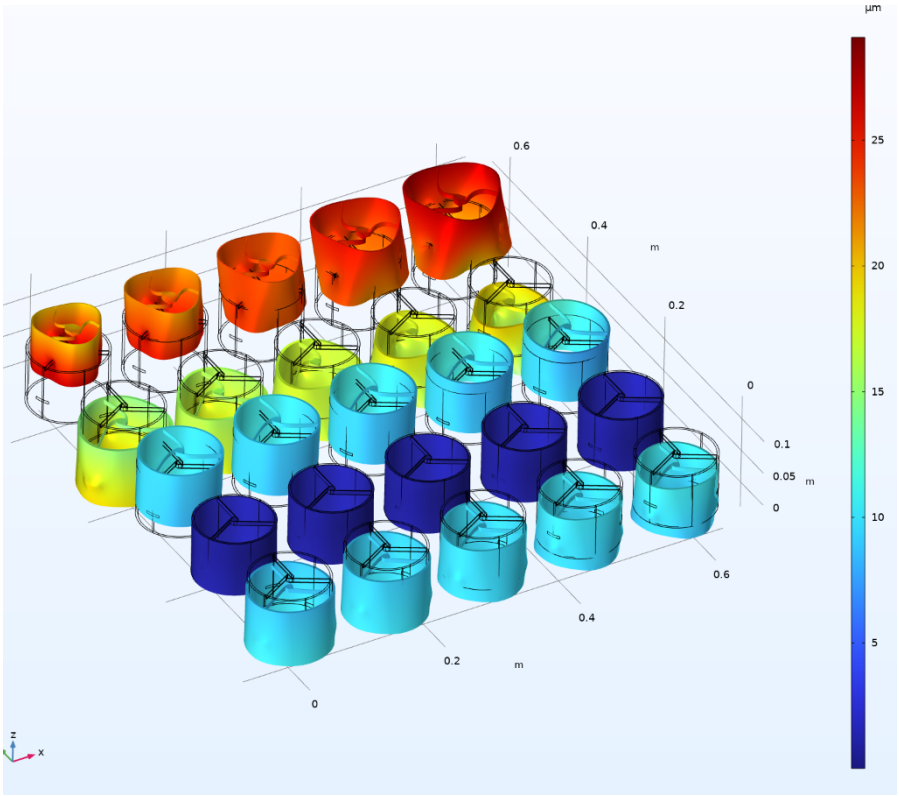

Figure 5.11: All of the displacement results for the 5 load cases and 5 sets of material properties. LC1 shown at the top and LC5 at the bottom. Scale factor : 2000

The FEA output used in the post processing consists of nodal displacement fields (u, v, w) for each optical surfaces as a result of the thermal load cases. These results are exported as text files containing the original coordinates (x, y, z) along with the displacement for each node on the surface of both mirrors.

5.5.1. Zernike-Based Rigid Body Motion Extraction

As explained in 2.6 the rigid body motions are used to quantify the performance of the telescope. These RBMs are not directly available from the FEM results. Hence some post processing is required to extract these metrics. The displacement fields of the mirror surfaces are utilized as input for a Zernike decomposition. The decomposition fits a set of functions to the the out-of-plane deformation $w(x, y)$ of the mirror surfaces. These functions are orthogonal and were first derived by the Dutch Nobel Prize winner Frits Zernike. The surface coordinates (x, y), are scaled to a unit circle and fitted using Zernike polynomial basis functions $Z_n^m(r, \theta)$ defined on the unit disk:

$$r = \frac{\sqrt{x^2 + y^2}}{R_{\max}}, \qquad \theta = \arctan(y/x),$$

where $R_{\max}$ is the maximum radial extent of the aperture.

The surface is approximated as a linear combination of Zernike modes (on the unit disk, $0 \leq r \leq 1$):

$$w(x, y) \approx \sum_{i=1}^{N} c_i Z_i(r, \theta) \tag{5.4}$$

with even (cosine) and odd (sine) angular parts

$$Z_n^m(r,\theta) = R_n^m(r)\cos(m\theta), \qquad Z_n^m(r,\theta) = R_n^m(r)\sin(m\theta),$$

and radial polynomial

$$R_n^m(r) = \sum_{k=0}^{(n-m)/2} (-1)^k \frac{(n-k)!}{k!\left(\frac{n+m}{2}-k\right)!\left(\frac{n-m}{2}-k\right)!} r^{n-2k},$$

defined for integers $n \geq 0$, $m \geq 0$ with $n - m$ even (otherwise $R_n^m \equiv 0$). Where the $Z_n^m(r,\theta)$ map to $Z_i(r,\theta)$ from Equation 5.4 by OSA/ANS indexing.

The sum of these polynomials provides a description of any deformation pattern on the unit disk. In perfect accuracy if an infinite amount of polynomials are used. Each polynomial is multiplied by a coefficient (c_i) and summed as in 5.4. For a given deformed surface, i.e., the top side of the M1 shown in Figure 5.10, these coefficients can be found. Since the polynomials and coordinates of the points $w(x,y)$ that describe the deformed surface are known, the coefficients $\{c_i\}$ can be obtained via least-squares fitting:

$$\mathbf{c} = \arg\min_{\mathbf{c}} \|\mathbf{Ac} - \mathbf{w}\|_2^2, -> \mathbf{c} = (A^T A)^{-1} A^T \mathbf{w} \tag{5.5}$$

where **A** is the Zernike design matrix (polynomial basis functions), **c** is the vector of coefficients, and **w** is the vectorized surface heights.

The first few modes, with their OSA/ANSI index j, Zernike indices (n,m), radial polynomials $R_n^m(r)$, and angular dependence, are shown in Table 5.5.1 below:

[H] height$j$	(n,m)	Name	$R_n^m(r)$	Angular term
0	(0,0)	Piston	1	1
1	(1,1)	Tilt (x)	r	$\cos\theta$
2	(1,−1)	Tilt (y)	r	$\sin\theta$
3	(2,0)	Defocus	$2r^2-1$	1
4	(2,2)	Astigmatism (0°)	r^2	$\cos 2\theta$
5	(2,−2)	Astigmatism (45°)	r^2	$\sin 2\theta$
6	(3,1)	Vertical coma	$3r^3-2r$	$\cos\theta$
7	(3,−1)	Horizontal coma	$3r^3-2r$	$\sin\theta$
8	(3,3)	Trefoil (x)	r^3	$\cos 3\theta$
9	(3,−3)	Trefoil (y)	r^3	$\sin 3\theta$

The coefficients corresponding to piston (Z_1), tip (Z_2), and tilt (Z_3) quantify rigid body motion (RBM) of the surface. Their differences between surface pairs yield the relative motion:

$$\Delta\text{Piston} = R_{\max} \cdot (c_1^{(2)} - c_1^{(1)}), \quad \text{m} \tag{5.6}$$

$$\Delta\text{Tip} = (c_2^{(2)}/R^{(2)} - c_2^{(1)}/R^{(1)}), \quad \text{rad} \tag{5.7}$$

$$\Delta\text{Tilt} = (c_3^{(2)}/R^{(2)} - c_3^{(1)}/R^{(1)}), \quad \text{rad} \tag{5.8}$$

where superscripts (1) and (2) denote the two surfaces being compared.

Additionally, the average in-plane displacement $(\bar{u},\bar{v})$ is computed to determine the decentering in µm. This yields a five-degree-of-freedom RBM characterization: piston, tip, tilt, and decentering in x and y. Rotation about the optical (z) axis is not assessed because of the system's rotational symmetry. The RBMs, some of which are shown in Figure 5.12 below. These can be reconnected to the sensitivities, enabling determination of the WFE attributable to each of these deviations.

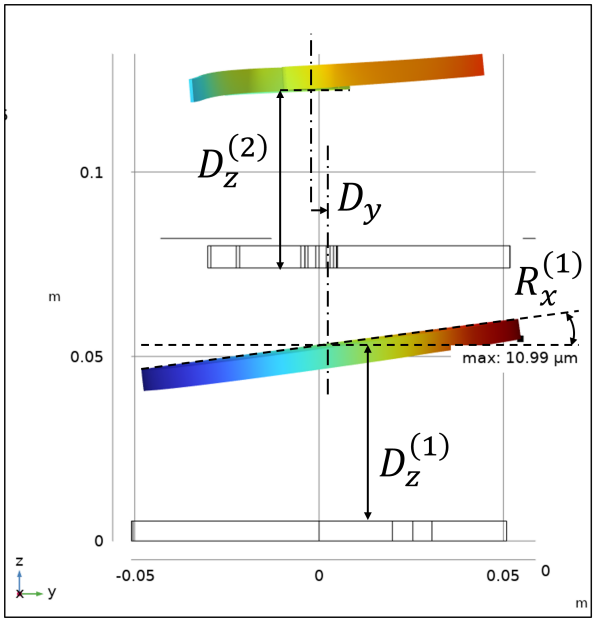

Figure 5.12: Some of the RBMs are visible in this side view of the LC3 solution. The piston is visualized per mirror (Dz) the Δ piston would be the difference between the arrows shown. The same holds for the rotation; however, the 5000x scale factor is too low for the M2 Rx to be visible.

Finally, due to the axial symmetry of the system, the sensitivities to tip and tilt are equal. To compress the results, the deltas are calculated as per Eq. 5.7, after which they can be combined using RMS since they are orthogonal.

Table 5.5: M1 rigid-body motions and resulting WFE contributions resulting from the LC3 contributions

RBM [unit]	Value	WFE sens.	WFE contrib. (nm RMS)
Δ Dx [μm]	0.32	10.5	3.34
Δ Dy [μm]	-1.24	10.5	13.04
ΔPiston (Dz) [μm]	0.04	70.5 (7.7)	2.55 (0.28)
Δ Tip & Tilt Rxy [μrad]	2.10	1.43	3.00

To isolate surface deformations, the first three modes (piston, tip, tilt) are subtracted enabling residual shape analysis independent of RBMs.

$$w_{\text{clean}} = w - \sum_{i=1}^{3} c_i Z_i(r, \theta), \tag{5.9}$$

This results in a graph of the residual surface deformation of the mirror surface as shown in Figure 5.13 below. Showing a symmetrical, across the yz plane, concave shape. Again, this is not equivalent to the WFE but does provide an insight into the deformation behavior of the mirror. In this case it seems to be compressed and bent. That said, the surface deformation of either mirror affects the WFE directly and thus should ideally be minimized.

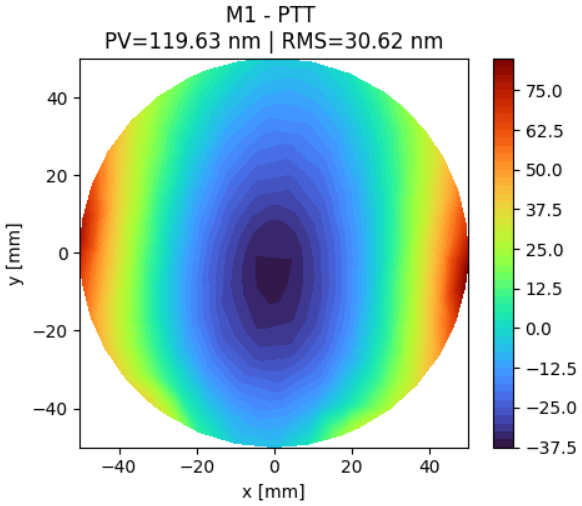

Figure 5.13: The residual surface deformation of the primary mirror in load case 3

One objective of the post-processing pipeline is for analysis of the surface pairs for each of the load cases and how they are affected by the tunable material properties. For example, the deformation data is stored and processed for a set of 5 FEM solutions. After which, the RBM values are stored and visualized in a summary figure. Figure 5.14 shows an example of this summary for load case 3 for 5 different material property sets. The RBMs are split into 3 subplots. First on the left is the piston of load case 3 and the change in the result due to the changing properties of the C/C-SiC material.

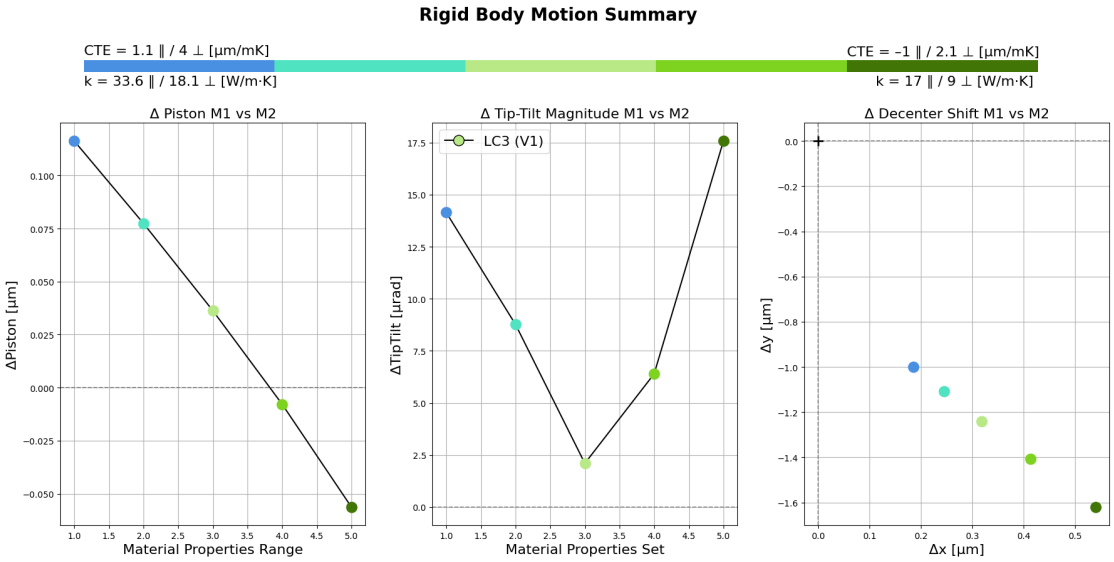

Figure 5.14: Relative mirror rigid body deformation in LC 3 and their sensitivity to material property change.

In the middle, the combined tip and tilt are plotted; on the right, the decentering vector is shown as a point in the xy-plane. The latter represents the in-plane relative shift between the two mirrors. The origin is the center of M1; the center of M2, and its displacement, is indicated by the colored dot.

6

Final Model Results: Performance and Compliance Range Given the CTE and Conductivity Uncertainty.

The model and post-processing scripts enable the evaluation of a first version of the telescope. From which the model is updated and extra details are added. The aim is to provide a more detailed and realistic representation of the telescope within the FEA model.

The updated configuration can be compared to the preliminary model to assess the impact of the implemented changes. In addition, the model is further exploited to investigate the sensitivity of the results and to verify both the performance and structural integrity of the final design. This process addresses the following questions:

How do CTE and thermal conductivity variations affect thermoelastic deformation in the preliminary model, and which model/design updates are needed to better meet the objective and improve predicted performance?

However, the updates are in part based on the primary model and its behavior. Which are reported in the following section.

6.1. Evaluation of The Preliminary Model

With the thermo-mechanical model established, the investigation of the impact of uncertainties in the material properties. As discussed previously, the thermal performance is primarily influenced by two key parameters: the thermal conductivity and the coefficient of thermal expansion (CTE). To explore their effects, the five distinct load cases were evaluated using five different sets of these material parameters. The parameter ranges were selected based on values reported in the literature [5].

The values for the relative RBMs are summarized for 3 load cases in the same figure. The LC3 gradient, LC4 conductive gradient, and LC5 operational hot are incorporated. Where LC1 and LC2 are left out because they represent the environment in which the LCT needs to survive. The summary of the results is captured in Figure 6.1 below.

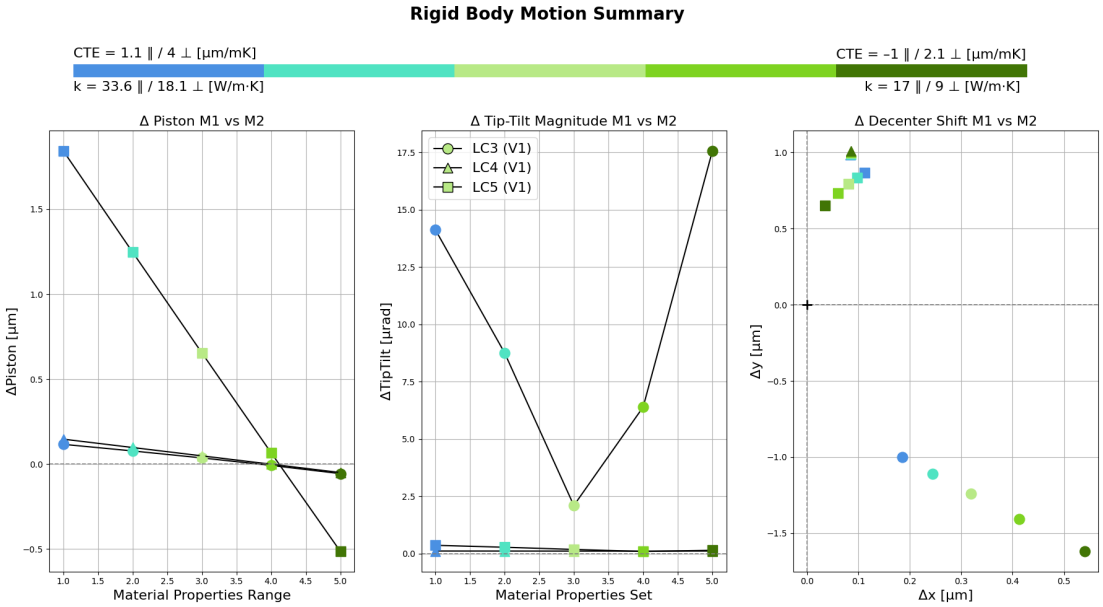

Figure 6.1: The relative rigid body motions for all operational load cases, 3 worst-case gradient, 4 conduction gradient, and 5 hot operational.

The behavior in the graphs above is driven by the CTE change and conductivity change as a result of the tunable SiC %. As a reminder, a higher SiC % corresponds to a higher CTE and conductivity. Which, in terms of mitigating thermo-mechanical performance, have an opposing effect. I.e., decreasing CTE should be a net positive, whereas decreasing conductivity would be a net negative. For convenience the material cases are again posted in Table 6.1 below. In addition, the RBM summary plots use the same colors for each of the material sets. Ranging from dark blue to dark green, as a reminder, **the bar at the top of the summary figures includes the extremes of the properties.**

Table 6.1: Material cases with anisotropic thermal properties for C/C-SiC: In directions parallel (∥) and perpendicular (⊥) to the fiber orientation. The first set is based on high SiC % (35–40 vol%) decreasing with each. *Note values are rounded.

Material cases	**CTE [μm/mK]**		**k [W/mK]**	
Parallel Perpendicular	∥	⊥	∥	⊥
1	1,1	4,0	33,6	18,1
2	0,6	3,5	29,5	15,8
3	0,1	3,1	25,3	13,6
4	-0,5	2,6	21,2	11,3
5	-1,0	2,1	17,0	9,0
Step size	0,525	0,475	4,15	2,275

The piston value is relatively low, ranging between -0.05 & 0.12 μm. Its small value relative to the angular behavior is hard to discern in the results. The tip, tilt and decenter behaviors are covered in the comming section.

Using this figure, the results can be related to the original requirements. As reported in section 2.6, for convenience, the rigid body deformation limits leaving 40 nm RMS for the surface deformation-induced WFE:

$$\Delta Dy = \Delta Dy = 1\ \mu m, \Delta Dz = 3\ \mu m, \Delta Rxy = 8\ \mu rad,$$

For example, if limits on the allowable rigid body motions are set. Starting at the values used in the example in Section 3.2. Most of the cases within the figure above fall well within these values, as is clear from Figure 6.1. Hence, the RBM maxima are reduced to decrease the allowable and cut the number of feasible material solutions, leading to 6.2.

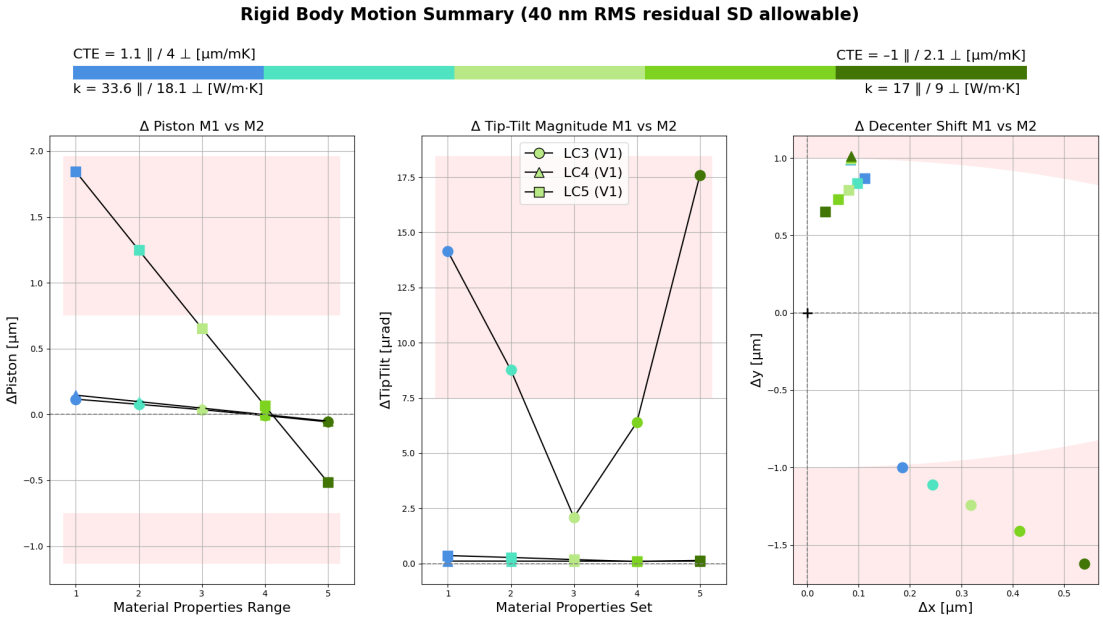

Figure 6.2: RBM summary including allowable displacements: $|Dz| < 0.75\ \mu m$; $Rxy < 7.5\ \mu rad$; $Dx^2 + Dy^2 < 1$.

This figure shows how the original requirements can be related to the post-processed results. Completing the method diagram as shown in Figure 6.3. The comparison to the requirements informs the next design iteration, as reported in.

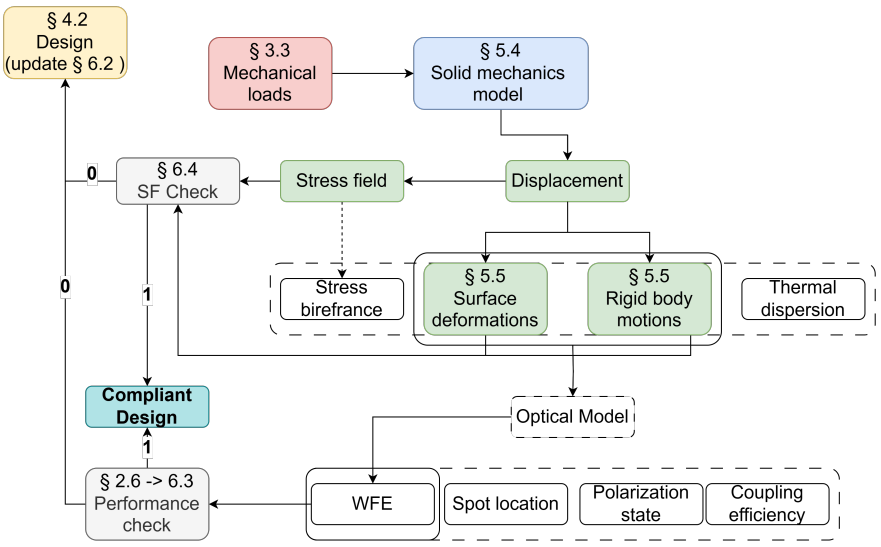

Figure 6.3: The last part of the modeling diagram as covered by the previous section.

The information in these summary graphs is sufficient to assess the RBM-based performance check. However, the deformation of the whole telescope is captured only in the complete FEA results, which contain additional information that provides insights into the interaction of the parts. This interaction might change when the design is updated; hence, a deeper dive into some of the behaviour is reported in the next section.

6.1.1. Deformation Behaviour Resulting from the Material Property range

Most notably, all RBM summary figures, e.g., Figure 6.2 show a distinct V-shape tip-tilt pattern (middle graph) for LC3. This shape is present in all cases but is significantly less pronounced in the other 2. Therefore, the effect is analyzed using LC3. Now the shape or nature of the temperature field does not change as a result of the material properties. It is only the magnitudes that change, i.e., hot parts get hotter and cold parts colder. The temperature field characterizing LC3 is shown in Figure

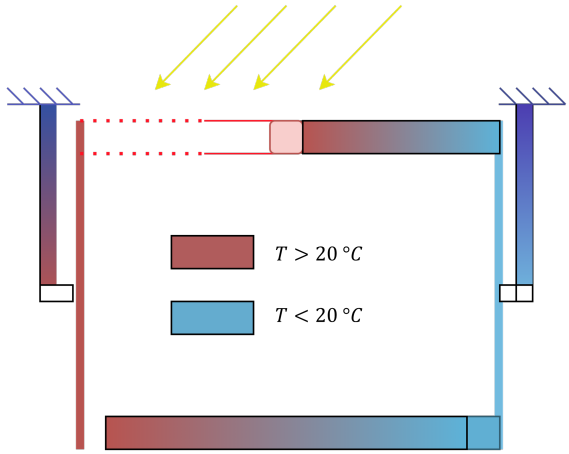

Figure 6.4: A schematic representation of the temperature field of LC3 w.r.t. the reference temperature (20°C)

For completeness, the temperature of the tube for material case 1 (MC1) 13.2 – 34.3°C and for MC 5 8.36 – 41.5°C.

The hypothesis is that flipping the sign of the coefficient of thermal expansion inverts the deformation pattern of the cylinder, which would explain the observed pivot around the zero-CTE mark. If you would plot the CTE as an absolute value it would have a similar shape.

The hypothesis disregards the role of thermal conductivity changes, as an decreasing conductivity would cause a larger gradient due to increased resistance. Which would result in larger rotations, which is not observed in the first 3 material cases. Thus the decreasing conductivity is inconsistent with the observed deformation change. I.e., CTE property probably dominates the behavior in this LC.

To illustrate angular deformation behavior, Figure 6.5 shows a cross-section for the two most extreme material cases.

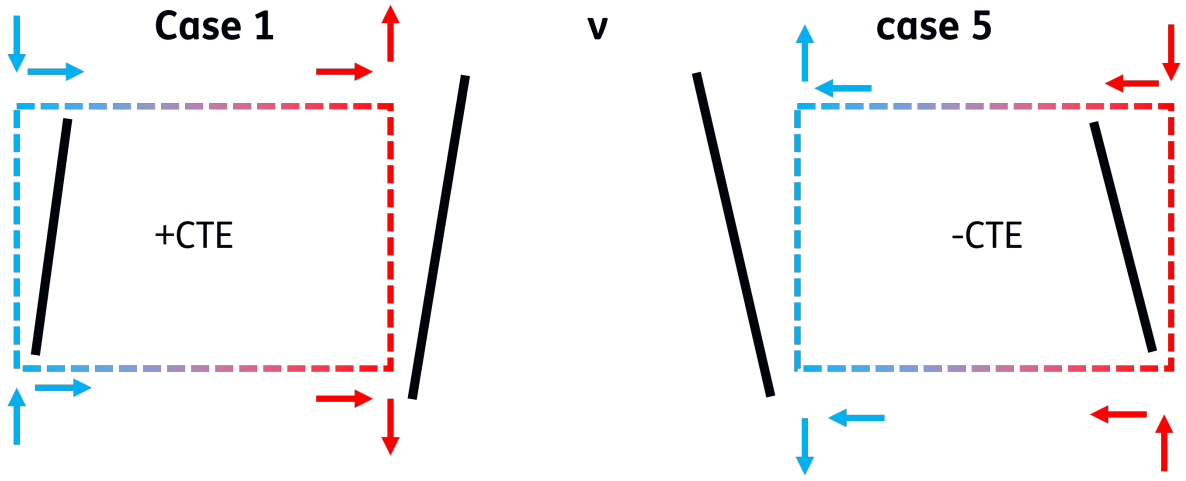

Figure 6.5: Schematic cross-section showing gradient-induced deformation for two extreme material cases.

It is important to note that the reference temperature, or zero-strain temperature, is 20°C. From this value, any temperature increase causes expansion in regions with a positive CTE. In the cross-section, three main components can be identified: the cylinder, the M1 mirror, and the spider. The M1 has a constant CTE of $0.5 * 10^{-6} m/mK$, while both the cylinder and spider feature varying CTE values as per Table 6.1.

Considering the behavior of each component individually, the interactions at the cylinder-spider and cylinder-M1 interfaces can be deduced:

- In the positive CTE case, the cylinder, spider, and M1 contract on the cold side and expand on the hot side.
- In the negative CTE case, the cylinder and spider expand on the cold side and contract on the hot side, while the M1 behavior remains unchanged.

- In both cases, the magnitude of the CTE in C/C-SiC is higher than that of M1, resulting in more significant deformations in the cylinder and spider.

Combining these effects, Figure 6.6 can be interpreted as follows: in case 1 (positive CTE), the top of the cylinder wall contracts more strongly due to the higher CTE magnitude. On the hot side, the wall is pushed outward instead of being pulled inward. The opposite effect is seen in case 5 (negative CTE). Given that the magnitude of the CTE changes more significantly than the thermal conductivity, the CTE dominates the deformation, reducing the angular deviation.

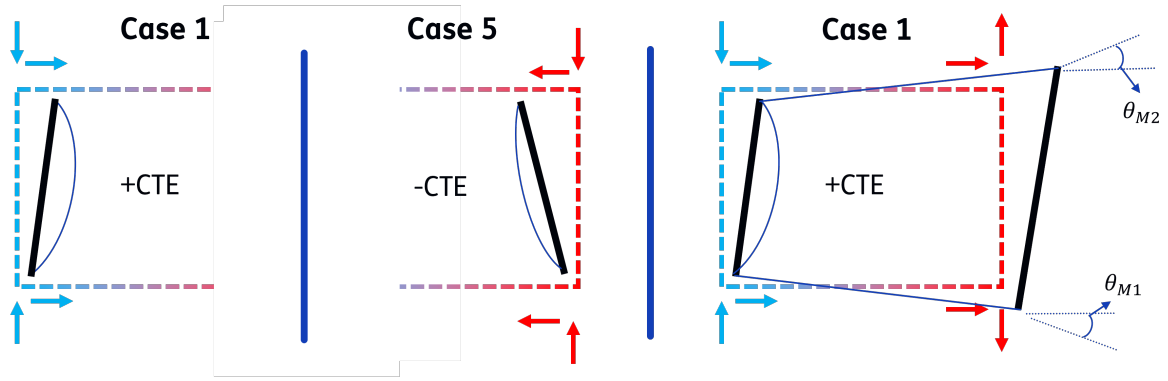

Figure 6.6: Schematic illustration of gradient-induced bending and corresponding angular displacement.

The delta in total angular displacement—i.e., the norm of the difference in tilt and tip—is always positive. This angular displacement is schematically represented on the right side of Figure 6.6. Finally, due to the angular alignment of the M1 and spider, the cylinder is also expected to bend inward, particularly on the contracted side, as depicted in the schematic. Figure 6.7 shows the side view for material cases 1, 3, and 5, with case 5 shown in front.

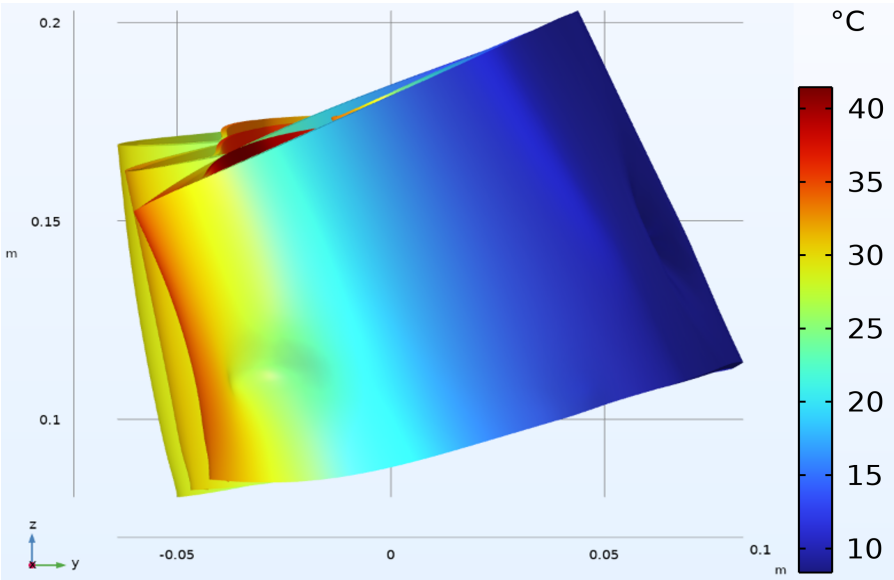

Figure 6.7: Side view of deformation in LC3 for material cases 1, 3, and 5 (front to back), color-coded by temperature. Deformation scale factor = 10000

The complete deformation pattern obtained from the FEA is more complex due to several factors: added stiffness from flexures, mismatched CTEs between components, and the inherently three-dimensional nature of the deformation. The cylinder's shape approximates an ellipse, as shown in the top view in Figure 6.8.

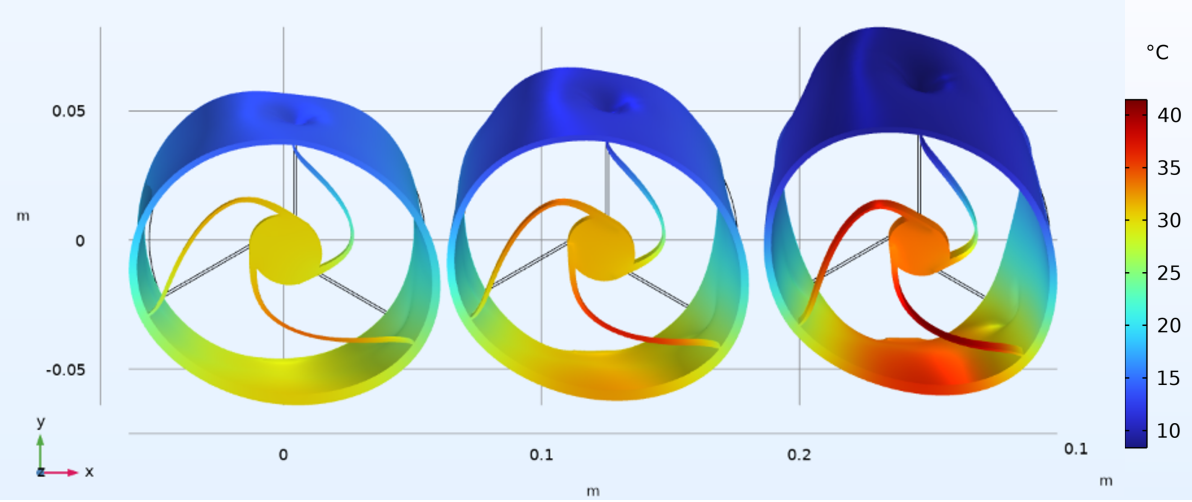

Figure 6.8: Top view of deformation in LC3 for material cases 1, 3, and 5. cylinder shape resembles an elliptical profile. Deformation scale factor = 10000

Figure 6.9 shows an isometric view of the three material cases, with the undeformed wireframe included as a reference. The upward deformation relative to the wireframe is primarily caused by the flexures, which are not shown in this figure.

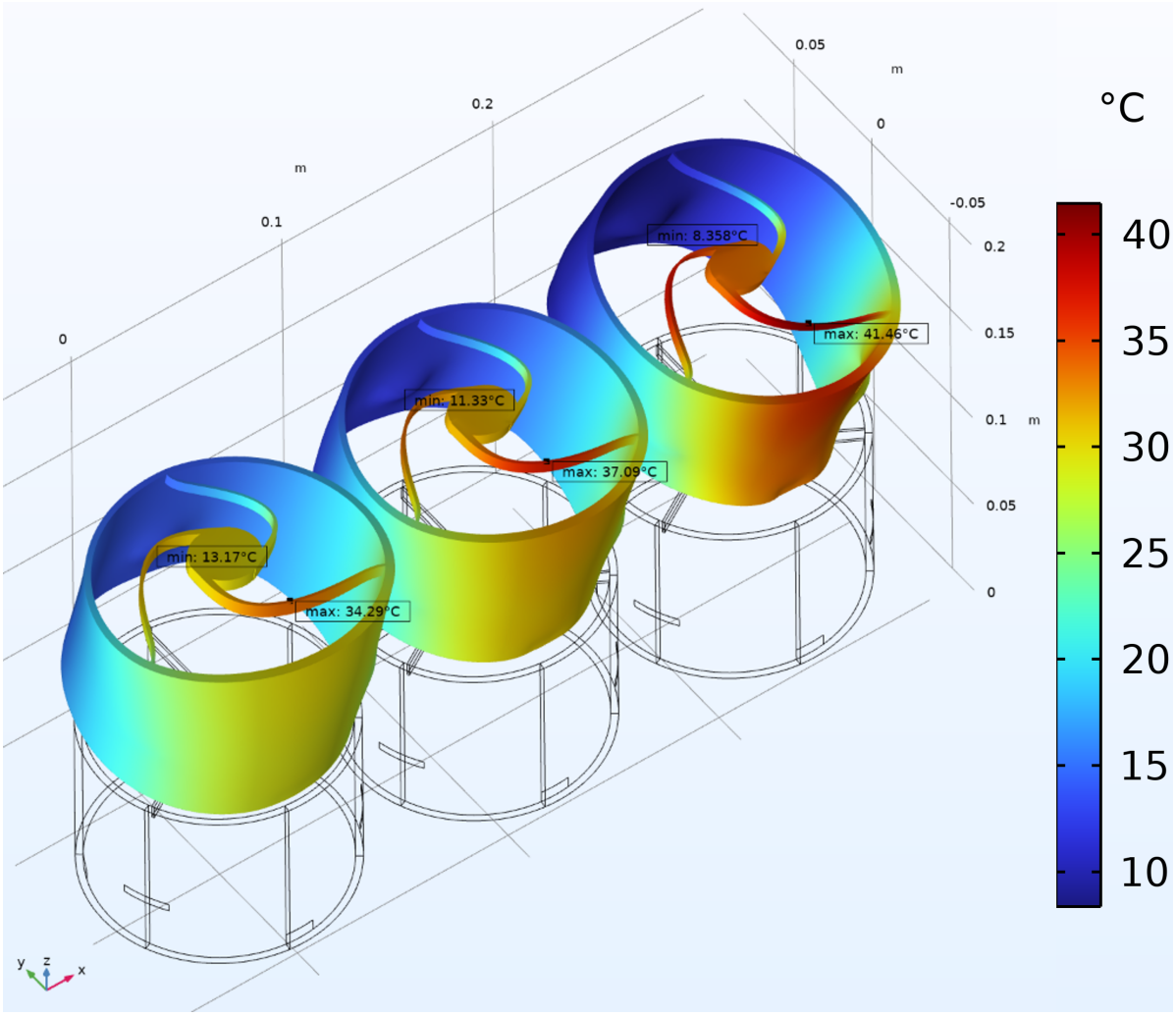

Figure 6.9: Isometric view of deformation in LC3 for material cases 1, 3, and 5, with wireframe showing the undeformed geometry. Deformation scale factor = 10000

Angular Deformation Behaviour

The behavior of the telescope tube under thermal loads is of primary interest to the case study. Thus the analysis is verified by varying the CTE values of the components; 2 sets are considered:

- Setting the cylinder CTE to 0 in all directions while applying the material cases to the spider.
- Setting the spider CTE to 0 in all directions while applying the material cases to the cylinder.

The decoupling of the CTE variation of the spider and the cylinder can show their individual contributions to the deformation as a whole. A side view of both is shown in figure 6.10. This shows little to no bending of the cylinder in the case of the 0-CTE cylinder on the right. The opposite is observed on the left side of the figure, where the cylinder clearly bends. These observations support the analysis that the spider has little influence and that the main effect is due to the cylinder.

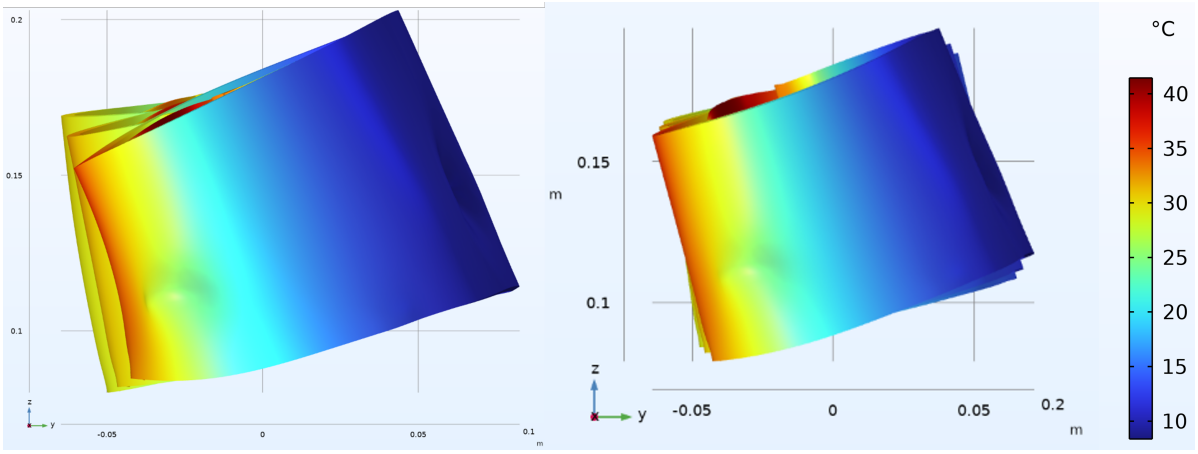

Figure 6.10: Deformation (×10,000) resulting from LC3 (gradient load). Left: zero CTE applied to the spider; right: zero CTE applied to the cylinder, with the other component using the same variable CTE material cases as before. Side view shown: case 5 in front, followed by cases 3 and 1, respectively.

The delta values for the 0 CTE cylinder are gathered as well and shown in figure 6.11. Which no longer shows the V shape as was seen in the RBM summaries, as well as significantly decreasing the magnitude of the deformation.

All of these findings support the analysis as set out in the previous section. Hence, the gradient load cases and the induced deformation are driving arguments for aiming the CTE towards the 0 value in the in-plane direction.

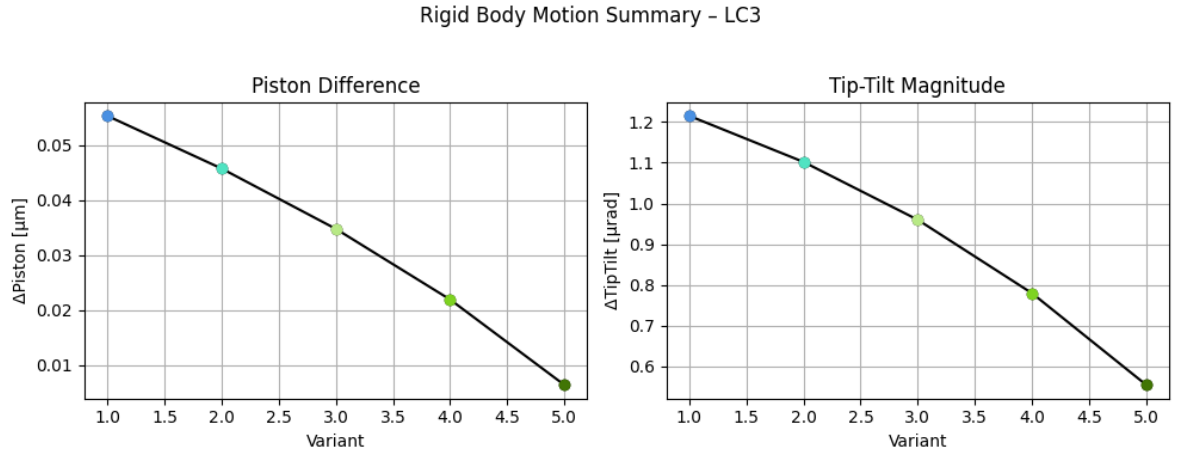

Figure 6.11: Relative mirror behavior for LC3 with a 0 CTE cylinder.

The influence of the flexures might also be significant; hence, the iteration takes this into account.

Finally, the decenter in the x- and y-directions can also be deduced from, for example, Figure 6.8, where the deformation of the tube increasingly pulls M1 toward the positive y-direction. Since its center is the origin used to calculate the relative decenter, this shape is consistent with the decenter graph.

6.2. Model Refinements and updates

From the insights of the preliminary model, a couple of updates are deemed necessary. The emphasis was put on changing the flexure geometry and adding details to M1 and M2 as well as updating their interfaces.

6.2.1. Terminal Volume

The terminal volume is reassessed based on the volume percentage of the current internal terminal design. This was estimated by comparing the volume of the current telescope design to that of the nacelle, resulting in a ratio of approximately 40%. To account for the likely need to add additional lenses and to remain conservative, the dimensions were adjusted to target a ratio of around 30%.

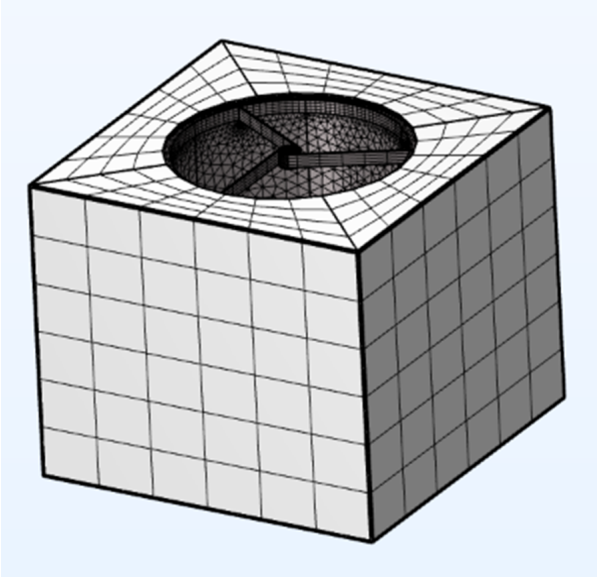

Figure 6.12: Updated LCT and telescope geometry scaled to 30% of the nacelle volume, including the finite element mesh used for analysis.

6.2.2. Adhesive Spot for M1 and M2 Interfaces

Given that the final performance in WFE is governed by the mirror surfaces, an increase in model fidelity was deemed necessary in this area. For this purpose, a dedicated part was added for the M2 mirror, and a central aperture was implemented in the M1 mirror to allow the light bundle to pass through.

In parallel, the mechanical connections between the mirrors and the supporting structure were updated to explicitly model the adhesive interfaces. For the M2, adhesive spots were added between the M2 support and the spider cylinder, as shown in Figure 6.13. The spots are evenly distributed to provide uniform load transfer, while their dimensions were conservatively chosen minimum adhesive thickness of 200 μm.

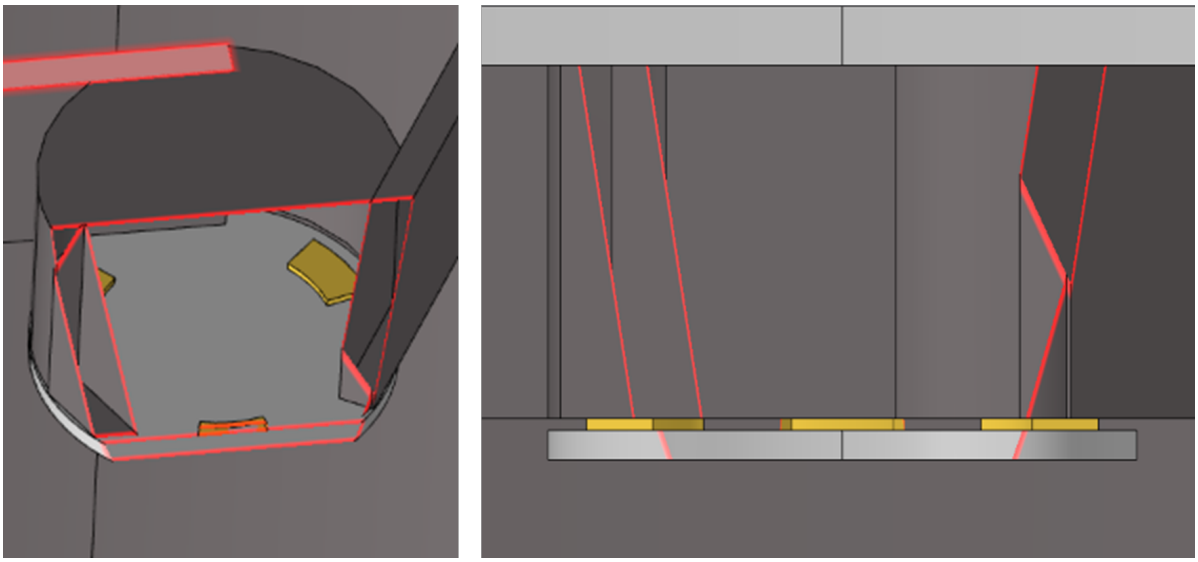

Figure 6.13: Modeled adhesive spot configuration for the M2, showing their placement between the M2 support and the spider cylinder.

For the primary mirror, the adhesive interface design is even more critical due to its larger size and its dominant contribution to optical stability. The updated model includes discrete adhesive pads between M1 and its supporting structure, as illustrated in Figure 6.14.

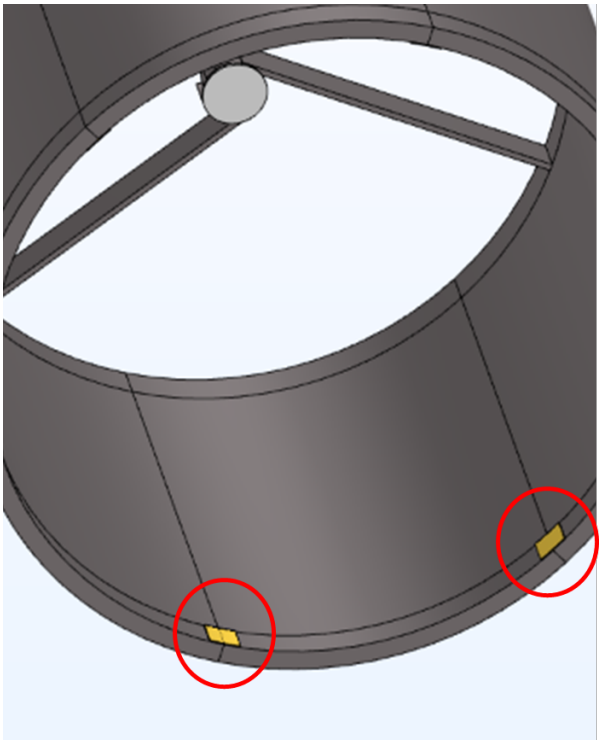

Figure 6.14: Detailed geometry of the adhesive spot interface for the primary mirror, highlighting the adhesive layer between M1 and the supporting structure.

6.2.3. Radial Flexures

In the preliminary model, it was concluded that the flexure design might interfere with the results and cause deformation in an undesirable manner. Hence, the decision was made to reevaluate the geometry. Based on common engineering practice, mass-efficient structures follow the shortest load path.

The structure connects to the bearings and serves other purposes as well, which would make a detailed design out of the scope of this project. Therefore, a simplified approach was chosen by adopting a common solution: connecting the flexures (leaf springs) tangentially to the telescope tube. In this configuration, they only rotate the telescope around the z-direction in the case of a gradient. A first-order estimate of the required dimensions was made based on the adhesive spot size needed to survive the 70 g load.

The flexure design has been changed to a tangential configuration, based on the philosophy that the telescope is axially symmetric. As a result, the expansion of the flexures will primarily cause the telescope to rotate about its axis, minimizing the impact of flexure deformation on the overall telescope deformation.

Logically, three connections would be used; however, given the square volume, a decision regarding the length of the flexures has to be made, as shown in Figure 6.29.

Choosing the connection points with a 30 ° offset to the spider provides both thermal isolation and symmetry. However, if the flexures were to be directly connected to the terminal nacelle, their lengths would be asymmetric, possibly introducing modeling artifacts in the thermal model. Therefore, the decision was made to keep the length consistent with the shortest flexure.

6.2.4. Painting the LCT

The most common strategy to control temperature variations in space systems is to color/paint/coat the outside and inside surfaces of a device. This affects the surface's emissivity and absorptivity constants. Thus changing the emitted and received radiation.

There are many variations of paint, and commonly a lot of combinations are checked. The base design with unaltered surface properties is compared to a painted version where the most common strategy is checked. Most likely the outside of the LCT will be white and the inside of the telescope and surrounding optical structure black. The latter helps to decrease stray light and other reflections, such as backscatter. If these are absorbed, they cannot interfere with the signal, or at least the interference is minimized.

The cross-sectional area and length are chosen to keep the conductive connection constant.

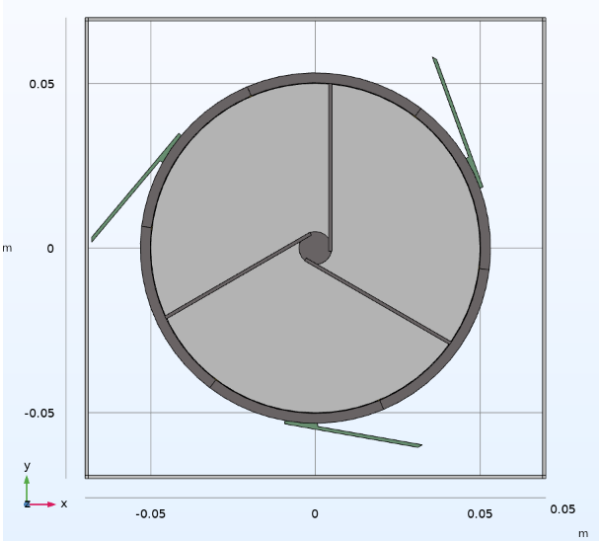

Figure 6.15: Top view of the model including the radial titanium flexures.

6.2.5. Zerodur Mirror

In the preliminary model the choice was made to model the M1 with fused silica properties. Because it is commonly used for many optical parts, and given the lack of a price difference along with the possibility of achieving a 0-CTE design, it is deemed worthwhile to consider Zerodur as an alternative. Given its near 0 CTE and proven use in space-based optical applications. Some of the properties common to Zerodur can be found at [23].

6.3. Resulting Performance Changes

The aforementioned changes are reassessed through the same load cases, and the same material cases are investigated to evaluate the effect of the design update.

But before the whole design is evaluated, consider the effect on the V shape analyzed in section 6.1.1.

The resulting rigid body deformations for loadcase 3 are shown in Figure 6.16. Where clearly there is very little influence w.r.t. the V shape. This result is regarded as additional support for the hypothesis that the effect is caused by the cylinder CTE.

Interestingly, the value of the relative piston results decreases significantly. Which might be attributed to the increased vertical flexure area modeled in the radial design. It is an example of the sensitivity of the results to design changes.

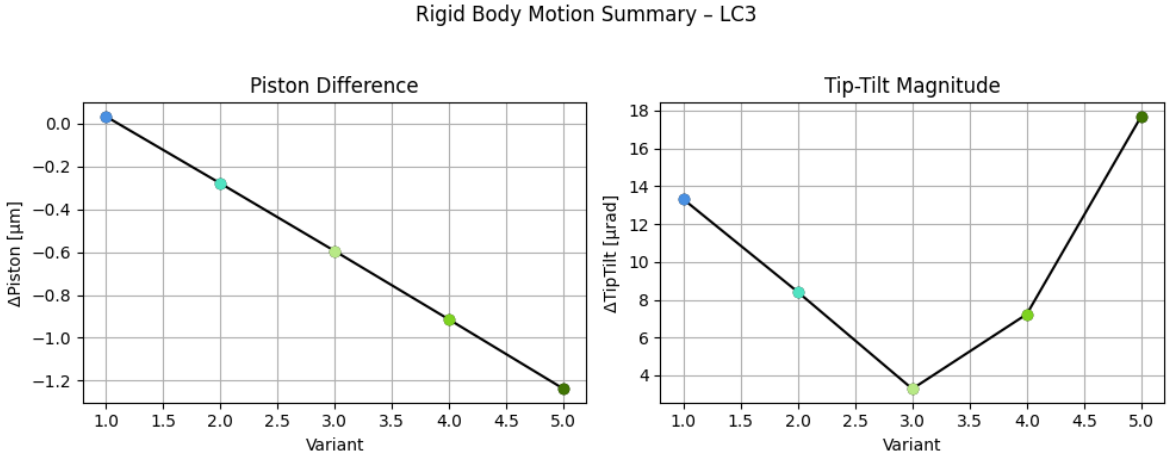

Figure 6.16: The piston and tip tilt results for new radial flexure design.

Figure 6.17 presents the same three operational load cases and their effect on the rigid body motions, comparing the new model (shown in darker colors) with the preliminary model (shown in the original colors). The load cases are still marked with a circle for LC3, a triangle for LC4, and a square for LC5.

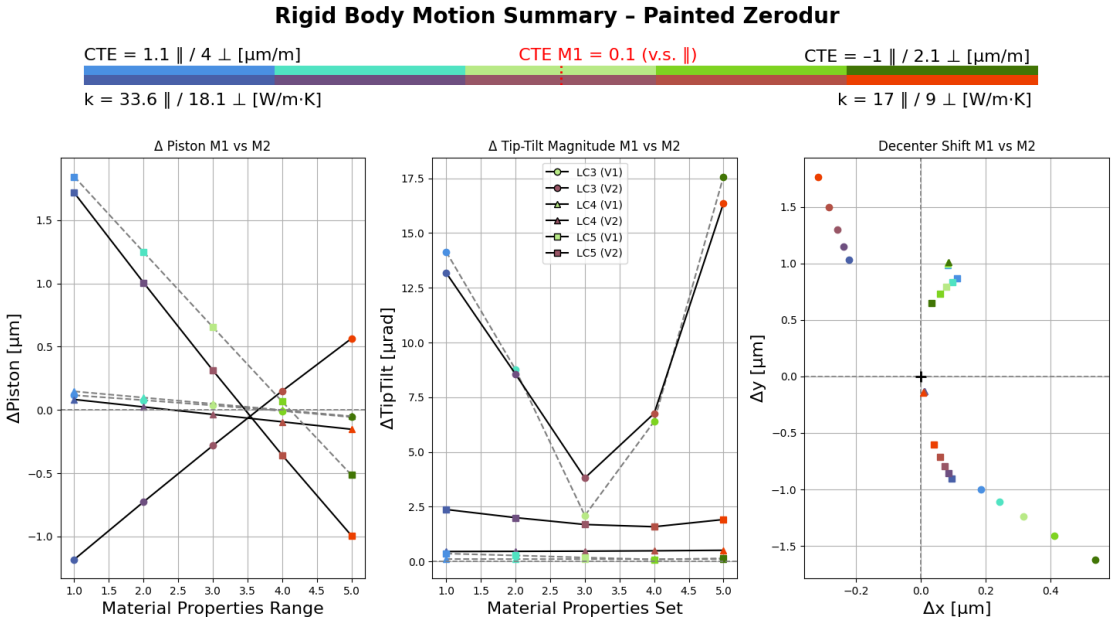

Figure 6.17: In blue to green, the preliminary design results for reference. In dark blue to orange the new design.

In general the order of magnitude of the RBMs has stayed the same with the updated details. This is a good confirmation of the validity of the updates. It re-warrants the interest in the thermo-mechanical properties of the C/C-SiC.

There are, however, some notable shifts—at least one in each type of RBM. Starting with the piston for LC3, its magnitude has increased, and it has flipped around the x-axis, with the value increasing as the CTE decreases. In addition the shift in decenter direction: in LC4, a positive effect is observed, probably due to the flexures no longer interfering. For LC5, the decenter has shifted around the x-axis, which may be related to the reassignment of temperature values on the LCT—these may have swapped positions. The magnitude and direction remain nearly identical, as does the variation between material cases.

Since load case 3 is familiar, the shifts caused by the design update are evaluated by focusing in its results.

6.3.1. The model update performance in temperature gradient

The changes in LC3 due to the model update are shown in isolation in Figure 6.18. Since the tip-tilt change is negligible, the following section covers only the piston and decenter.

Starting with the piston change, the main influence is a temperature drop, as shown in Figure 6.19, where the whole cylinder increases in size due to the negative CTE. Naturally, this starts from a contracted cylinder, since the temperature is mostly below 20 degrees.

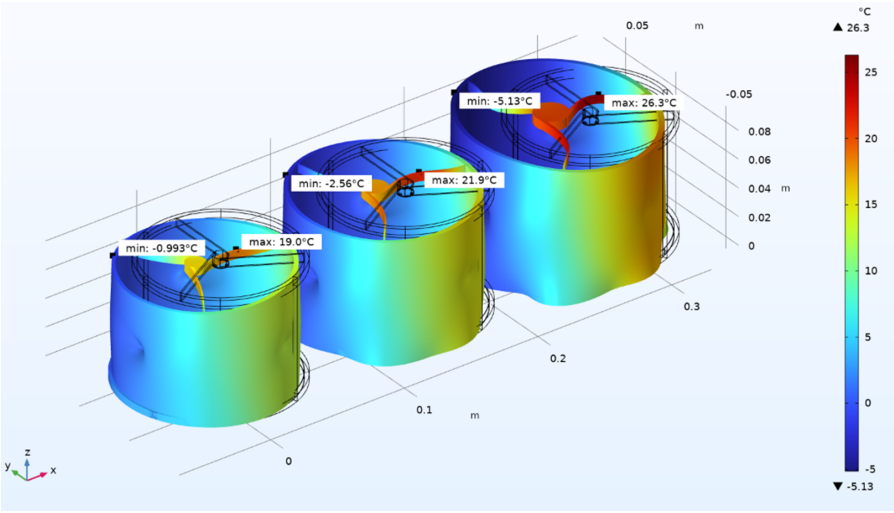

Figure 6.19: An isometric view of material cases 1-3-5 and their temperature and resulting deformation (5000x) for LC 3

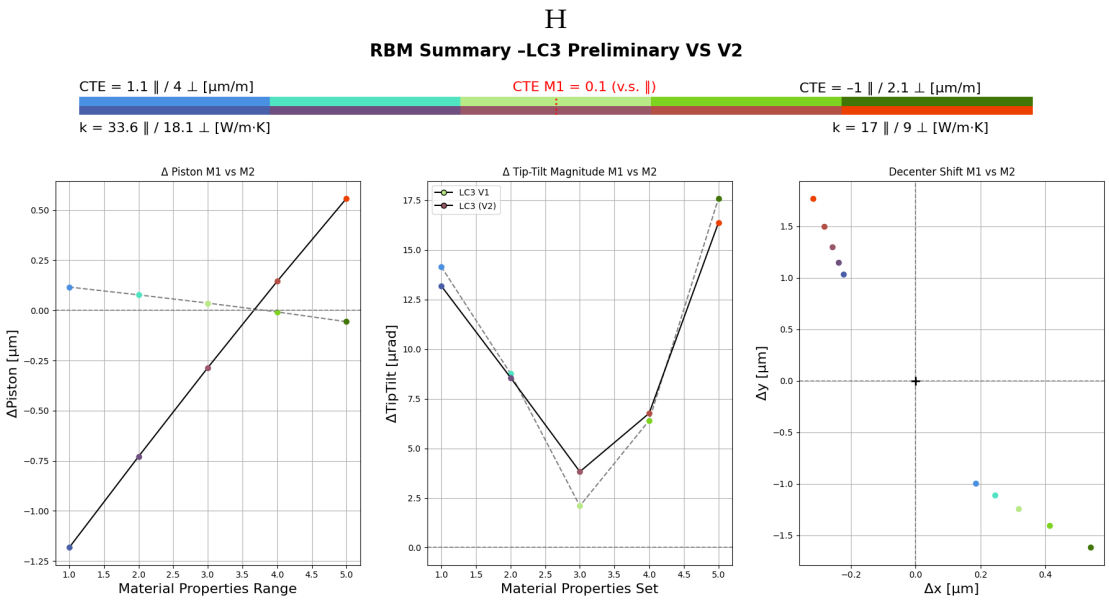

Figure 6.18: RBM summary for LC3 comparing versions 1 and 2.

the paint change, which increases the radiative connection with both the $-30°C$ terminal and outer space, causing the temperature to drop below the reference temperature for most of the structure.

Finally, in the decenter graph, LC3 appears to have been roughly mirrored about a diagonal axis. The magnitude, as well as its increase with decreasing SiC percentage, remains similar. The latter can be explained by considering the top view of the telescope as shown in Figure 6.20 below.

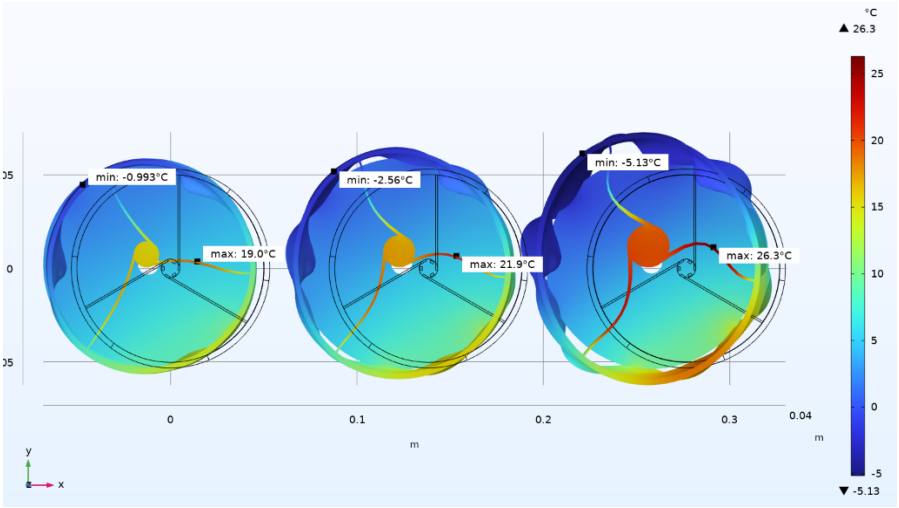

Figure 6.20: Top view of the deformation and temperature for the model update caused by LC 3. The material cases are shown 1-3-5 from left to right

Where the cold side contraction and, the hot side expansion and the wave like deformation pattern increases throughout the material cases and pulls and pushes the secondary mirror support structure in the opposite direction w.r.t. the preliminary model

6.4. Conformance Evaluation of the Second Modele

Considering all values and sensitivities, LC3 remains the most critical case. Assuming full telescope sensitivity for the piston, the logical choice for both piston and tip–tilt is the material set closest to zero CTE. For the decenter shift, however, this choice is less favorable, though still manageable. From the RBM results it is clear that LC3 and LC5 are the driving cases, and for both, material case 3 is the most favorable. The WFEs induced by the RBMs in LC3 and LC5 are therefore reported in Table **??** below.

Table 6.2: RBM induced wavefront error for the worst-case operational LCs, i.e. the gradient and Hot albedo & IR. The residual was calculated based on the 50 nm RMS total WFE requirements

Degree of Freedom (units)	LC3			LC5		
	RBM_S	Sensitivity	nm Mean Squared^2	RBM_S	Sensitivity	nm Mean Squared
Dx	0.25	10.5	6.89	0.08	10.5	0.71
Dy	1.30	10.5	186.32	0.80	10.5	70.56
Dz	0.30	70.5	101.00	0.33	70.5	122.21
Rxy	4.00	1.43	32.83	1.80	1.43	6.65
Sum of squares	–	–	673,36 | **25.95 nm RMS**	–	–	619.17 | **24.88 nm RMS**
Residual surface	$< \sqrt{50^2 - 673.36} = 42.47$**nm RMS**			$< \sqrt{50^2 - 619.17} = 43.37$ **nm RMS**		

Before committing to this set of material properties, the surface deformation in the operational load cases is investigated, as well as the structural integrity in the survival cases (LC1 and LC2). Similar to the RBMs, Figure 6.21 reports the changes in surface deformations (SDs) due to the material cases. From the graphs it is clear that if material case 3 is chosen the surface deformations experienced are well above 50 nm RMS.

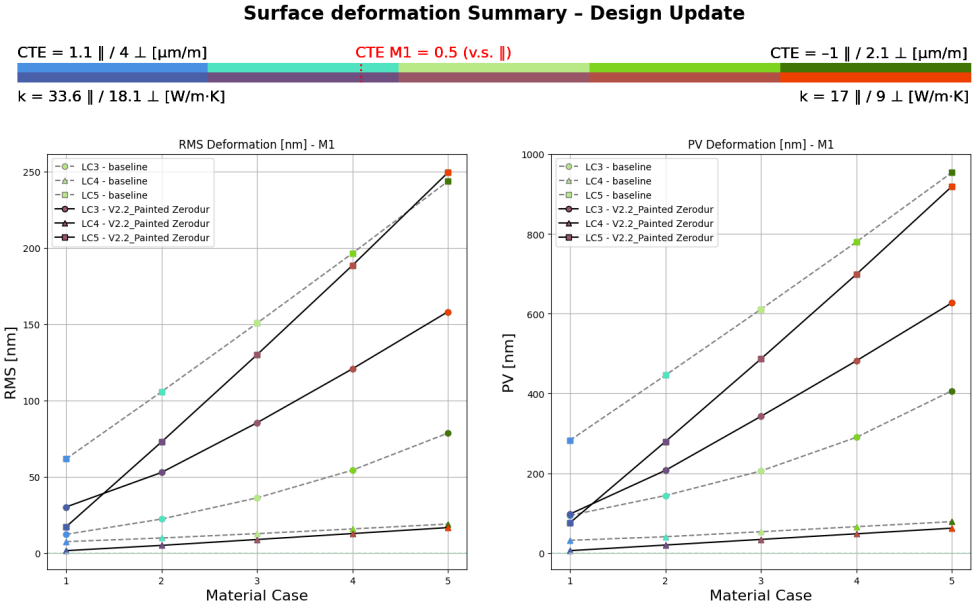

Figure 6.21: The surface deformations for the primary mirror in terms of RMS and peak-to-valley values depending on the different material properties.

Hence the SDs for the driving LCs (3 & 5) are investigated in more detail. The SDs are plotted for a specific material case. Figures 6.22 and 6.23 show that the SDs patterns are dominated by low-order terms, and while the RMS values exceed 50 nm for LC3/LC5, these cannot be directly equated to system-level WFE without STOP analysis as discussed in Chapter 3.

The deformation pattern shows predominantly a focus on the M1 and something akin to bending on the M2.

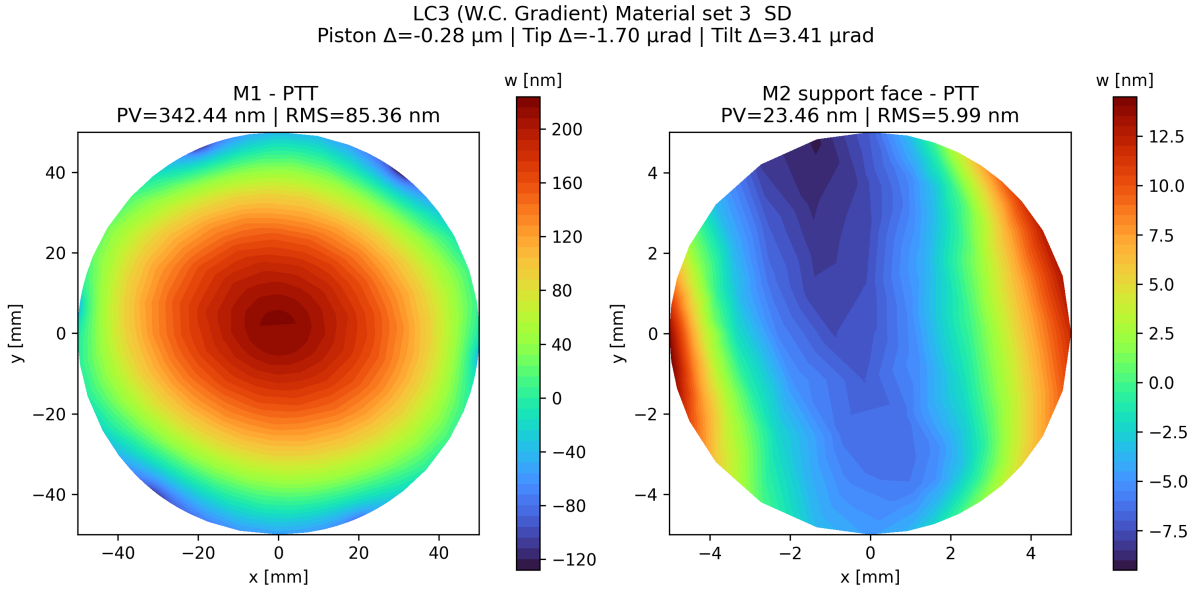

Figure 6.22: Surface deformation pattern for the primary mirror under LC3, shown for a specific material case, highlighting RMS and peak-to-valley variations.

In addition the large focus error in LC5 shown in Figure 6.23 below clearly shows 6 peaks around the perimeter. Which are explained by the locations of the adhesive. Indicating the expansion behavior of the adhesive or the relative expansion between the cylinder and mirror might compress the M1 at these points. Bending it into a focus shape, 1 effect that is not modeled might mitigate this.

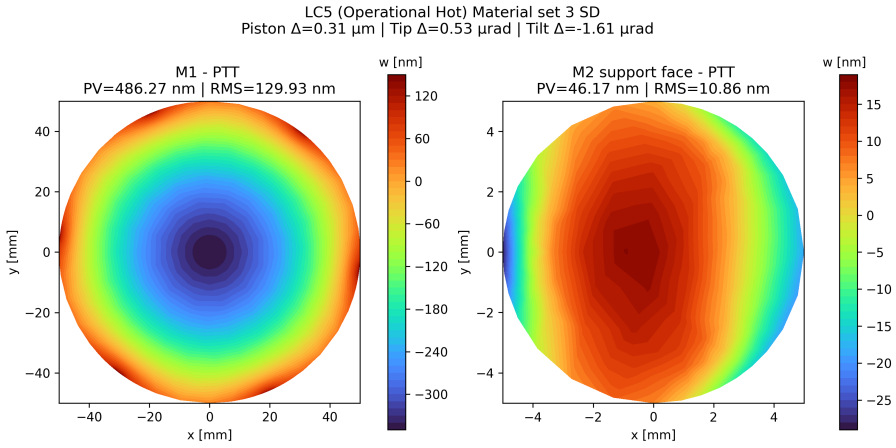

Figure 6.23: Surface deformation pattern for the primary mirror under LC5, shown for the same material case as in Fig. 6.22, allowing a direct comparison of deformation characteristics.

Namely, the epoxy adhesive has a tendency to shrink, meaning in flight it might already be in a negative strain state. Which it would have to overcome before stressing the rest of the parts. However, this contribution is minor.

The surface deformations are significant there are, however, some relatively easy design updates that could solve the problem:

- Making incisions in the cylinder around the adhesive connection to remove stiffness allowing the mirror the expand without getting stressed. Decreasing both the loading in LC1 and 2 as well decreasing the deformation.
- Decreasing the adhesive layer thickness, which would decrease the amount of expansion of the adhesive decreasing the load as well.

The former would come at the cost of stress concentrations and cutting fiber paths. Both are decreasing the strength so there should be a margin if that path is taken. The influence of the adhesive patch is remarkable. Hence, the influence of the adhesive thickness is reviewed in LC3.

The V2 model M1 and cylinder connection is made by a conservatively chosen 200 μm thick patch. But nominally, if the tolerances of a design are met, a 150 μm thickness should be feasible. Using the parametric setup of the model the adhesive thickness for all patches can be changed with the click of a button. Resulting in the following change in RBMs for load case 3 shown in Figure 6.24.

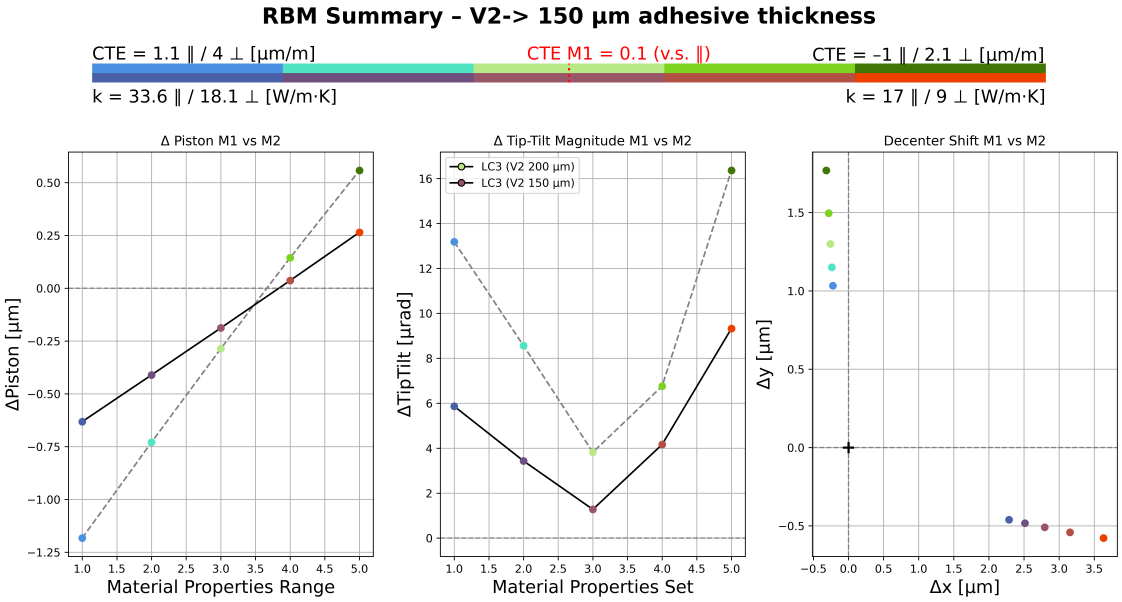

Figure 6.24: Showing the change in RBMs for LC3 due to changing the adhesive thickness layer to 150 μm.

Given these considerations, the following sections evaluate the strength of the design under the relevant load cases.

6.5. Survival load cases

Thermo-mechanical strength checks for all material cases (Tab. 6.3) confirm that peak von Mises stresses in the mirrors are well below the respective yield limits. For all material cases the maximum in plane shear stress in the local axis system for the C/C-SiC is 5 MPa. It is found in MC5 at the adhesive connection with the M1. The maximum structural stress under LC1 is 34.86 MPa, corresponding to ~ 15% of the assumed 230 MPa felxural yield strength for C/C-SiC, and mirror stresses remain below 10 MPa. Under LC2, the same case reaches 23.03 MPa in the structure and 6.081 MPa in the mirrors, which is similarly within safe bounds. LC3 loads produce even lower stresses, indicating structural risk within the set limits.

Table 6.3: Maximum stresses for mirrors for three load cases (LC1, LC2, LC3) with decreasing SiC %.

Material case (↓ SiC %)	LC1 mirrors [MPa]	LC2 mirrors [MPa]	LC3 mirrors [MPa]
Case 1	9.394	4.105 (M2)	1.426
Case 2	9.482	4.678	1.856
Case 3	9.595	6.081	2.494
Case 4	10.49 (M1)	7.525	3.197
Case 5	12.49 (M1)	9.024	3.995

The maximum stress located in the temperature survival load cases are found in the flexure cylinder interface. Shown in Figure 6.25. The interface is a direct solid connection between the Flexure and the cylinder hence the CTE difference between the titanium and C/C-SiC is most likely the cause.

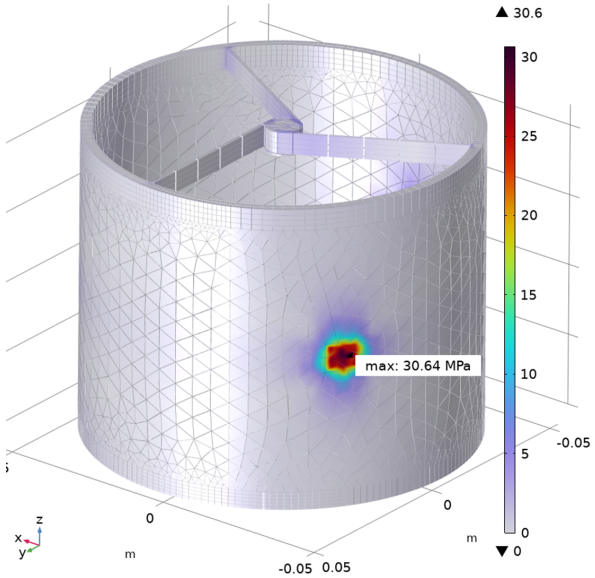

Figure 6.25: The maximum thermo mechanical stress location within the model for Material case 1 in LC1 is located at the flexure interface. Note the other 3 flexure interfaces are similarly stressed.

6.5.1. Structural evaluation of the Model Updates

For the given telescope mass (270 grams), the corresponding quasi-static limit loads are derived by linear interpolation of the curve breakpoints (Tab. 6.4), and applied independently in each principal axis directions. This approach envelopes the low-frequency launch environment and is consistent with the preliminary design phase, where the specific launch vehicle is not yet defined. The loads are implemented as static accelerations in the FEA model, and the resulting adhesive and structural stresses are evaluated.

Table 6.4: MAC design limit loads for relevant mass range, adapted from [31].

Mass [kg]	Limit Load [g]	Interpolated Load [g]
1	68.0	
5	49.0	70.0
10	39.8	

Quasi-static 70 g load simulations (Tab. 6.5) further implicate the safety margin. Adhesive layer stresses are far below the 20 MPa shear allowable established in Chapter 5, with the highest being 2.414 MPa. These results demonstrate that even with adhesive modeling at 200 μm bond-line thickness, the design retains large safety factors against both structural and adhesive failure.

Although the 83.38 MPa M1 mises stress result in the table below is below the allowable yield for Zerodur (100 MPa) as reported in Table 5.4. Leaving a roughly 20 % margin is quite low. Considering the stage in the design process, the actual loading conditions are not fully represented by the MAC curve load. This warrants further investigation.

Table 6.5: Maximum stresses for 70 g load directions in x, y, z order, including adhesive stresses for the same directions.

Direction (70 g)	**Mises max in adhesive** $[MPa]$	**Mises max in whole model**$[MPa]$
x	2.414	70.89(M1)
y	2.281	83.38(M1)
z	1.455	24.19(M1)

The maximum stress found in M1 is located at the back side of the mirror near the adhesive connection. When the mesh is examined on the single element level as shown in Figure 6.26 it is clear that the effect is quite local. The thin element shape is non desirable and in can cause the very large gradient in stress found over the singular element. Which would argue for the high value to be a numerical artifact instead of a real to be expected stress.

In either case the adhesive connection between the cylinder and the primary mirror is of the upmost importance. This is to be expected but also reconfirmed through the MAC load case and the thermo-mechanical results from LC1-5.

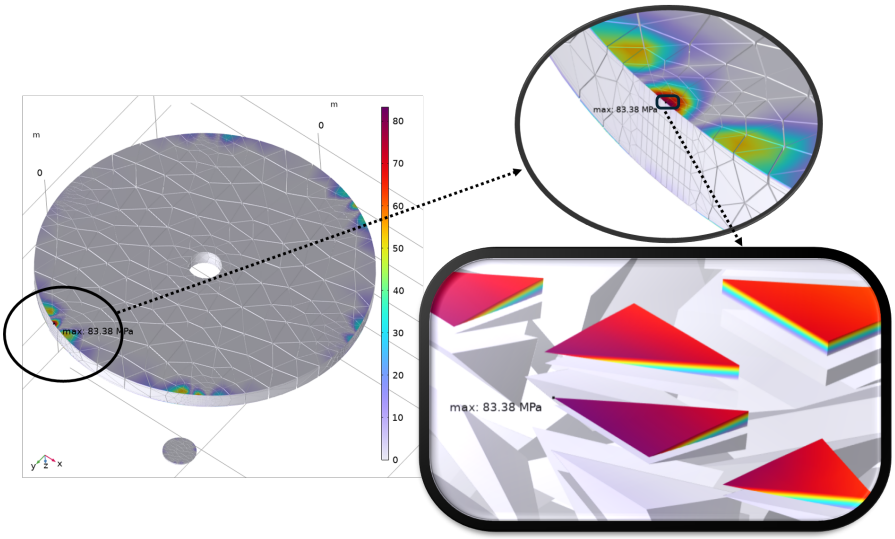

Figure 6.26: The group of tetrahedral elements in which the maximum stress is found in the acceleration load cases. Depicted for the 70g y direction load

Given that LC3 RBM sensitivity is the primary driver for material choice, and that the thermo-mechanical and g-load strength checks for Case 3 are satisfactory, the recommended target for the $\phi = 100$ mm telescope is a C/C-SiC with *near-zero in-plane CTE* (approximately +0.1 μm/mK) and mid-range anisotropic conductivity ($k_{\parallel} \approx 25.3$ W/mK, $k_{\perp} \approx 13.6$ W/mK). This property set offers the optimal balance: minimal LC3 piston/tip-tilt, manageable decenter, acceptable surface deformation in LC1/LC2, and large strength margins for both operational and launch-like load cases.

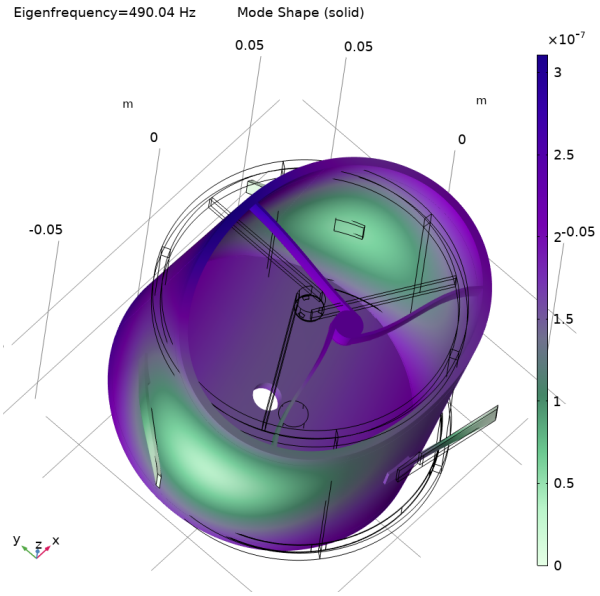

Figure 6.27: First mode shape of the structure at 490 Hz, illustrating the primary deformation pattern.

The first mode shape corresponds to a global deformation mode with a frequency of 490 Hz, which is relatively high. This indicates a structurally stiff configuration with considerable margin above typical launch vibration excitation frequencies. Such a high first eigenfrequency reduces the risk of dynamic amplification during launch. It should be noted, however, that the result is strongly influenced by the applied boundary conditions, and the modeled flexures are only partially representative of the final configuration. In addition to the high specific stiffness of C/C-SiC, the low-weight design and the relatively large 3 mm wall thickness are also key drivers for achieving a high f_1.

6.6. Mesh Convergence

Using the model and the manner in which it was set up, the following section reports the assessment of its accuracy. As in the previous chapter, the gradient load case (LC3) is used to assess the accuracy and limitations of the model. A mesh convergence

study is presented to evaluate whether the results are sensitive to element size.

To evaluate discretization error within the model and ensure convergence, a mesh convergence study was performed. The study focuses on verifying the most important result. Commonly, displacement and temperature results are relatively insensitive to element size and shape, whereas stress results are not. This acknowledgement guides the scope of the activities reported in this chapter. Since resources are limited, the main results—namely the rigid body motions—are evaluated.

6.6.1. Mesh Generation

There are multiple algorithms by which a mesh can be generated. A user-friendly method is the automatic tetrahedral option, since its element shape allows the mesh to fit most geometries easily. However, this reduces control over specific parts. In the case of the telescope, both the mirrors and adhesive patches are relatively thin compared to their surface area. To properly capture their deformation behavior, a common rule of thumb is to have at least two elements through the thickness. An element's ability to capture the behavior depends on the solution and also on the element type.

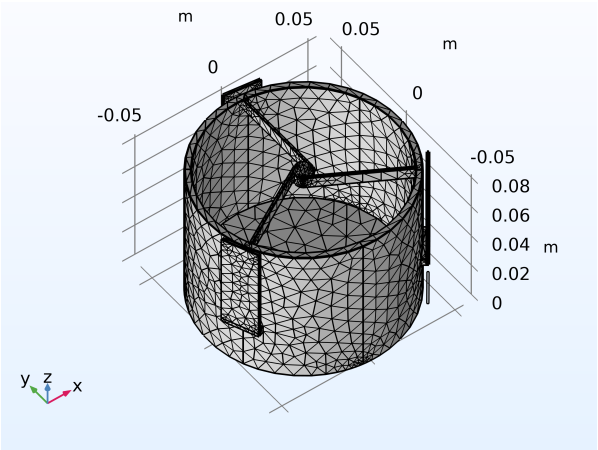

Figure 6.28: Mesh applied to the preliminary model covered in Chapter 5, used in the solid mechanics analysis.

For this reason, the parts of interest and concern are meshed in a controlled manner. This also allows a single scaling parameter to be added to the generation algorithm, which scales the number of elements in the parts. For example, the boundary layer can be used to force extra elements around the adhesive patches.

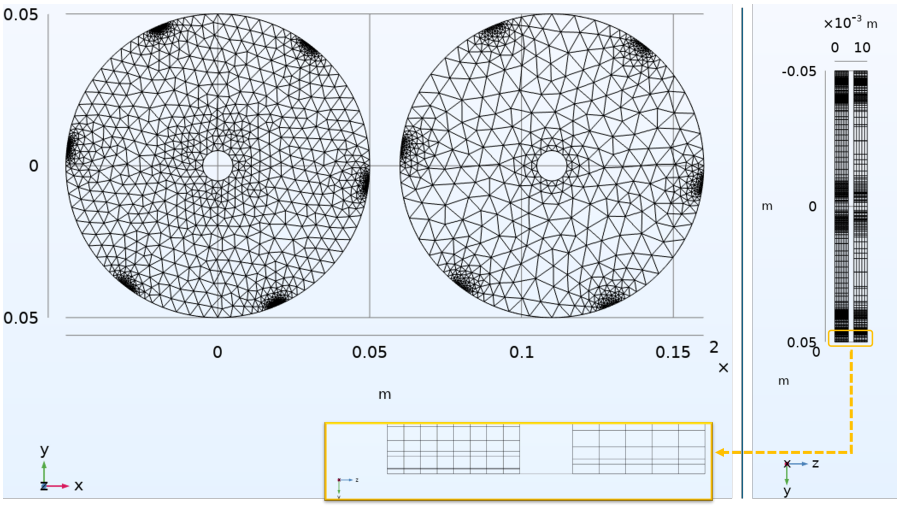

Figure 6.29: Top view (left) and side view (right) of the primary mirror mesh with scaling parameters 60% and 100%, resulting in a three-element difference through the thickness.

A similar approach is taken for all parts, where extra care is taken in the adhesive patches and mirrors as well as near the flexures. Conversely, the same methods can be used to limit the size of the mesh in places where there is less interest. For example, in the terminal nacelle, the faces are partitioned so that the surfaces use a limited number of elements. Before showing the three scaled meshes used for the subsequent step, Table 6.6 reports the meshing parameters used and how they are scaled.

Table 6.6: Meshing parameters with their scaling expressions, default values, and roles in the model.

Parameter	Expression	Default Value	Description
`tt`	$\text{round}\left(\frac{2}{M_{\text{scaling}}}\right)$	2	Through-thickness elements ($V_0 = 2$)
`Arc`	$\text{round}\left(\frac{20}{M_{\text{scaling}}}\right)$	20	Arc elements ($V_0 = 20$)
`edge_a`	$\text{round}\left(\frac{5}{M_{\text{scaling}}}\right)$	5	Adhesive pads ($V_0 = 5$)
`n_b`	$\text{round}\left(\frac{2}{M_{\text{scaling}}}\right)$	2	Boundary layers ($V_0 = 2$)

The number of elements is, an integer; there are no half elements. Hence, rounding is used, and the rest is scaled from the baseline mesh. These parameters are used to set distribution settings in the meshing algorithms to enforce the number of elements and how they grow throughout the model. Most parts of interest are either meshed with a quadrilateral or boundary-layer mesh on the surface and then mapped through the thickness. The resulting meshes for scaling parameters of 100%, 80%, and 60% are shown in Figure 6.30, with, respectively, 34k, 56k, and 80k elements.

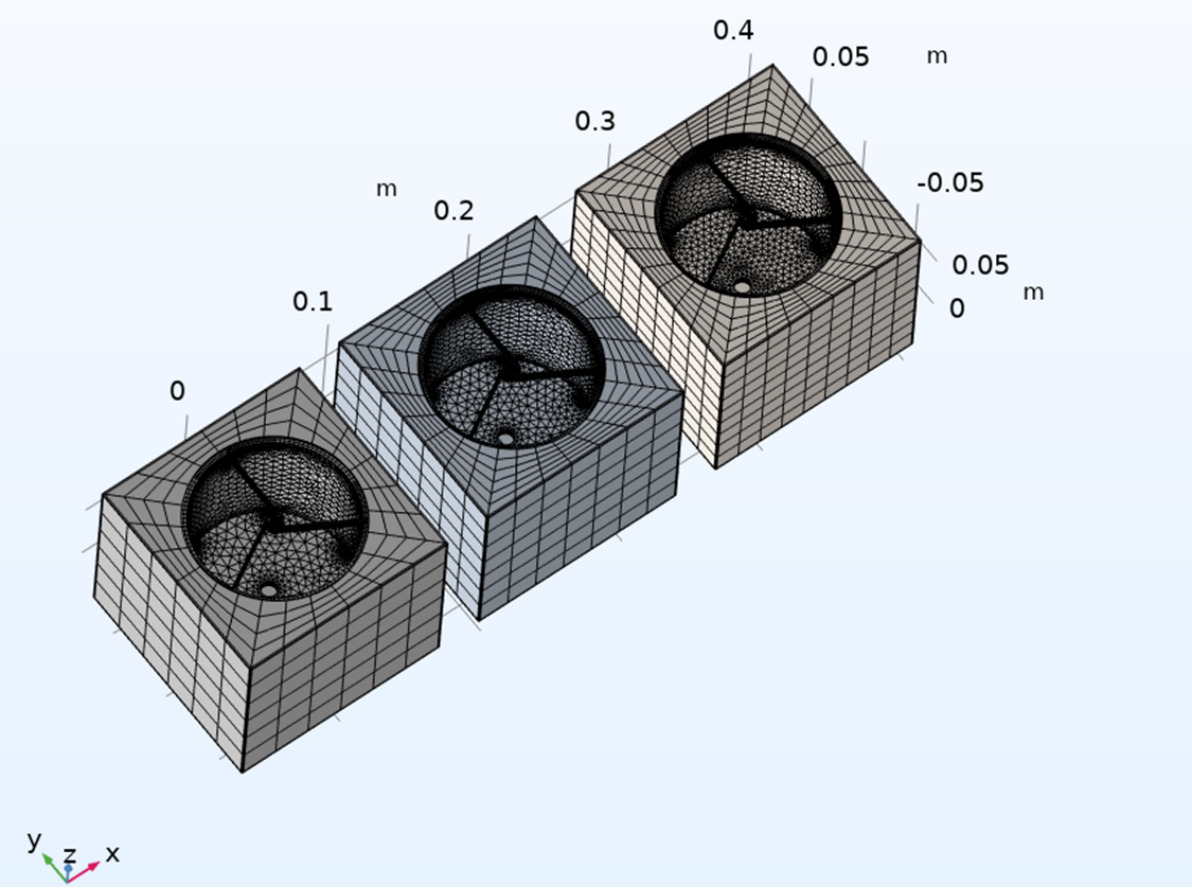

Figure 6.30: Meshes for scaling parameters of 100%, 80%, and 60%.

The number of elements does not scale exactly equally across the whole model. For example, from 100% to 60%, the element count in M1 increases from roughly 7k to 19k, and in the adhesive patch between M1 and the C/C-SiC tube from roughly 100 to 400 elements.

For M1, on average, the element size changes from 5,5 mm3 to 2 mm3, whereas for the adhesive patch the change is from 0,05 to 0,013 mm3.

Finally, COMSOL provides several internal mesh-quality measures that enable a preliminary analysis and flag areas of concern. For example, as plotted in Figure 6.31 below, the maximum angle of the individual elements can be used as a quality metric. A large maximum angle indicates element distortion, which degrades the interpolation of the solution field and can reduce the accuracy of the results.

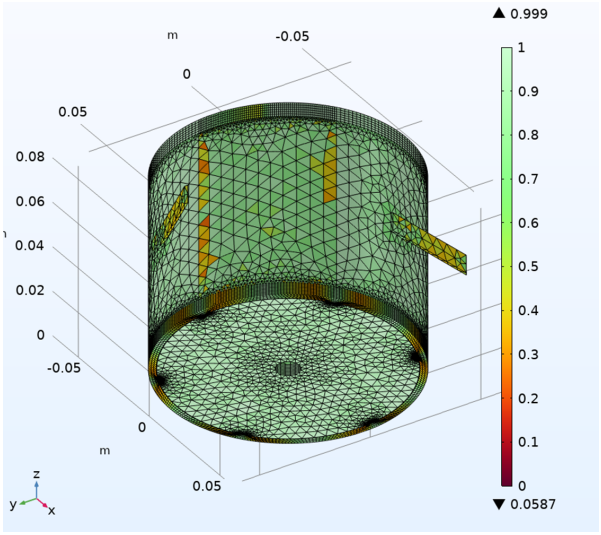

Figure 6.31: Mesh quality plot generated in COMSOL, using the maximum element angle as the quality criterion.

As expected, larger-angle elements are found near boundaries of parts of the model due to increases in size or changes in direction. These are areas to treat with extra care—for example, the transition from the adhesive patch through the C/C-SiC tube. However, evaluating M1, M2, and the M1 patches in detail shows a generally high-quality mesh in terms of maximum angle.

6.6.2. Mesh convergence of RBM results

To evaluate the sensitivity of the predicted rigid-body motions (RBMs) to mesh density, a convergence study was performed using three systematically refined meshes ($M = 06, 08, 10$). The gradient load case (LC3) was used for this assessment.

In classical mesh convergence studies, the apparent order of accuracy p is often estimated using the Richardson extrapolation relation

$$p = \frac{\ln\left(\frac{Q_3 - Q_2}{Q_2 - Q_1}\right)}{\ln(r_{21})}, \tag{6.1}$$

Where Q_i are the results on successively refined meshes. However, this approach assumes that the sequence Q_3, Q_2, Q_1 is strictly monotonic. In the present case, the RBM values change only slightly between meshes. As a result, sign changes occur between successive differences, leading to oscillatory behavior. This makes the ratio $\frac{Q_3 - Q_2}{Q_2 - Q_1}$ negative or near zero and thus p becomes undefined. For this reason, order-of-accuracy estimates are not meaningful here, and convergence is instead evaluated using absolute tolerances.

Absolute convergence tolerances are defined from the system error budget. Let B be the allowable optical error (for example 50 nm RMS), and s_i the sensitivity of this error to RBM component i. Allocating a fraction η of this budget to numerical discretization gives the allowable mesh-discretization error

$$\tau_i = \frac{\eta B}{s_i}. \tag{6.2}$$

Convergence is accepted if the absolute change between the fine and medium mesh results satisfies

$$\Delta_i = |Q_{h_1} - Q_{h_2}| \leq \tau_i \qquad \forall i. \tag{6.3}$$

The RBM results for LC3 are listed in Table 6.7, together with the absolute changes Δ between subsequent mesh refinements.

Table 6.7: Rigid-body motion results for LC3 and MC3 across three mesh densities, with absolute differences Δ between mesh levels.

	Piston [μm]		Tip [μrad]		Tilt [μrad]		Dec$_x$ [μm]		Dec$_y$ [μm]	
Mesh	Q	Δ	Q	Δ	Q	Δ	Q	Δ	Q	Δ
$M = 10$	−0.289		−1.863		3.101		−0.270		1.283	
$M = 08$	−0.289	0.000	−1.740	0.123	3.224	0.123	−0.242	0.028	1.275	0.008
$M = 06$	−0.293	0.004	−1.803	0.063	3.036	0.188	−0.263	0.021	1.306	0.031

The maximum observed differences between the fine and medium meshes are

$$\max|\Delta\text{tip}| = 0.123\ \mu\text{rad}, \qquad \max|\Delta\text{decenter}| = 0.028\ \mu\text{m}.$$

Assuming tolerances of $\tau_{\text{tip}} = 5\ \mu$rad and $\tau_{\text{decenter}} = 1\ \mu$m, these correspond to only

$$\frac{0.123}{5} \times 100\% \approx 2.5\%, \qquad \frac{0.028}{1} \times 100\% \approx 2.8\%.$$

Thus, the RBM results are considered mesh-converged, with the mesh discretization contributing less than 3% of the allowable RBM error budget.

6.6.3. Mesh Update Resolves Stress Concentrations

The mesh was updated using the algorithmic tools described at the beginning of this chapter, allowing a reassessment of the result shown in 6.26. The working hypothesis is that high element skewness led to an overestimation of the interpolated stress in that region. After remeshing, the local peak disappears and the stresses vary smoothly across elements, indicating that the previous hotspot was a numerical artifact rather than a true structural response.

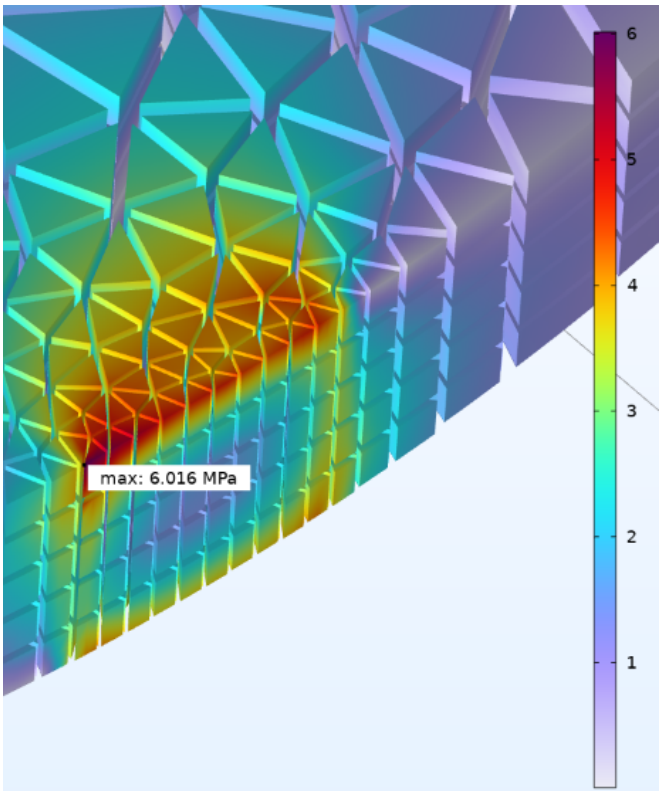

Figure 6.32: Backside of M1 for the 70 g y-direction load after the mesh update, showing a maximum von Mises stress of 6 MPa (previously 83 MPa).

This updated result (Fig. 6.32) supports the conclusion that element quality—particularly skewness—can inflate peak stresses when results are interpolated over distorted elements. The analyses for version 2 chapter use the updated mesh to avoid such artifacts. In addition, for the xyz 70g load cases, the maximum stress in the mirror equals that shown in the figure. It is no longer near the critically high level reported previously, supporting the model's mechanical soundness.

7

Conclusion

This research examined the thermo-elastic behaviour of carbon–carbon silicon carbide (C/C–SiC) for potential application in a laser communication terminal (LCT), focusing on a ⌀100 mm diameter telescope structure operating in low Earth orbit (LEO) at altitudes of 500–2000 km. A parametric finite element analysis (FEA) model was developed in COMSOL Multiphysics, coupling radiative and conductive heat transfer models with the solid mechanics module. A Zernike-based Python post-processing pipeline was implemented to extract rigid body motions (RBMs) and surface form errors from the optical surfaces.

A modelling framework adapted from [8] enabled systematic evaluation of worst-case hot, worst-case cold, and operational thermal gradients from solar, infrared, and albedo radiation. Parametric studies were facilitated by the flexible model setup, allowing investigation of the design's sensitivity to material properties.

This analysis focused on two C/C-SiC parameters: coefficient of thermal expansion (CTE) and thermal conductivity. Which have been shown to be tunable based on the SiC volume % by [19, 20]. In layman's terms, a higher SiC percentage results in properties that more closely resemble pure SiC, with in-plane CTE values tunable from $17\ to\ 33\ \mu m/mK$, for SiC contents of respecitvely 15 to 40 %.

The final model showed that when the planar CTE is tuned between 0.1 and 0.5 μm/mK, corresponding to approximately 25–30 % SiC (vol.) in a ±90° layup. The rigid body motion-induced WFE error is well within the, $\lambda/30 \approx 50\ nm\ RMS$ budget. Namely, 25 & 26 $nm\ RMS$ for the most demanding load cases. Leaving a minimum 42 $nm\ RMS$ for other thermo-mechanically induced effects that were not accounted for or were out of scope.

Furthermore, the adhesive connections between the mirrors and the structure are critical, as they significantly influence deformation behavior. This effect is minimized and mitigated with the chosen material parameters. The 105 mm diameter M1 design remains well within material stress limits while avoiding the need for a sun filter at the aperture and potentially even the need for focal correction. This tolerance for large gradients and temperature ranges could greatly benefit the researched application, given the variety of orbits and satellite platforms on which it must perform. The project thus addressed the central research question:

Can a ⌀100 mm telescope structure made from C/C-SiC be used to maintain a wavefront error within acceptable limits under representative LEO thermal load cases for laser communication applications?

Based on the thermo-mechanical modelling, the answer is affirmative. When the in-plane CTE is tuned close to zero, the resulting RBMs and surface form errors remain within the performance limits defined for the Cassegrain telescope design. Providing a first step in ensuring that the total induced wavefront error does not exceed the allowable thresholds for laser communication applications. This conclusion holds for the evaluated steady-state thermal load cases, with margins to account for manufacturing tolerances both in terms of geometric accuracy as well as the exact property range required.

From a production perspective, the answer to the research question is negative. The report focuses on model-based work but the thesis project also served a supporting role to the CASTT project, in which challenges related to delamination during production and cleanliness remain unresolved. Work toward these goals is ongoing, but at the time of writing, the state of progress is insufficient for the laser communication use case.

Regarding the use case, C/C-SiC could in theory offer significant improvements, particularly with an optical design that is less sensitive to thermal gradients. However, achieving this effectively would require more than the telescope alone. Given current production capabilities, the necessary resources and effort would be substantial. Combined with the competitiveness of the laser satcom market, where reducing the cost per terminal is the current focus, this makes for a poor fit.

Alternatively, other use cases may offer a more viable path, as the effort required to achieve consistent manufacturing can be more readily justified when increased performance is the primary driver.

8

Recommendations

For Material Development and Quality Assurance at Arceon

In Appendix B, a first rudimentary cleanliness assessment method has been suggested, based on tape-lift sampling as described in ECSS-Q-ST-70-50C. This is complemented with background information on the mechanisms by which contamination affects system performance, the main sources of contamination, and mitigation and verification techniques. These include rinsing, witness samples, visual inspection, airborne monitoring, and thermal vacuum testing for outgassing.

For follow-up projects, it is recommended to focus on developing and validating a bake-out procedure as the logical next step. A measurement plan should be incorporated into the relevant stages of the process chain, at minimum:

- after rinsing at Arceon, following a documented ultrasonic cleaning procedure;
- upon opening a shipped package, supported by a documented packaging procedure;
- during and/or after bake-out, to verify particle and molecular contamination reduction.

Depending on the product geometry and surface roughness, surface cleanliness verification can be performed either by tape-lift testing or by rinse sampling. Bake-out effectiveness should additionally be supported by monitoring Total Mass Loss (TML) and Collected Volatile Condensable Material (CVCM) in accordance with ECSS-Q-ST-70-02C. Using a structure with a similar size as the application in mind.

These measures together may provide a practical path to raising the cleanliness maturity of C/C-SiC parts and enable suppliers, such as Arceon, to align their processes with the stringent requirements of contamination-sensitive space optics applications.

Regarding material characterisations

- The optical properties of C/C-SiC for the machined, non-machined, and (non-)mould faces are required in detail over the temperature range of interest for low-CTE, thermally sensitive applications.
- Correlation of the expected mechanical properties at large structure size in a vibration test.
- Studying the thermo-mechanical properties and correlating them with the CT scans.
- Keep improving the toolbox to enable more complex structures. The added benefit of a near-zero CTE is only unlocked in its full potential if a CTE-matched optical backbone can be enabled. The sandwich structures being developed are a very logical course of action to fulfil this.

For Future Use of the Thermo-Elastic Workflow and Continuation of the COMSOL Model

For additional verification and to apply the analysis to following iterations, extend the analysis to include a preliminary transient based on [51]. The challenge remains to find the balance between the off-the-shelf aim of the LCT and being overly conservative, but verifying the temperature fields from the current steady-state load cases would add value to the current results.

Another addition would be a more direct connection to the optical performance, for example through a STOP analysis. One of the main assumptions taken in the quantification of the RBM limitations and adherence to the requirements is the orthogonal nature of the induced WFE, which in the real system might not be the case: depending on the thermo-mechanical behaviour, some of the WFEs are likely to interact. Doing this would help ensure the current design is as far in spec as it is for the rigid-body motions.

Use the model for preliminary analysis of a TVC test, with a limited amount of work, mainly setting up the thermal loading for the testing campaign. The model can be easily adapted to the test-object geometry, enabling at the very least an additional preliminary prediction of the behaviour of the tube within the TVC. With some extra work, additional features could be added to support the testing campaign, for example by providing an estimate of the deformation and temperature during the test.

Regarding the use cases

As mentioned in the conclusion, the current development path for C/C-SiC does not fit as well. The resources required to finish the development phase for this application do not justify the added performance increase, in part because a development route with an optical design philosophy has already been chosen, and the expectation is that it will meet its aims based on current developments.

That said, there are still clear trends in the extreme use cases, e.g., in both ground and space astronomy. Euclid, Gaia, and Ariel were already mentioned, but LISA, being in part developed at TNO, is another example. An overview of designs using the near-zero-CTE material Zerodur can be found in [60].

Combining the developments made in the CASTT project with the developments in 3D zero-CTE sandwich structures [55, 61], especially the successful in-situ joining of multiple components at a larger scale, makes for significant steps towards near-zero-CTE support structures. Given the already available optical parts and the great interest in near-zero-CTE designs, it should be an avenue to keep exploring.

Bibliography

[1] Fred Kamphues. Gaia BAM flat folding mirrors, November 2008.

[2] Xiaomeng Fan and Xiaowei Yin. Progress in research and development on matrix modification of continuous fiber-reinforced silicon carbide matrix composites. *Advanced Composites and Hybrid Materials*, 1(4):685–695, December 2018. Company: Springer Distributor: Springer Institution: Springer Label: Springer Number: 4 Publisher: Springer International Publishing.

[3] Hemani Kaushal and Georges Kaddoum. Optical Communication in Space: Challenges and Mitigation Techniques. *IEEE Communications Surveys & Tutorials*, 19(1):57–96, 2017. Conference Name: IEEE Communications Surveys & Tutorials.

[4] Jan de Vreugd; Bjorn Nijland; Rene Hazelebach. Design definition of a C/C-SiC telescope structure, September 2024.

[5] Bernhard Heidenreich. C/SiC and C/C-SiC Composites. In *Ceramic Matrix Composites*, pages 147–216. John Wiley & Sons, Ltd, 2014. Section: 6 _eprint: https://onlinelibrary.wiley.com/doi/pdf/10.1002/9781118832998.ch6.

[6] Vladimir Sacek. Telescope optical aberrations, July 2016.

[7] Georg Wiedermann, W Gockel, Stefan Winkler, J Rieber, B Kraft, and D Reggio. *THE SENTINEL-2 SATELLITE ATTITUDE CONTROL SYSTEM - CHALLENGES AND SOLUTIONS*. June 2014.

[8] Mario Badás, Pierre Piron, Jasper Bouwmeester, Jérôme Loicq, Hans Kuiper, and Eberhard Gill. Opto-thermo-mechanical phenomena in satellite free-space optical communications: survey and challenges. *Optical Engineering*, 63(4):041206, October 2023. Publisher: SPIE.

[9] ninguem. Using Blender to learn the basics of Adaptive Optics (part I / II) – /dev/.mind, June 2021.

[10] H. Sanusi and Jan Plessis. *Epoch Time Assisted Orbit Determination for Near Equatorial Low Earth Orbiting Satellites*. December 2002.

[11] Junlan Li, Shaoze Yan, and Renyu Cai. Thermal analysis of composite solar array subjected to space heat flux. *Aerospace Science and Technology*, 27(1):84–94, June 2013.

[12] W. Krenkel. Carbon Fibre Reinforced Silicon Carbide Composites (C/SiC, C/C-SiC). In *Handbook of ceramic composites*, pages 117–149. 2005.

[13] Yochanan Kushnir. Radiative Balance and the Natural Greenhouse Effect.

[14] Introduction to Computing Radiative Heat Exchange.

[15] Jens Nieke, Laurent Despoisse, Antonio Gabriele, Heidrun Weber, Helene Strese, Nafiseh Ghasemi, Ferran Gascon, Kevin Alonso, Valentina Boccia, Bogdana Tsonevska, Pierre Choukroun, Giuseppe Ottavianelli, and Marco Celesti. The copernicus hyperspectral imaging mission for the environment (CHIME): an overview of its mission, system and planning status. In *Sensors, Systems, and Next-Generation Satellites XXVII*, volume 12729, pages 21–40. SPIE, October 2023.

[16] T. Beck, C. Broeg, A. Fortier, V. Cessa, L. Malvasio, D. Piazza, W. Benz, N. Thomas, D. Magrin, V. Viotto, M. Bergomi, R. Ragazzoni, I. Pagano, G. Peter, M. Buder, J. Y. Plesseria, M. Steller, R. Ottensamer, D. Ehrenreich, C. Van Damme, K. Isaak, F. Ratti, N. Rando, and I. Ngan. CHEOPS: status summary of the instrument development. In *Space Telescopes and Instrumentation 2016: Optical, Infrared, and Millimeter Wave*, volume 9904, pages 751–766. SPIE, July 2016.

[17] Ivo Wevers. Outgassing of Technical Polymers PEEK, Kapton, Vespel & Mylar, 2021.

[18] D.M. Tanner, J.A. Walraven, K. Helgesen, L.W. Irwin, F. Brown, N.F. Smith, and N. Masters. MEMS reliability in shock environments. In *2000 IEEE International Reliability Physics Symposium Proceedings. 38th Annual (Cat. No.00CH37059)*, pages 129–138, San Jose, CA, USA, 2000. IEEE.

[19] A. Schöppach and T. Petasch; B. Heidenreich; R. Renz; W. Krenkel. Use of Ceramic Matrix Composites in High Precision Laser Communication Optics. In *European conference on spacecraft structures, materials and mechanical testing: 29 November-1 December 2000, ESTEC, Noordwijk, the Netherlands*, number 468 in ESA, pages 141–145. ESA publications division ESTEC, Noordwijk, 2001.

[20] Bernhard Heidenreich, Matthias Scheiffele, Marco Tausendfreund, and Hans-Ulrich Wieland. C/C-SiC telescope structure for the laser communication terminal in TerraSAR-X. In Walter Krenkel and Jaques Lamon, editors, *Tagungsband High Temperature Cearamic Materials and Composites*, pages 505–512, Bayreuth, Deutschland, 2010. AVISO Verlagsgesellschaft mbH.

[21] RSP technology. RSP alloys-overview-2025, January 2025.

[22] TIMET. timetal-550, 2025.

[23] SCHOTT. Technical properties for ZERODUR® glass-ceramic | SCHOTT.

[24] CORNING. HPFS_7979,7980,8655 Fused Silica product information, 2015.

[25] ECSS. ECSS-E-HB-32-20 Part 5A – Structural materials handbook – Part 5: New advanced materials, advanced metallic materials, general design aspects and load transfer and design of joints (20 March 2011) | European Cooperation for Space Standardization. pages 296–337. March 2011.

[26] Rochelle Brandt, M. Frieß, and Günther Neuer. Thermal conductivity, specific heat capacity, and emissivity of ceramic matrix composites at high temperatures. *High Temperatures-High Pressures*, 35/36:169–177, January 2003.

[27] Hemani Kaushal, V. K. Jain, and Subrat Kar. Link Feasibility Study. In *Free Space Optical Communication*, pages 197–204. Springer, New Delhi, 2017. ISSN: 1935-3847.

[28] P.D. Sundvold. PDF, January 1996.

[29] Isam Yunis. The Standard Deviation of Launch Vehicle Environments. Reston, VA, United States, April 2005. NTRS Author Affiliations: NASA Kennedy Space Center NTRS Report/Patent Number: KSC-2005-055 NTRS Document ID: 20120001364 NTRS Research Center: Kennedy Space Center (KSC).

[30] Jacob Wijker. Spacecraft Design Loads. In *Spacecraft Structures*, pages 27–69. Springer, Berlin, Heidelberg, 2008.

[31] Corina Koca, Bob Caffrey, Lateef Ajayi, John Ruffa, John Van Blarcom, Doug Rowland, Jim Simpson, Synthia Tonn, and Andrew Peddie. Representative Launch Environment Signature/Approval Page.

[32] ARCEON. General TDS Carbeon_fabric, April 2025.

[33] Yuan Shi, Fiona Kessel, Martin Friess, Neraj Jain, and Kamen Tushtev. Characterization and modeling of tensile properties of continuous fiber reinforced C/C-SiC composite at high temperatures. *Journal of the European Ceramic Society*, 41(5):3061–3071, May 2021.

[34] W. Gielesen, D. de Bruijn, T. van den Dool, F. Kamphues, E. Meijer, and B. C. Braam. GAIA basic angle monitoring system. In *International Conference on Space Optics — ICSO 2012*, volume 10564, pages 511–516. SPIE, November 2017.

[35] Florent Mallet, Jean-Marc Boitrel, Marc Ferrato, Alexandra Guggenheim, Jérôme Lavenac, Laurent Brouard, Alexandre Gerbert-Gaillard, Xavier Just, and Vincent Pecastaing. Manufacturing the Euclid Truss Spider: a large and lightweighted brazed SiC structure. In *International Conference on Space Optics — ICSO 2024*, volume 13699, pages 870–877. SPIE, July 2025.

[36] Rudolf Saathof, Will Crowcombe, S. Kuiper, Nick Valk, Federico Pettazzi, Dorus Lange, Peter Kerkhof, Martijn van Riel, Harry Man, Niel Truyens, and Ivan Ferrario. *Optical satellite communication space terminal technology at TNO*. July 2019.

[37] Hiroshi Hatta, Roland Weiss, and Patrick David. Carbon/Carbons and their Industrial Applications. In *Ceramic Matrix Composites*, pages 85–146. John Wiley & Sons, Ltd, 2014. Section: 5 _eprint: https://onlinelibrary.wiley.com/doi/pdf/10.1002/9781118832998.ch5.

[38] Bernhard Heidenreich. Melt iniltration process. In *Ceramic matrix composites: fiber reinforced ceramics and their applications*, pages 113–141. Wiley-VCH, Weinheim, 2008. OCLC: ocn181069640.

[39] H. Abu El-Hija and W. Krenkel. Cost Analysis for the Manufacture of C/C-SiC Structural Parts. In *High Temperature Ceramic Matrix Composites*, pages 846–851. John Wiley & Sons, Ltd, 2001. _eprint: https://onlinelibrary.wiley.com/doi/pdf/10.1002/3527605622.ch129.

[40] ECSS. ECSS-E-HB-32-20_part1a Overview and material properties and aplications, March 2011.

[41] H. Adibi, H. Esmaeili, and S. M. Rezaei. Study on minimum quantity lubrication (MQL) in grinding of carbon fiber-reinforced SiC matrix composites (CMCs). *The International Journal of Advanced Manufacturing Technology*, 95(9):3753–3767, April 2018.

[42] TNO. Launch satellite with SmallCAT laser communication system succesfull, April 2023.

[43] FSO-Instruments. Advanced Optomechatronic Systems – FSO Instruments.

[44] Othman I. Younus, Amna Riaz, Richard Binns, Eamon Scullion, Robert Wicks, Jethro Vernon, Chris Graham, David Bramall, Jurgen Schmoll, and Cyril Bourgenot. Overview of Space-Based Laser Communication Missions and Payloads: Insights from the Autonomous Laser Inter-Satellite Gigabit Network (ALIGN). *Aerospace*, 11(11):907, November 2024. Number: 11 Publisher: Multidisciplinary Digital Publishing Institute.

[45] eoPortal. Copernicus: Sentinel-2 - eoPortal, December 2024.

[46] eoPortal. TSX (TerraSAR-X) - eoPortal, November 2023.

[47] NFIRE.

[48] Sandra Erwin. Space Force MILNET constellation emerges as top 'unfunded priority', July 2025.

[49] Bernard J. Klein and John J. Degnan. Optical Antenna Gain 1: Transmitting Antennas. *Applied Optics*, 13(9):2134, September 1974.

[50] G. Morgante, L. Terenzi, L. Desjonqueres, P. Eccleston, G. Bishop, A. Caldwell, M. Crook, R. Drummond, M. Hills, T. Hunt, D. Rust, L. Puig, T. Tirolien, M. Focardi, P. Zuppella, W. Holmes, J. Amiaux, M. Czupalla, M. Rataj, N. C. Jessen, S. M. Pedersen, E. Pascale, E. Pace, G. Malaguti, and G. Micela. The thermal architecture of the ESA ARIEL payload at the end of phase B1. *Experimental Astronomy*, 53(2):905–944, April 2022. Company: Springer Distributor: Springer Institution: Springer Label: Springer Number: 2 Publisher: Springer Netherlands.

[51] B J Anderson, C G Justus, and G W Batts. Guidelines for the Selection of Near-Earth Thermal Environment Parameters for Spacecraft Design. 2001.

[52] Simon Appel and Jaap Wijker. *Simulation of Thermoelastic Behaviour of Spacecraft Structures: Fundamentals and Recommendations*. Springer Aerospace Technology. Springer International Publishing, Cham, 2022.

[53] David González-Bárcena, Juan Bermejo-Ballesteros, Isabel Pérez-Grande, and Ángel Sanz-Andrés. Selection of time-dependent worst-case thermal environmental conditions for Low Earth Orbit spacecrafts. *Advances in Space Research*, 70(7):1847–1868, October 2022.

[54] NASA. NASA7005, 2001.

[55] Bernhard Heidenreich, Nathan Bamsey, Yuan Shi, Miguel Such-Taboada, and Dietmar Koch. Manufacture and test of C/C–SiC sandwich structures. *CEAS Space Journal*, 12(1):73–84, January 2020. Company: Springer Distributor: Springer Institution: Springer Label: Springer Number: 1 Publisher: Springer Vienna.

[56] Walter Krenkel, T. Henke, and N. Mason. In-Situ Joined CMC Components. *Key Engineering Materials*, 127-131:313–320, November 1996.

[57] Peter Josef Hofbauer, Friedrich Raether, and Edda Rädlein. Finite element modeling of reactive liquid silicon infiltration. *Journal of the European Ceramic Society*, 40(2):251–258, February 2020.

[58] Dirk Biermann, T. Jansen, and M. Feldhoff. Machining of Carbon Fibre-Reinforced Silicon-Ccarbide Composites. *Advanced Materials Research*, 59:51–54, 2009. Publisher: Trans Tech Publications Ltd.

[59] David G. Gilmore, editor. *Spacecraft thermal control handbook*. Aerospace Press, El Segundo, Calif, 2nd ed edition, 2002.

[60] Janina Krieg, Antoine Carré, Thorsten Döhring, Peter Hartmann, Tony Hull, Ralf Jedamzik, and Thomas Westerhoff. The past decade of ZERODUR glass-ceramics in space applications. In *Space Telescopes and Instrumentation 2022: Optical, Infrared, and Millimeter Wave*, volume 12180, pages 2086–2100. SPIE, August 2022.

[61] Bernhard Heidenreich, Harald Kraft, Nathan Bamsey, and Miguel Such-Taboada. Shear properties of C/C-SiC sandwich structures. *International Journal of Applied Ceramic Technology*, 19(1):54–61, 2022. _eprint: https://ceramics.onlinelibrary.wiley.com/doi/pdf/10.1111/ijac.13818.

[62] Christopher T. G. Smith, Michal Delkowki, Jose V. Anguita, David C. Cox, Catherine Haas, and S. Ravi P. Silva. Complete Atomic Oxygen and UV Protection for Polymer and Composite Materials in a Low Earth Orbit. *ACS Applied Materials & Interfaces*, 13(5):6670–6677, February 2021. Publisher: American Chemical Society.

[63] J. V. Anguita, C. T. G. Smith, T. Stute, M. Funke, M. Delkowski, and S. R. P. Silva. Dimensionally and environmentally ultra-stable polymer composites reinforced with carbon fibres. *Nature Materials*, 19(3):317–322, March 2020. Publisher: Nature Publishing Group.

[64] Toray Celebrates the Successful Launch of the Historic James Webb Space Telescope - Toray Advanced Composites.

[65] Toray. EX-1515_cyanate-Ester_pds, January 2020.

[66] Baolong Sun, Chuang Xue, Weihui Shang, Mingxin An, Haojiang Zhao, and Hansi Zhang. The performance characterization of carbon fiber–reinforced plastic for space applications. *Journal of Reinforced Plastics and Composites*, 42(15-16):844–853, August 2023. Publisher: SAGE Publications Ltd STM.

[67] Paul J. J Tol, Tim A Kempen, Richard M Hees, Matthijs Krijger, Sidney Cadot, Ralph Snel, Stefan Persijn, I. Aben, and R.W.M. Hoogeveen. Characterization and correction of stray light in TROPOMI-SWIR. *Atmospheric Measurement Techniques*, 11:4493–4507, July 2018.

[68] Adrien Bolliand, Michel Lequime, Claude Amra, and Myriam Zerrad. Impact of localized defects in light scattered by optical components: measurement and analysis. *Optics Express*, 33:22396–22415, May 2025.

[69] Paul R. Spyak and William L. Wolfe. Scatter from particulate-contaminated mirrors. part 1: theory and experiment for polystyrene spheres and lambda=0.6328 um. *Optical Engineering*, 31:1746–1756, August 1992. ADS Bibcode: 1992OptEn..31.1746S.

[70] ECSS-Q-ST-70-50 Space product assurance Particles contamination monitoring for spacecraft systems and cleanrooms, April 2011.

[71] ECSS-Q-ST-70-02C Thermal vacuum outgassing test for the screening of space materials, November 2008.

[72] Renny Fields, Carl Lunde, Robert Wong, Josef Wicker, David Kozlowski, John Jordan, Brian Hansen, Gerd Muehlnikel, Wayne Scheel, Uwe Sterr, Ralph Kahle, and Rolf Meyer. NFIRE-to-TerraSAR-X laser communication results: satellite pointing, disturbances, and other attributes consistent with successful performance. In *Sensors and Systems for Space Applications III*, volume 7330, pages 211–225. SPIE, May 2009.

A

Alternative Composite Materials for Telescope Structures

Space-based optical communication terminals place stringent requirements on dimensional stability across thermal cycles and in challenging orbital environments. These demands could be met by low-CTE ceramics, such as C/C-SiC, however the novelty of the material, limitations in manufacturability and process control, motivate exploration of alternatives composite.

Carbon fiber reinforced polymers present a viable class of materials offering low density, high specific stiffness, and a customizable thermomechanical response through controlled fiber layup and matrix selection. This section reports the current state-of-the-art use of CFRPs in opto-structural applications, heritage from missions and concisely reporting some examples of resin systems, production techniques, and environmental stability countermeasures.

CHIME Mission
The CHIME mission demonstrates the use of CFRP in a toroidal telescope support structure, as shown in Figures A.1 and A.2. Although the mission has not yet flown, the structure has been manufactured.

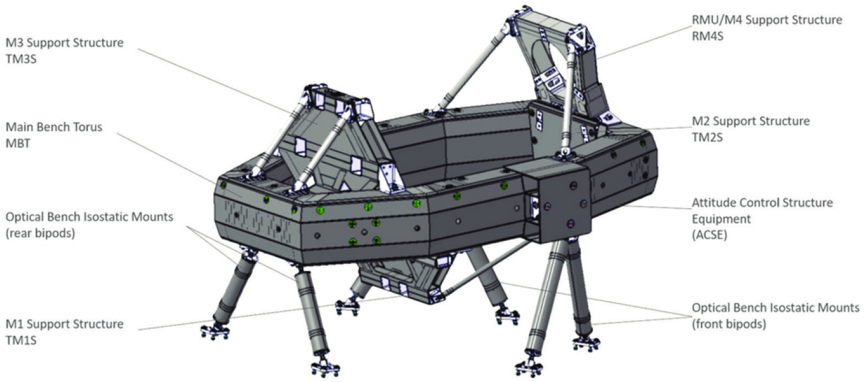

Figure A.1: CAD rendering of the CHIME CFRP torus structure.

Figure A.2: Presentation image of the actual CHIME CFRP structure [15].

Sentinel-5
Airbus employed CFRP bipods and honeycomb panels in the Sentinel-5 optical bench. The surfaces were protected with multilayer TiO_x/SiO_x coatings to counteract ultraviolet (UV) and atomic oxygen (ATOX) exposure, as shown in Figure A.3 [62, 63].

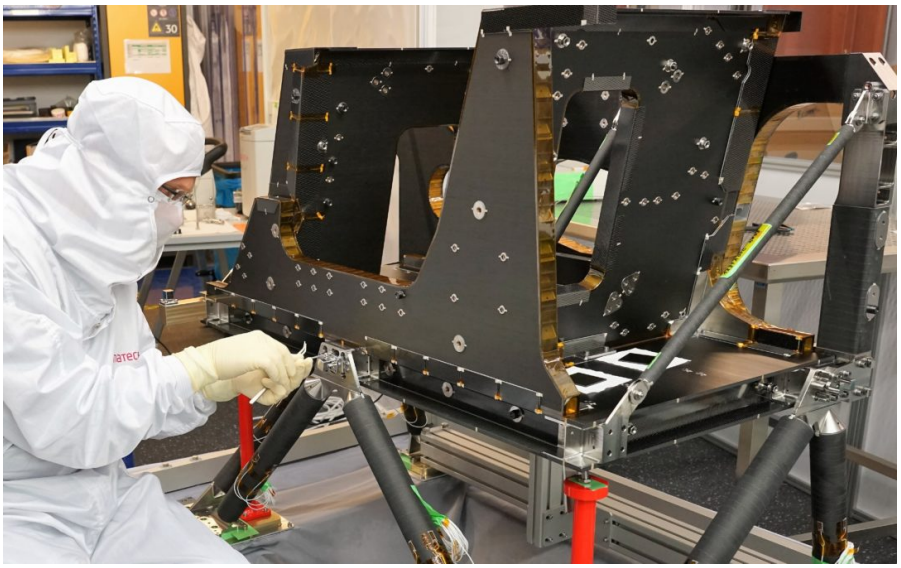

Figure A.3: CFRP structural elements used in Sentinel-5.

CHEOPS
The CHEOPS mission applied layup optimization and local thermal control to maintain a CFRP tube's CTE below 0.75 µm over 30 cm and 3 K (Figure A.4) [16]. This showcases laminate tailoring as a viable tool for precision thermal control in CFRP.

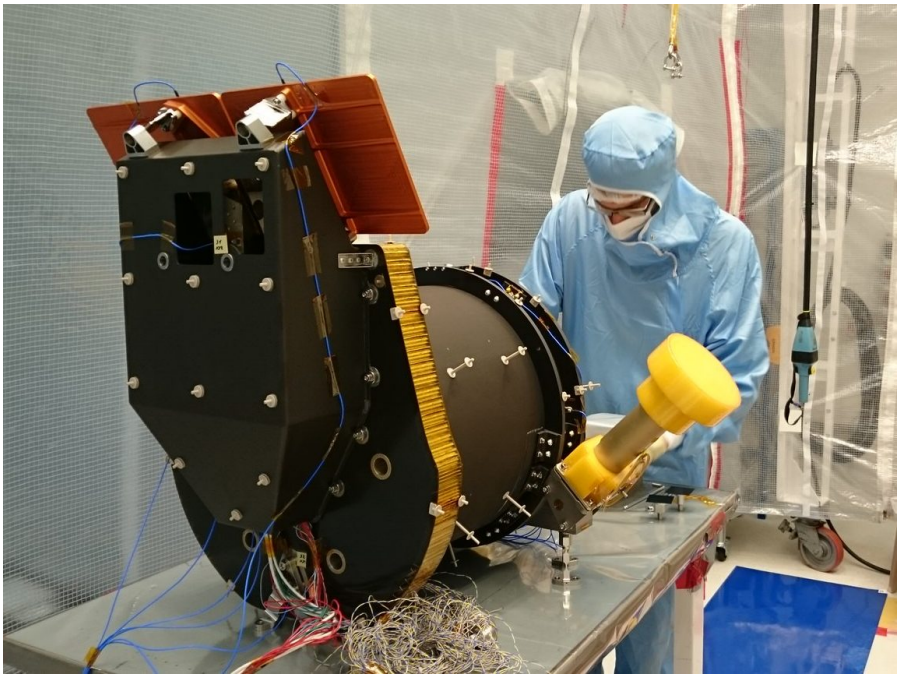

Figure A.4: Backside view of the CHEOPS telescope structure [16].

TNO Internal Breadboard
A prior thesis at TNO developed a CFRP hexapod telescope structure, verified via interferometry (Figure B.3). While a mismatch between expected and supplied CTE values was noted, this case illustrates the importance of accurate material characterization and fiber-matrix traceability in CFRP-based optics.

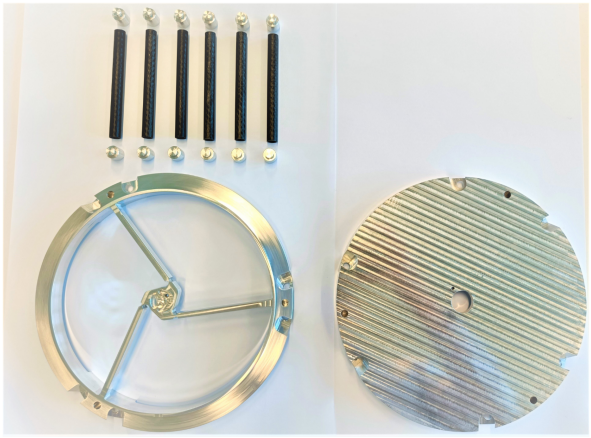

Figure 68: Parts for the test model telescope

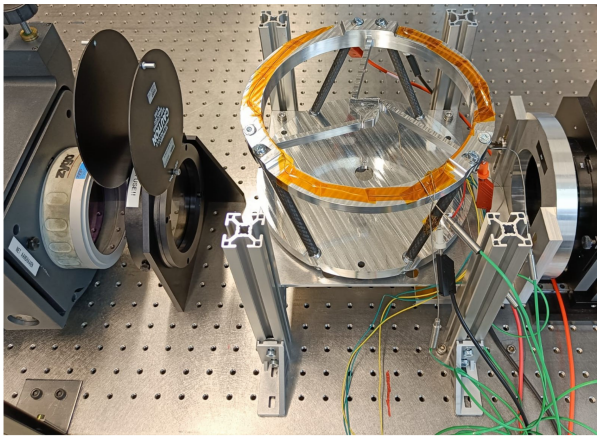

Figure 69: Telescope assembly

Figure A.5: CFRP breadboard telescope developed internally at TNO.

JWST MIRI Hexapod
The JWST's Mid-Infrared Instrument is mounted on a CFRP hexapod using cyanate ester resin and high-modulus fibers, optimized for cryogenic conditions (Figure A.6) [64]. This benchmark application demonstrates successful CFRP use under extreme thermal conditions.

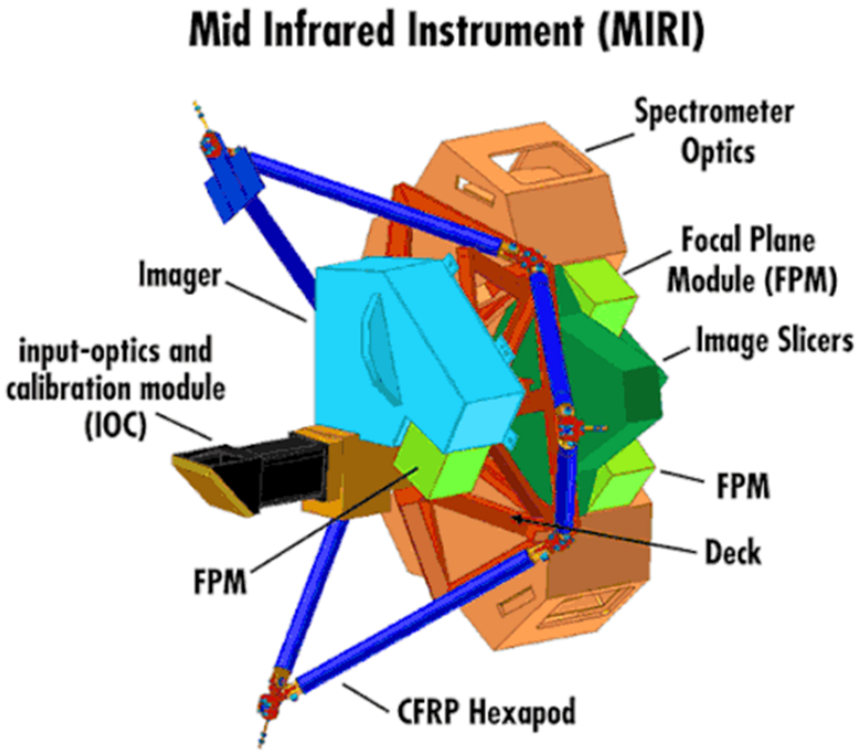

Figure A.6: The CFRP hexapod structure supporting the JWST MIRI instrument.

Matrix Systems and Outgassing Performance

Matrix selection is central to CFRP viability in vacuum. The ECSS standard endorses cyanate esters and PEEK (a thermoplastic) for low outgassing. Reported data show cyanate esters achieving CVCM = 0.01% and TML = 0.18% [65], while PEEK exhibits similarly favorable rates across multiple thicknesses (Figure A.7) [17].

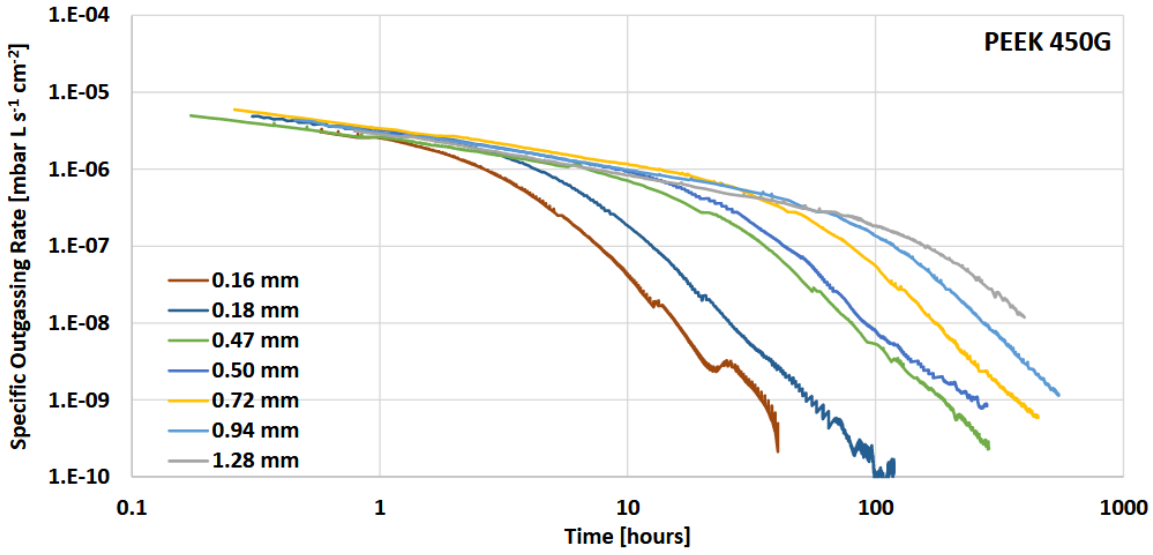

Figure A.7: Specific outgassing rate for PEEK as a function of thickness [17].

Manufacturing Techniques and Scalability

CFRP offers scalable production routes. Thermosets, such as cyanate esters, are compatible with conventional layup and autoclave curing. PEEK thermoplastics support ultrasonic welding and automated fiber placement, allowing cost-effective batch production.

Though thermoplastics offer recyclability and toughness, thermosets remain widely used due to their established performance in space applications.

Environmental Stability

While UV and ATOX degradation remain a concern, coating systems such as TiO_x/SiO_x have shown promise [62]. Most spacecraft designs with CFRP avoid direct exposure to these environments by shielding or positioning.

Thermal cycling and moisture stability are also essential. The coefficient of moisture expansion (CME) can exceed the CTE and must be controlled through cleanroom processing and symmetric layups. Enhanced stability can be achieved by incorporating additives such as carbon nanotubes into the matrix [66].

B

Clean Manufacturing

Materials developed for space applications are used to solve complex problems by using their properties to the fullest extent. One of the challenges is generally not as extensively addressed from a thermomechanical performance point of view. But improper procedures can have effects on thermo-mechanical performance, among many other degradations. Some examples are changes in optical properties, i.e., reflection/transmission/absorption/emission, sticking of surfaces, improper wetting of adhesives, and many others. Hence, care must be taken in every step of a process to avoid contamination. An example of particle contamination causing an electrical short is shown in Figure B.1.

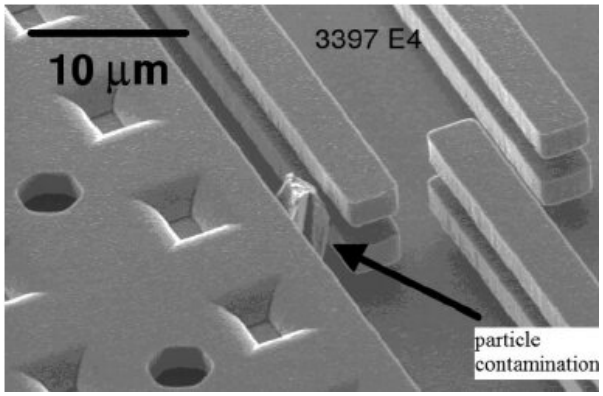

Figure B.1: Particle contamination example: found in microengine actuator, causing an electrical short of the drive signal. Reported by [18]

For most space systems cleanliness is non-negotiable, even more so for the one of a kind optical systems produced, designed and tested at TNO. In the overarching project, the test tube as manufactured was deemed unsafe for use in a vacuum environment during testing. Due to concerns of particulates releasing from the material and settling on the TVC. Figure B.2 provides an example of the rough unmachined surface of the first C/C-SiC test tube. These large particulates and the roughness embedding particles can pose risks for subsequent projects using the facility, and the facility itself.

The lessons learned and implications for using a C/C-SiC in a telescope for an LCT are discussed in this section. The information gathered is in part based on an interview taken with Frits van der Knaap. He is a product assurance engineer with more than 40 years of experience. A summary of the interview is provided in Appendix **??**

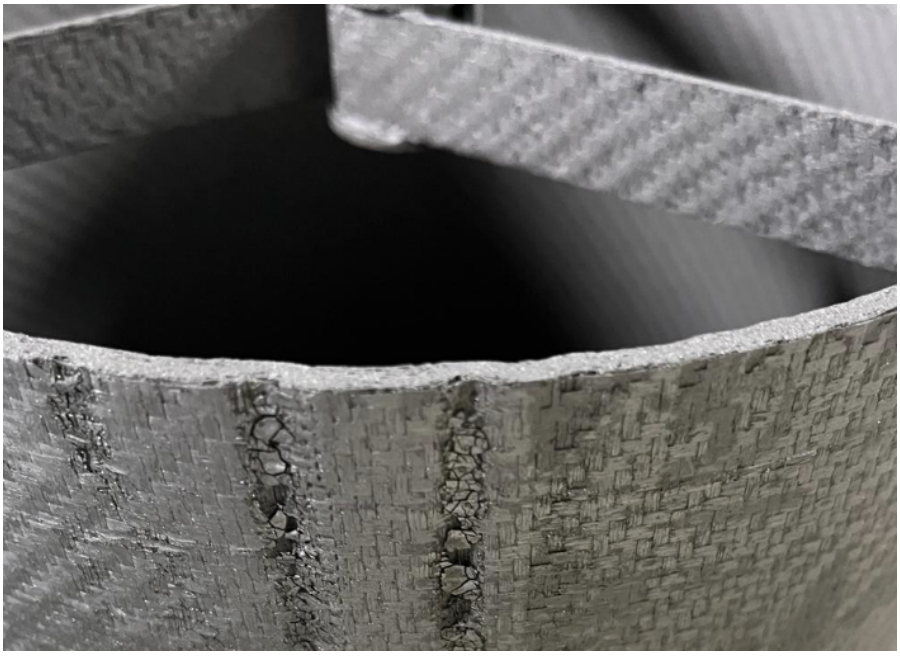

Figure B.2: Shows the rough surface including silicon flakes of the un-machined outer surface of the first CASTT structure. Their cause was found to be the wrinkles on the outer wall. These effects were mitigated by changing fiber layup

The main sources of contamination can be split up into categories, namely particle and molecular contamination (PAC & MOC). In an LCT and space applications more generally, testing facilities and equipment work at a high level of cleanliness. Guaranteeing this for a new supplier is a challenge due to the resources and knowledge required to guarantee the level of cleanliness.

There are a number of variables that govern the strictness of the required cleanliness and the ability of the manufacturer to guarantee adherence. The main considerations identified from internal documentation and the aformentioned interview are the following:

- The application, i.e, the telescope, e.g. for an LCT or for a science instrument.
- The cleanroom or vacuum facility in which the part will be assembled and/or tested. Depending on the common use cases of a cleanroom, its certification requirements may differ.
- Surface and material properties can prohibit some testing/monitoring procedures from being applicable.
- Rigorous consideration and documentation of sources of contamination need to be completed throughout the manufacturing process.

B.1. The effects of contamination

Contamination can significantly degrade the performance and reliability of high-end optical and space systems. In the context of laser communication terminals, where stability and precision are critical, even minor contamination levels can lead to unacceptable performance loss or damage.

PAC primarily leads to:

- Scatter and obscuration of optical surfaces, resulting in increased straylight and reduced in-beam light intensity;
- Changes in optical and thermal radiative properties;
- Increased friction or jamming of bearings or actuators and other precision mechanisms;
- Short-circuiting of electrical tracks or components in the presence of metallic particles.

MOC introduces additional risks, including:

- Degradation of reflection and transmission on sensitive optical surfaces due to spectral absorption or scatter from condensed droplets;
- Changes in absorptance/emittance (α/ε) of thermal control surfaces;
- Sticking of mating surfaces in precision mechanisms;
- Corrosion of electrical contacts or metallic surfaces;
- Chemically destructive reactions with liquid lubricants;
- Impaired wetting of adhesives and solders.

To ensure long-term suitability for high-end optical applications like LCTs, it is therefore essential to evaluate the cleanliness behavior of C/C-SiC throughout its processing chain. This includes assessing the effects of post-processing steps such as surface sealing, coating, or bake-out treatments, and establishing contamination control protocols tailored to the material's characteristics.

Without sufficient mitigation strategies, contamination risks could undermine the performance benefits that C/C-SiC offers in terms of thermal and mechanical stability.

Clearly the contamination effects need to be avoided. Most of the effects can be mitigated to the point where they do not interfere with the performance of the system. Apart from the transmission losses and stray light increase. The effects of stray light or scatter and methods by which they can be modeled are an active field [67] [68]. One of the principle models developed can be found in [69]

B.2. Sources of contamination

Contamination originates from a range of sources that must be considered throughout manufacturing, integration, and testing. For particulate contamination, the primary mechanism is particle fallout, where airborne particles settle onto exposed surfaces. Additional sources include human-generated particles, fibres and lint from clothing, and particles caused by material wear, shedding, or corrosion.

Molecular contamination arises mainly from outgassing of hardware or subsystems, particularly under vacuum or elevated temperatures. Cross-contamination is another key concern and can occur through off-gassing from materials present in the cleanroom, outgassing during thermal vacuum testing, or by direct and indirect contact. Indirect sources include handling or integration procedures, while direct contamination can result from the use of solvents, cleaning agents, or other process chemicals.

Effective contamination control depends on identifying and mitigating these sources at every stage of the process chain.

B.3. Tape-lift sampling

ECSS-Q-ST-70-50C-5.1.1.4 Tape-lift method describes on of the measurement methods to examin particle count on a surface of interest. In short, an adhesive tape is pressed onto a surface to collect particles. The tape is then examined under a microscope to count and size particles, offering a direct measurement of surface cleanliness. The steps involved are summarized below after which calculation is done to roughly estimate the allowable particles on a tape lift sample for the C/C-SiC tube. [70]

ECSS-Q-ST-70-50C Tape-Lift Test, summarized steps

Step 1: Detach tape from roll. Remove a 6−10 cm length of low-tack, transparent adhesive tape from the roll at a speed $\leq 1\,\mathrm{cm\,s^{-1}}$.
- *Reasoning:* Slow removal minimizes static electricity.

Step 2: Record dimensions for small samples. For local measurements on small surfaces (< 5 cm dimension), record in the measurement report: (i) the total surface and (ii) the analysed surface.
- *Reasoning:* Explicit documentation of both areas is required when a tape-lift is used to determine local particulate levels.

Step 3: Apply tape to the surface. Immediately after detaching from the roll, apply the tape to the sample in one direction using a force < 0.1 N.
- *Reasoning:* Controlled, low application force is prescribed for consistent contact.

Step 4: Smooth the tape. Use one gloved finger *or* a folded lint-free tissue to smooth the tape on the sample surface.
- *Reasoning:* Smoothing establishes uniform contact across the applied area.

Step 5: Verify adhesion quality (acceptance criterion). The tape, as applied, shall exhibit uniform adhesion and be free of voids, bubbles, or un-adhered regions.
- *Reasoning:* Non-uniform adhesion is not acceptable; if ripples/bubbles/un-adhered areas are present, reject and take a new sample at a different location.

Step 6: Initiate removal from the surface. Detach approximately 5 cm of the applied tape at a constant speed $\leq 1\,\mathrm{cm\,s^{-1}}$ and at an angle of $\sim 45°$ to the surface. Do not use sudden or uneven forces.
- *Reasoning:* Controlled speed and angle are prescribed; abrupt or uneven forces are explicitly disallowed.

Note: Subsequent actions (e.g., handling with a membrane filter, trimming, sample holder labelling, inspection, and analysis) follow the same procedure and are outside the present focus on initial handling and application.

There is no direct quantitative normative value in the ECSS it states : "to be agreed by the supplier and the customer". However if the process is combined with the TNO Iso class of the clean rooms and the surface area of the C/C-SiC test object. A suggestion can be made for the acceptable particle count from a tape lift test.

Multiple representative samples would have to be tested in accordance with the procedure in the ECSS norm. Where the following particle counts should only be used as a suggestion and a starting point. Contamination for the vacuum environment can be much more critical due to the lack of pressure. Increasing the particle release. The iso particle count per cubic meter of air is given in Table B.1

Table B.1: ISO particle limits per cubic meter. TVC is ISO Class 5.

ISO class	$> \mathbf{0{,}1}\,[\mu m]$	$> \mathbf{0{,}2}\,[\mu m]$	$> \mathbf{0{,}3}[\mu m]$	$> \mathbf{0{,}5}\,[\mu m]$	$> \mathbf{1}\,[\mu m]$	$> \mathbf{5}\,[\mu m]$
ISO 3	1000	237	102	35	8	0
ISO 4	10000	2370	1020	352	80	0
ISO 5	100000	23700	10200	3520	832	29
ISO 6	1000000	237000	102000	35200	8320	293

The values above are valid per cubic meter but the air is filtered completely multiple times an hour depending on an hour. Which would mitigate the particle introduction on sensitive surfaces. Never the less its taken as a total allowable budget per cubic meter of air. Taking a more conservative approach and simplifying the calculation.

Using the premise above a total allowable amount of particles can be estimated for the TVC test chamber which is an ISO 5 class facility. using a conservative estimate for the cylinder area the maximum amount of particles that could be allowed on a tape can be estimated.

$$p_a = \frac{p_{ISO} \cdot V_{TVC}}{A_{Cyl}} * A_{sample} \tag{B.1}$$

- p_a: Allowable number of particles on one tape-lift sample (count) for the selected particle-size bin.
- p_{ISO}: ISO class limit for particle concentration corresponding to the selected particle-size threshold (units: m^{-3}).
- V_{TVC} Internal volume of the thermal-vacuum (TVC) test chamber (units: m^3).
- A_{Cyl} Conservative estimate of the relevant internal cylindrical surface area used to convert volumetric limits to a surface-density limit (units: m^2).
- A_{sample} Area of the adhesive tape in contact with the surface during one tape-lift (e.g., $7 \times 1{,}2\,\text{cm}^2$); units: m^2.

Resulting in the table below using a 0.2 m^2 area for the cylinder and a $\tilde{0}.3$ m^3 for the TVC volume.

Table B.2: Suggested allowable particles per area of (background contamination corrected) $7 \times 1{,}2$ cm tape

ISO class	$> \mathbf{0{,}1}\,[\mu\text{m}]$	$> \mathbf{0{,}2}\,[\mu\text{m}]$	$> \mathbf{0{,}3}\,[\mu\text{m}]$	$> \mathbf{0{,}5}\,[\mu\text{m}]$	$> \mathbf{1}\,[\mu\text{m}]$	$> \mathbf{5}\,[\mu\text{m}]$
ISO 3	1	0	0	0	0	0
ISO 4	12	3	1	0	0	0
ISO 5	119	28	12	4	1	0
ISO 6	1188	281	121	42	10	0

The calculation above provides an approach to have a starting point which can be easily executed by ARCEON. Logically given the lack of available clean facilities the test should be done after a define cleaning procedure. For example, right after a rigorous cleaning using their ultra-sonic bath in a documented procedure.

There are multiple other mitigation and measurement techniques which can be employed. Some of which are touched upon in the coming sections.

Witness samples
Polished witness samples, typically made from silicon wafers or optical glass, are placed near contamination-sensitive hardware to collect particulate fallout over time. These samples are later inspected to assess environmental cleanliness levels.

Rinse sampling
Rinse techniques involve flushing a surface or cavity with a clean solvent, after which the rinse fluid is filtered and the captured particles analyzed. This approach is particularly useful for internal or complex geometries. Normative guidance is provided in the ECSS cleanliness and contamination control standards, which should serve as the primary reference for acceptance criteria and sampling methodology. A practical method is to submerge the component in an ultrasonic bath filled with demineralized water or another suitable rinsing fluid. After the first cleaning cycle, the fluid is removed and replaced with fresh liquid for a second ultrasonic cycle. A defined volume from this second rinse is then extracted and analyzed for particulate content.

For early estimates, a calculation similar to the tape-lift method can be applied: translate the maximum permissible ISO class 5 or 6 volume particle density, into an expected particle count. By using the sampled rinse volume based and extraction volume. Any design change or introduction of a new part requires a renewed cleanliness risk assessment.

Visual inspection
A qualitative method where surfaces are inspected under proper lighting conditions to detect visible contaminants. While not quantitative, this method is fast and effective for identifying gross contamination. It is a well documented procedure within TNO.

Airborne monitoring
Air cleanliness in cleanrooms and integration areas is monitored using airborne particle counters. These instruments measure the concentration and size distribution of particles suspended in the air, supporting compliance with required cleanliness classifications.

Each technique serves a specific role within an overall contamination control plan and helps verify that cleanliness requirements are met at various stages of the project lifecycle.

Mitigation techniques
Cleanrooms are generally classified by ISO standard or an equivalent version. Some general measures to achieve a certain class are clothing disciplines, airflow control, and limiting access to only trained personnel.

B.4. Particulates and Vacuum
Outgassing behavior under vacuum is an essential consideration when introducing new materials into space environments. According to ECSS-Q-ST-70-02C, thermal vacuum testing is used as a screening method to assess the suitability of materials by quantifying two key parameters: Total Mass Loss (TML) and Collected Volatile Condensable Material (CVCM). TML reflects the total fraction of material lost during a 24-hour exposure at 125°C in a vacuum, while CVCM measures the amount of that mass that re-condenses on a cold collector, simulating deposition on sensitive spacecraft surfaces. [71]

Specific processing routes or post-processing treatments may introduce constituents that contribute to TML or CVCM. If the thresholds specified in ECSS-Q-ST-70-02C are exceeded, the material may be disqualified for use in contamination-sensitive environments. This poses a challenge for material suppliers relatively new to space-grade and specifically high-end optics-grade cleanliness requirements or qualification procedures.

It is important to note that the standard ECSS screening conditions are not intended to replicate in-orbit behavior. The 125°C bake-out for 24 hours provides only a snapshot of outgassing under simplified conditions. For applications involving extended vacuum exposure, thermal cycling, or non-standard temperature profiles, further testing is recommended to characterize the long-term release of volatiles and their potential impact on nearby surfaces. [71]

CVCM remains a critical parameter, as the condensation of volatile material on cold surfaces—even in trace amounts—can alter optical and thermal performance. These effects can be difficult to detect post-integration and may lead to irreversible surface degradation. As such, great care must be taken to assess not only the material itself, but also any surface treatments, environmental exposure, or packaging that could introduce additional outgassing risks during qualification or operation.

B.5. CASTT Project Considerations
The introduction of LSI C/C-SiC envisioned low CTE applications require additional attention to be completed cleanly. It should be taken into account from the start of the design process. The challenge can be overcome as is shown by the adoption in the Nfire mission's LCT made by TE-Sat [72]. The main difference that might explain the success in terms of cleanliness is the difference in manufacturing process. An outer mold was used at least during the CFRP production process which explains the smooth outer surface.

Figure B.3: A foto of the final integrated C/C-SiC telescope resulting from the low CTE development reported in [19,20]

The roughness currently being the main cause of doubt since it might allow particles to embed within the surface. In addition it undermines the accuracy of simple tests like tape lifting.

An alternative method for assessing particulate contamination is the rinsing test, as described in ECSS-Q-ST-70-50C [70].